TAMPEREEN TEKNILLINEN YLIOPISTO
TAMPERE UNIVERSITY OF TECHNOLOGY

Hanna Hakola

Photoactive ZnO-Organic Nanostructures

Development and Characterization

Julkaisu 1385 • Publication 1385

Tampere 2016

Tampereen teknillinen yliopisto. Julkaisu 1385
Tampere University of Technology. Publication 1385

Hanna Hakola

Photoactive ZnO-Organic Nanostructures

Development and Characterization

Thesis for the degree of Doctor of Philosophy to be presented with due permission for public examination and criticism in Festia Building, Auditorium Pieni Sali 1, at Tampere University of Technology, on the 27th of May 2016, at 12 noon.

Tampereen teknillinen yliopisto - Tampere University of Technology
Tampere 2016

ISBN 978-952-15-3748-6 (printed)
ISBN 978-952-15-3759-2 (PDF)
ISSN 1459-2045

Abstract

Photoinduced processes in hybrid semiconductor-organic nanostructures were studied in this thesis. The work was divided into three tasks: (1) preparation of ZnO thin films and nanorod arrays in a controlled and cost-effective way, (2) functionalization of the ZnO surfaces with organic, photoactive layers and (3) study of photoinduced reactions on the surfaces by both steady state and time-resolved methods.

Aluminum doped zinc oxide (AZO) electrodes were tested as an alternative for the traditionally used indium tin oxide semitransparent electrodes in organic solar cell devices. The electrodes were prepared by atomic layer deposition method. Devices with AZO electrodes showed performance comparable to that of the reference device but were more stable in open air showing no degradation during 40 days time interval.

ZnO nanorod arrays were prepared and used as model substrates to study electronic interactions at semiconductor-organic interface. The growth was optimized to achieve well-aligned nanorods with high specific surface area. To control the semiconductor electronic properties, while keeping the morphology unchanged, the nanorods were further modified with thin layers of Al_2O_3 or TiO_2 prepared by atomic layer deposition.

Self-assembled monolayers (SAM) of three different porphyrin derivatives and one phthalocyanine derivative were formed on the ZnO nanorods using carboxylic acid or siloxane as anchor groups. The fastest electron transfer from zinc porphyrin (ZnP) to the semiconductor was observed for the ZnO nanorods modified with a 5 nm layer of TiO_2 (<0.2 ps). On the contrary, the charge recombination was not any faster compared to that of ZnP on the unmodified nanorods. This indicates that the charge recombination depends mainly on the semiconductor bulk properties, whereas the charge separation is determined by the surface properties of the semiconductor.

The charge generation mechanisms in the hybrid systems consisting of zinc phthalocyanine (ZnPc) SAM on ZnO nanorods covered by a spin coated layer of hole transporting materials, P3HT or Spiro-OMeTAD, were studied with time-resolved absorption spectroscopy. After selective excitation of ZnPc the primary electron transfer step was controlled by the hole transporting material. In the system with P3HT the first reaction step is a fast (1.8 ps) electron transfer to ZnO, whereas in the Spiro-OMeTAD system a fast (0.5 ps) hole transfer from the excited ZnPc to Spiro-OMeTAD is the dominant primary electron transfer step. However, in both cases long-lived (> 5 ns) charge-separated states are formed. In these states electrons are localized in ZnO and the holes in the organic donor layer, while ZnPc is in the ground state.

Preface

It has been a privilege to work at the Department of Chemistry and Bioengineering, Tampere University of Technology during these years. The work presented in this thesis is supported by the projects of the Finnish Funding Agency for Innovation (Tekes) and Academy of Finland. I'm also grateful of funding support from TUT President's doctoral programme and doctoral programme in Engineering and Natural Sciences at TUT.

I wish to express my deepest gratitude for the completion of this thesis to my supervisors, Prof. Nikolai Tkachenko for the guidance during my studies. I'm grateful for the trust and freedom I got during this work. Prof. Helge Lemmetyinen is gratefully acknowledged for giving me the opportunity to work in his excellent group and for the being supportive in all aspects regarding the work and the family as well. Special thanks for organizing the (skiing) seminars in Saariselkä.

I warmly thank all my partners for cooperation. Strong collaboration played an essential role in this work. Dr. Milja Mäkelä introduced me to the fascinating world of the atomic layer deposition. Prof. Tapio Niemi, Dr. Antti Tukiainen and Dr. Juha Kontio provided support with AFM and SEM. It was my pleasure to have an excellent ALD cooperation with Prof. Harri Lipsanen and Dr. Alexander Pyymaki Perros. Dr. Pasi Myllyperkiö shared sincerely his knowledge in pump-probe measurements. Prof. Hiroshi Imahori and Dr. Kei Kurotobi were responsible in carrying DSSC experiments. Without Alexander Efimov, I would not have the compounds to study.

My workmates at the Chemistry Lab are acknowledged for all the help in the lab and for the pleasant work atmosphere. Special thanks go to closest colleagues, Mrs. Kirsi Virkki, Dr. Essi Sariola-Leikas, Dr. Kimmo Kaunisto, Dr. Kati Stranius, Dr. Marja Niemi and Dr. Jenni Jarju, for sharing the cheerful and hard times during the years.

I am grateful to my family and relatives, especially Mom, Dad, Helena, and Annmari for the care and support along the way. I'm thankful to my son, Lauri for the joy and balance he has brought into my life. Finally, my warmest thanks go to Sami for being there for me.

Tampere, February 2016

Hanna Hakola

Contents

List of Symbols and Abbreviations

A	Absorbance
AFM	Atomic force microscope
ALD	Atomic layer deposition
Al_2O_3	Aluminum oxide
Alq_3	Tris-(8-hydroxyquinoline) aluminum
ATR	Attenuated total reflectance
AZO	Aluminum doped zinc oxide
CB	Conduction band
CPTPP	5-(4-carboxyplehyl)-10,15,20-triphenyl-21,23*H*-porphyrin
CT	Charge transfer
DEZ	Diethylzinc
DOS	Density of states
DSSC	Dye sensitized solar cell
ET	Electron transfer
FT-IR	Fourier transform infrared spectroscopy
FTO	Fluorine doped tin oxide
HOMO	Highest occupied molecular orbital
HTM	Hole transporting material
ITO	Indium doped tin oxide
IR	Infrared spectroscopy
J-V	Current-voltage

LUMO	Lowest unoccupied molecular orbital
MO	Metal oxide
P3HT	Regioregular poly(3-hexyl thiophene-2,5-diyl)
PTCDI	3,4,9,10 perylene-tetracarboxylic diimide
P-Si$(OEt)_3$	2-{3-[10,15,20-tris(3,5-di-tert-butylphenyl)porphyrin-5-yl]phenoxy}ethyl 4-(triethoxysilyl)butanoate
RMS	Root mean roughness
SAM	Self-assembled monolayer
SEM	Scanning electron microscope
Spiro-OMeTAD	2,2',7,7'-Tetrakis-(N,N-di-4-methoxyphenylamino)-9,9'-spirobifluorene
TA	Transient absorption
TCO	Transparent conductive oxide
TCSPC	Time correlated single photon counting
TMA	Trimethylaluminum
$TiCl_4$	Titanium tetrachloride
TiO_2	Titanium dioxide
TiO_2p	Titanium oxide nanoparticle
$Zn(NO_3)_2$	Zinc nitrate
ZnO	Zinc oxide
ZnOr	ZnO nanorods
ZnP	Zinc porphyrin
ZnPc	Zinc phthalocyanine

List of Publications

The Thesis is based on the work contained in the following publications, which will hereafter be referred to by their Roman numerals:

I. **Aluminum doped zinc oxide films grown by atomic layer deposition for organic photovoltaic devices**
Hanna Saarenpää, Tapio Niemi, Antti Tukiainen, Helge Lemmetyinen, and Nikolai V. Tkachenko
Solar Energy Materials and Solar Cells **2010**, *94*, 1379-1383.

II. **Self-assembled porphyrins on modified zinc oxide nanorods: development of model systems for inorganic-organic semiconductor interface studies**
Hanna Saarenpää, Essi Sariola-Leikas, Alexander Pyymaki Perros, Juha M. Kontio, Alexander Efimov, Hironobu Hayashi, Harri Lipsanen, Hiroshi Imahori, Helge Lemmetyinen, and Nikolai V. Tkachenko
The Journal of Physical Chemistry C **2012**, *116*, 2336-2343.

III. **Photoinduced electron transfer at nanostructured semiconductor-zinc porphyrin interface**
Hanna Hakola, Alexander Pyymaki Perros, Pasi Myllyperkiö, Kei Kurotobi, Harri Lipsanen, Hiroshi Imahori, Helge Lemmetyinen, and Nikolai, V. Tkachenko
Chemical Physics Letters **2014**, *502*, 47-51.

IV. **Effect of hole transporting material on charge transfer processes in zinc phthalocyanine sensitized ZnO nanorods**
Hanna Hakola, Essi Sariola-Leikas, Alexander Efimov, and Nikolai V. Tkachenko
The Journal of Physical Chemistry C **2016**, *120*, 7044-7051.

Author's contribution

Strong teamwork and collaboration have been prerequisite for all the publications. Hanna Hakola (Saarenpää) has been the main researcher and the first author in all publications. She planned and performed almost all the experiments, analyzed the results and wrote the manuscripts.

In publication I Tapio Niemi and Antti Tukiainen were responsible of the SEM and AFM characterization. In publication II Essi Sariola-Leikas synthesized one of the studied porphyrin derivatives. Alexander Pyymaki Perros did the ALD experiments for publications II and III. In publication III, the pump-probe measurements were made together with Pasi Myllyperkiö and the DSSC experiments were performed by Kei Kurotobi. Alexander Efimov and Essi Sariola-Leikas synthesized ZnPc chromophore studied in publication IV. The results are interpreted and discussed together with Nikolai Tkachenko. All co-authors commented the manuscripts.

1 Introduction

The world's energy consumption is growing rapidly and there is a need for new environmental friendly energy sources. Solar energy has a huge potential, about 885 million terawatt hours (TWh) of irradiation reach the surface of the earth every year. This means that sun can provide in a few hours the amount of energy we currently consume in a year. Furthermore, the solar energy is a clean, climate friendly and inexhaustible energy source and is relatively well-spread over the world.[1] However, only 2.6% of electricity consumption in Europe is produced by photovoltaic systems.[2] The huge gap between the potential and use of solar energy represents a great motivation for this thesis.

Organic and hybrid semiconductor-organic solar cells can be generally described as sandwich-type structures where the light absorbing material, dye, is assembled between transparent and metal electrodes. In organic solar cells, the basic operation principle can be described in four steps: (1) in the sun irradiation the excited state, exciton, is formed, (2) the exciton diffusion to the organic-organic interface yields (3) the primary energy conversion process, the charge separation, and (4) in the final step, the charges are transported to the electrodes, the holes to an anode and electrons to a cathode.[3] In hybrid solar cells, the first and last steps are similar to those of organic solar cells, but the charge separation takes place at a semiconductor-dye interface, where the excited dye injects an electron to the conduction band of the semiconductor and the ground state of the dye is restored by the electron transfer from the hole transporting material.[4-6]

With respect to design of new solar cell architectures, the development of new materials and a deep understanding of reactions taking place at the interfaces are important aspects. New materials are essential in terms of cost and performance of the devices. The interfaces between the layers play a key role since they control the charge injec-

tion and collection processes.[5,7,8] The study of photoinduced reactions at the interface is rather challenging. The interface structure in real devices is a complex one and several reactions are taking place simultaneously; therefore effects of individual reactions are difficult to distinguish. Furthermore, the time scale of photoinduced phenomena at the organic-organic and semiconductor-organic interfaces is short, typically in a femto- to picoseconds time domain. The real-time measurements in this time scale can only be acquired by ultrafast optical spectroscopy methods which require samples with specific optical properties. This highlights the importance of preparing model samples with simple organic-semiconductor and organic-organic interfaces, which would allow investigation by these advanced spectroscopy techniques.

The main research goal was to investigate the photoinduced charge transfer at the semiconductor-organic interface. There were two objectives to reach the main goal, (1) preparation of ZnO films in a controlled and cost-effective way and (2) functionalization of ZnO surfaces with organic, photoactive layers.

This Thesis summarizes the results from the four articles. The results are presented in Chapter 4 in the following order:

- The study of aluminum doped zinc oxide electrodes in photovoltaic applications is presented in Section 4.1. Electrodes were prepared by atomic layer deposition method and the performance was compared to the most common transparent electrode material, indium tin oxide.

- Preparation of model sample templates is described in Section 4.2. Hydrothermal growth of ZnO nanorods was optimized in terms of experimental conditions to achieve well-aligned structure with high specific surface area. Furthermore, while keeping the morphology unchanged, the surface properties were modified by a layer of Al_2O_3 or TiO_2, both prepared by atomic layer deposition.

- Finally, Sections 4.3 and 4.4 presents the study of photoinduced interactions at the semiconductor-organic interface. Three porphyrin and one phthalocyanine derivatives were studied as the organic sensitizer. The interactions were studied by both the steady state and time-resolved techniques.

2 Background

The interface between semiconductor electrode and dye sensitizer plays a key role in all types of hybrid solar cells and is fundamentally important in several fields, including photo- and electrochemistry, and molecular electronics.[7] This Chapter describes the theoretical background of the field: introduction to transparent conductive oxides, atomic layer deposition, self-assembled monolayers of organic chromophores, and photoinduced interactions at the semiconductor-dye interface.

2.1 Zinc oxide thin films and nanostructures

Transparent conductive oxides (TCO) are widely utilized in technological applications.[9-11] For example, thin films of TCOs are used as electrodes in optoelectronic devices, such as light emitting diodes and solar cells.[3,4,12] Three of the most common TCOs for electrode applications are indium oxide (In_2O_3), tin oxide (SnO_2) and zinc oxide (ZnO). Typically the oxides are doped with tin (In_2O_3:Sn = ITO), fluorine (SnO_2:F = FTO) and Al (ZnO:Al = AZO). ITO, FTO and AZO have wide optical band gaps (≥ 3.3 eV) and thus are transparent at wavelengths > 360 nm.[13] Among the TCOs, ITO is probably the most studied material because it has many important properties such as low electrical resistivity, high transparency and good substrate adherence.[14] On the other hand, ITO has some limitations and drawbacks, low abundance in the earth crust makes ITO expensive material and moreover, ITO is harmful for the humans and for the environment.[15]

ZnO is an attractive candidate for replacing ITO because it is non-toxic and inexpensive material. The abundance in earth's crust is 400 times higher than that of ITO (40 vs. 0.1 ppm).[13] ZnO thin films are used in organic solar cells as a buffer layer[16] and when doped as TCO in organic and hybrid solar cells.[17,18] ZnO fims can be prepared on

large areas by several methods including sputtering, pulsed laser deposition, and atomic layer deposition (ALD).[13,19]

One important advantage of ZnO is its ability to form a rich variety of nanostructures including rods, wires, tubes, flowers and they all have well-controlled surface morphology.[20-26] ZnO nanostructures are known to grow as single crystals resulting in excellent electrical properties along the nanostructure.[27] The nanostructures grown on a flat surface have increased specific surface area but it is still smaller than that of the nanoparticle film with the same thicknesses.[28,29] This fact may limit the use of ZnO nanostructures in some applications.

In this thesis the study is focused on the growth of the ZnO nanorods (ZnOr) by the hydrothermal growth method. Among all ZnOr preparation methods, the hydrothermal growth is widely used because of its simplicity and low-cost. One practical advantage of this method is the low growth temperature (< 100 °C), which allows a great choice of substrates.[30] The hydrothermal growth is a two-step process consisting of the seed layer formation on the substrate and the actual growth of ZnOr. The ZnO seed layer is an important prerequisite for the growth of the well-aligned dense ZnOr arrays. This can be understood by the nucleation theory. In most cases, the activation energy barrier is higher for a homogenous nucleation of solid phases than for a heteronucleation.[31] Also the interfacial energy barrier is smaller between the crystals and substrates than between the crystals and solution. Therefore, the heteronucleation onto a substrate takes place at a lower saturation ratio than the homogenous nucleation in solution. Forming a proper seed layer of the ZnO crystals on the substrate is the most straightforward way to control the morphology and orientation of the nanorods. Sputtering and spin coating of colloidal solutions are the two most commonly used methods but other methods, like atomic layer deposition can also be used.[32-34]

The actual growth of ZnOr is taking place typically in an aqueous solution of zinc nitrate ($Zn(NO_3)_2$) and hexamethylenetetramine (HMTA) at temperatures between 40-95 °C.[35,36] Zinc complexes are formed when hydroxide ions react with zinc ions. The ZnOr growth process can be summarized in the following chemical reactions.[21,37]

1. $Zn(NO_3)_2 \rightarrow Zn^{2+} + 2NO_3^-$
2. $(CH_2)_6N_4 + 6H_2O \rightarrow 6HCHO + 4NH_3$
3. $NH_3 + H_2O \rightarrow NH_4^+ + OH^-$
4. $Zn^{2+} + 2OH^- \rightarrow ZnO + H_2O$

Upon heating zinc nitrate produces Zn^{2+} ions (reaction 1) and HMTA decomposes to formaldehyde and ammonia (reaction 2). OH^- ions are produced by the reaction of ammonia with water (reaction 3). The solid ZnO is finally formed according to reaction 4. The actual role of HMTA is not fully understood in literature, but it is generally accepted that HMTA acts as a weak base and it slowly releases hydroxide ions into solution.[30,37]

2.2 Atomic layer deposition

Atomic layer deposition (ALD) is a chemical thin film deposition technique based on the alternate, saturated surface reactions at the gas-solid interface. The ALD method was developed for commercial use in Finland in the late 1970s by Tuomo Suntola and coworkers. The first ALD processes were aimed at manufacturing nanolaminate insulators (Al_2O_3/TiO_2) and zinc sulfide phosphor films for thin film electroluminescent displays. The list of available ALD materials is currently wide ranging for example from oxides, nitrides, and sulfides to metals. Currently, ALD is part of number of industrial applications where precise nanometer thick, pinhole free conformal films on any shape and geometry are required.[38-40] One example of commercial applications is anti-tarnish coating of silver jewelry and coins as illustrated in Figure 2.1.

FIGURE 2.1 ALD anti-tarnish coating for silver jewelry and coins.[40]

2.2.1 ALD operation principle

ALD utilizes highly reactive precursor chemicals, each containing different elements of the material being deposited. Each precursor is introduced separately into the reactor in a cyclic manner. The precursor molecules form a chemisorbed monolayer on the substrate surface and the following inert gas pulse prevents the gas-phase reactions and removes the volatile byproducts from the reaction chamber. As a simple example from the ALD cycle, the deposition of aluminum oxide is schematically illustrated in Figure 2.2. One cycle consists of four steps: (1) exposure of the first precursor, tri-

methylaluminum, (2) purge or evacuation of the reaction chamber, (3) exposure of the second precursor, water, and (4) purge or evacuation. This four-step cycle is repeated as many times as necessary to obtain the desired film thickness. Depending on the process, one cycle increases the film thickness by 0.1-3.0 Å.[38,39,41]

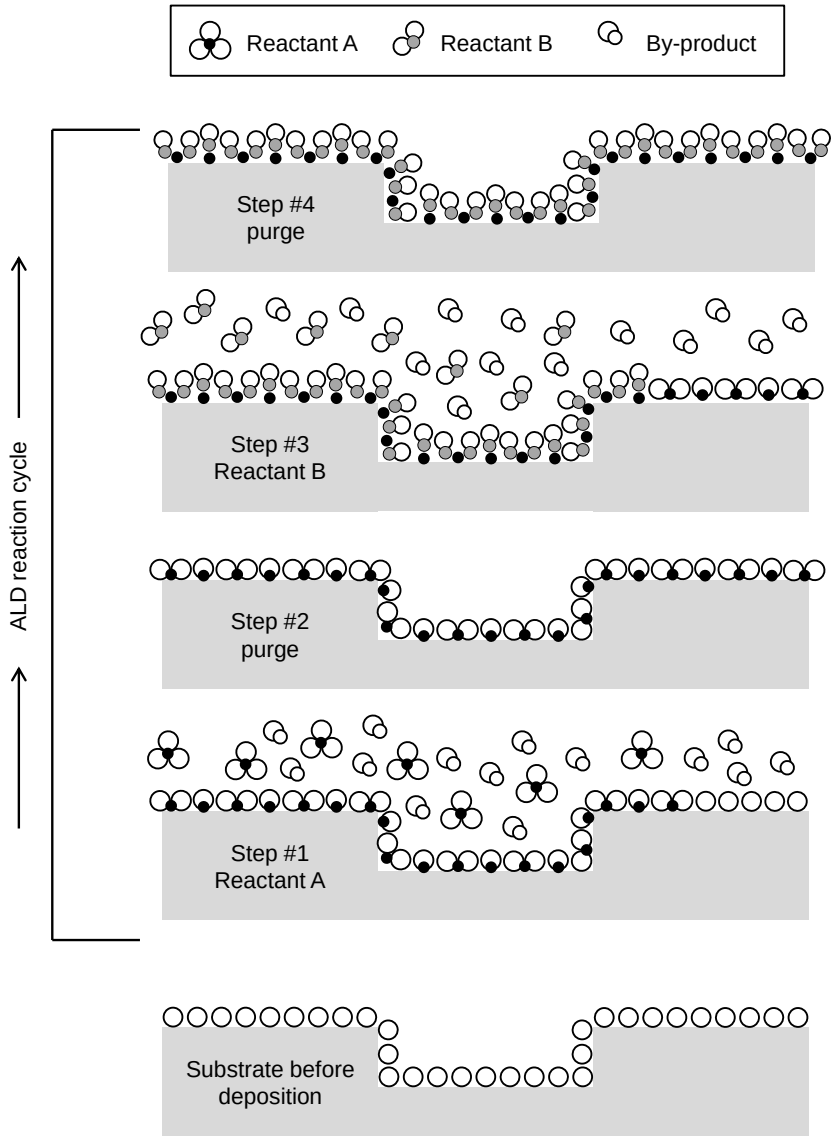

FIGURE 2.2 Schematic illustration of ALD cycle, modified from ref 41.

2.2.2 Benefits and limitations

The advantages of ALD are based on the surface controlled, self-saturating film growth principle. It is worth emphasizing that in order to achieve the benefits an ideal ALD process is needed. In addition to the proper selection of the precursors, the pulse and purge times, the precursor flux and the deposition temperature should be optimized.

Maybe the most unique benefit of ALD is extreme film *uniformity* on 3-D parts and porous materials and particles. *An accurate and simple film thickness control* down to the nanometer level is also one big benefit of ALD. Except the very first cycles when the surface is converted from the bare substrate to the film material, each cycle deposits the same amount of material. The ALD processes have a *high reproducibility* being operated without in situ control or tuning, and the processes run automatically, without the need for continuous operator attendance. Many ALD processes may be performed over a relatively *wide temperature range*. Therefore, a common growth temperature is often found for different materials, thereby making it possible to deposit multilayer structures in a continuous manner. *The control of material composition at atomic level* is easy. The doping level can be controlled by switching a fraction of deposition cycles to precursor containing a dopant. Major drawback of ALD is generally a rather low growth rate since in the best case only one atomic layer is deposited during one cycle. This can be partly compensated by scaling up the process and expressing the productivity in terms of film volume.[38,39,41]

2.2.3 Precursors

The choice of proper precursors is the key issue in a successful design of an ALD process. The requirements for precursors are not the same as in the case of other chemical gas-phase reactions, because instead of gas-phase, all the reactions should take place at gas-solid interface. At the deposition temperature, the precursors must have sufficient volatility and no self-decomposition is allowed. The reactions between the surface sites and the precursor molecules should be aggressive and complete. It's also important that precursors do not cause any etching of the substrate or the growing film. The precursors used in industrial applications should also be available at a reasonable price, be non-toxic, and safe to handle.[39]

2.2.4 Misconceptions of the ALD process

There are two general misconceptions concerning ALD process. Both are relevant in this thesis and therefore are briefly discussed here. First, one may think that ALD growth proceeds always in a layer-by-layer manner. This is often not true and only a fraction of monolayer of grown material is deposited in each cycle. The reason for this can be steric hindrances between the bulky ligands in the chemisorption layer. Another reason for the submonolayer deposition per cycle growth is limited number of reactive surface sites. For instance, when the number of –OH groups on the surface decreases with the increase of temperature, the growth rate decreases.[39,41]

Another misconception is that ALD would produce atomically smooth films. This may be true for amorphous and monocrystalline films, but not for the polycrystalline films. The nucleation and the film growth of polycrystalline films results in measurable surface roughness and it increases with the film thickness.[39]

2.3 Self-assembled monolayers

Self-assembled monolayers (SAMs) can be described as organic assemblies that are formed by the adsorption of molecular constituents from solution or gas phase onto solid surface. The technique can be used to form uniform layers of different classes of organic and bio-organic compounds on variety of metal and metal oxide surfaces. The research interest of SAMs has increased over the past years. First reports on SAMs date back to 1940s and nowadays SAMs are important part for example in hybrid opto-electronic devices such as dye sensitized solar cells.[4,42,43]

SAM formation is a spontaneous reaction where the reactive group of the anchor reacts with the surface atoms of the substrate, e,g. with hydroxyl groups of oxide surfaces.[43] A thiol group is common anchor for gold and some metal surfaces[42,43] whereas for metal oxides, there are more anchor groups available.[44,45] The immobilization can take place for example via carboxylic and phosphonic acid, siloxane, and anhydride anchors.[46-49] The big advantage of the SAM deposition technique is its simplicity. Any special arrangements (e.g. no high vacuum) are not needed, a substrate is dipped into the solution for a certain period of time and a monolayer is assembled. To achieve good quality SAMs many factors like, solvent, temperature, concentration and immersion time should be optimized.[50] Ethanol is widely used solvent for preparing SAMs and typical concentrations are at the level from µM to mM.[43]

An important property of SAMs is that they can be deposited on high curvature surfaces including porous surfaces if the characteristic size of pores is much greater than the size of molecules. The optical absorption of a SAM deposited on any non-flat surface is expected to be proportional to the effective surface area if the monolayer formation is completed. Therefore comparison of the absorptions of SAMs deposited on different types of porous surfaces is a relatively simple but informative way to monitor the effective surface area.[51]

2.4 Photoinduced processes at semiconductor-dye interface

Photoinduced electron transfer (ET) at a semiconductor-dye interface resembles that in a donor-bridge-acceptor complex, where the dye (electron donor) is assembled on the semiconductor (electron acceptor) through molecular spacer and anchor (bridge).[52] Electron injection from the excited dye to the semiconductor is thermodynamically possible when the lowest unoccupied molecular orbital (LUMO) of the dye lies higher in energy than the semiconductor conduction band (CB).[6] This is illustrated schematically in Figure 2.3.

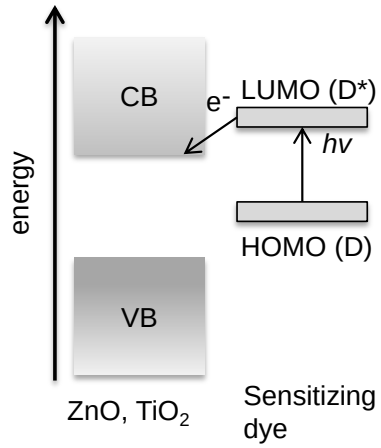

FIGURE 2.3 Scematic illustration of the energy level alignments at semiconductor-dye interface upon photoinduced electron transfer reaction.

Study of the primary electron transfer from the dye molecule to the metal oxide is a challenging task because several factors need to be taken into account as summarized in Figure 2.4. To achieve an efficient interfacial ET, prerequisites for the dye layer are: (1) a stable interfacial electronic coupling between the dye molecules and the metal oxide, (2) a dense and optimized packing of the dye molecules in the layer, and (3) an appropriate distance between the dye and metal oxide. The stable coupling is achieved if the dye has an anchor group, which reacts with the surface hydroxyl groups of the metal oxide and forms a chemical bond.[7,53] In addition to the type of the anchor group, the number of anchor groups and their position in the dye molecule have an impact on the molecular orientation, coupling strength and thus on the interfacial ET kinetics.[54-56] The packing density of the dye molecules should be optimized to avoid the excited state quenching due to the intermolecular interactions in the dye layer itself. Appropriate bulky substituent groups in the dye and possible small molecules as coadsorbates are the two main ways to reduce aggregation effects in the dye layer.[57-59] The ET rate is

also found to depend on the distance from the dye to the metal oxide surface. The longer the distance, the slower the ET is. Therefore the spacer group(s), which links the anchor group to the chromophore part of the dye molecule, is another key factor determining the rate of the ET processes.[60-62]

Considering the metal oxide properties, the most crucial factor may be the density of electron accepting states in the conduction band. The higher the density of the states (DOS) the faster the ET is. The DOS depends on the material and if the material bulk properties are compared, TiO_2 has a higher DOS than ZnO.[6,63] It is important to notice that the nanostructure properties can differ from the bulk properties. As the feature size decreases, the number of surface atoms increases relative to that in bulk and therefore the properties change. The role of the metal oxide nanostructure in ET is always a case-sensitive depending on the morphology and the preparation method.[51,64]

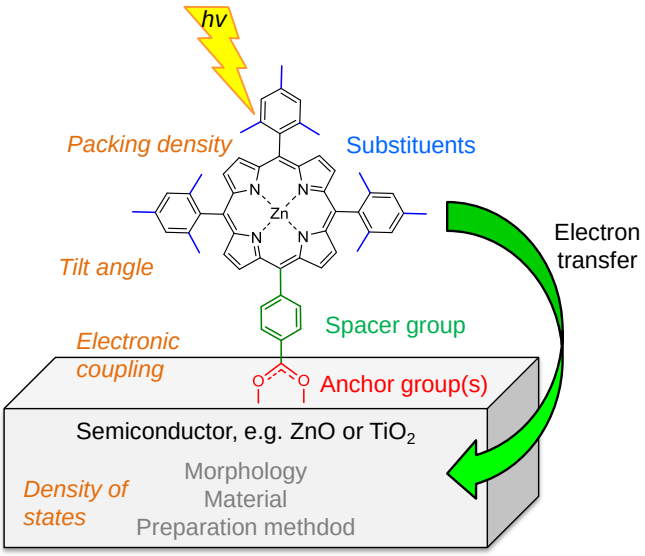

FIGURE 2.4 The factors determining the ET kinetics at a semiconductor-dye interface.

Upon photoexcitation of the dye molecules assembled on semiconductor, a few reactions can take place. At least two states can be formed in the dye layer, the singlet excited state and the cation, the latter can be formed after the primary electron transfer from the LUMOs of the excited dye to the electron accepting states in CB of the semiconductor.[58] However, excited state of the dye can be deactivated via the intermolecular interactions in the dye layer. To distinguish between the two reactions, the dye layer can be assembled on the insulating metal oxide, for example on the aluminum oxide (Al_2O_3). Its CB energy high enough to prevent the ET and the singlet excited state quenching is expected to originate only from the intermolecular interactions in the dye layer itself.

3 Materials and methods

This chapter describes the studied compounds, film preparation methods and the main characterization methods utilized in this thesis. More detailed description and the experimental details are found in publications I-IV and references therein.

3.1 Compounds

3.1.1 Compounds for photoactive thin films

Compounds used to prepare thin films are shown in Figure 3.1. Aluminum doped zinc oxide films were studied as light transparent electrodes in organic solar cells using regioregular poly(3-hexyl thiophene-2,5-diyl) (P3HT), 3,4,9,10 perylene-tetracarboxylic diimide (PTCDI) and tris(8-hydroxyquinoline) aluminum (Alq3) as photoactive layers. Approximately 20 nm layer of P3HT was prepared by spin coating and PTCDI (40 nm) and Alq3 (6 nm) were deposited by vacuum thermal evaporation.

Hole transporting materials, P3HT and Spiro-OMeTAD ((2,2',7,7'-Tetrakis-(N,N-di-4-methoxyphenylamino)-9,9'-spirobifluorene) were studied in publication IV. P3HT is well-known hole conductor in organic solar cells[3,65] but recently it is also used in solid state solar cells.[66] Spiro-OMeTAD is a common hole conductor in solid state dye sensitized solar cells (DSSC).[67,68] Both films were prepared by spin coating on top of ZnPc SAM on ZnO nanorods.

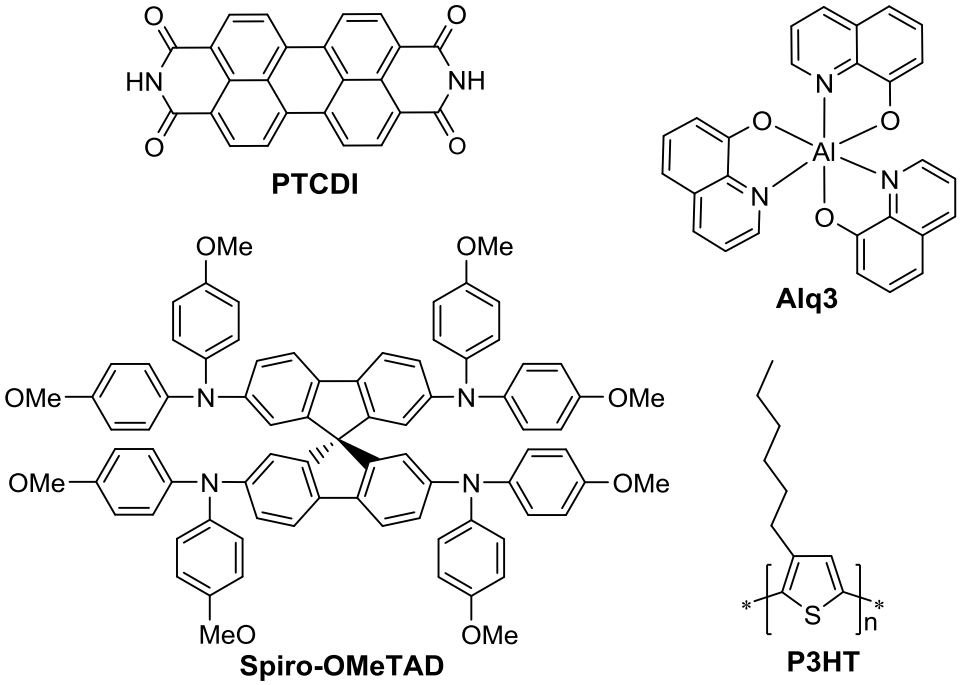

FIGURE 3.1 Molecular structures of the compounds for the thin film preparation.

3.1.2 Porphyrin and phthalocyanine derivatives

SAMs of three porphyrin derivatives and one phthalocyanine derivative were formed on ZnO, TiO_2, and Al_2O_3. The molecular structures are shown in Figure 3.2. 5-(4-Carboxyphenyl)-10,15,20-triphenyl-21,23H-porphyrin (CPTPP) was a commercially available chromophore and 5-(4-carboxyphenyl)-10,15,20-tris(2,4,6-trimethylphenyl) porphyrinatozinc(II) (ZnP) was synthesized at the Department of Molecular Engineering in Kyoto University. 2-{3-[10,15,20-tris(3,5-di-tert-butylphenyl)porphyrin-5-yl]phenoxy} ethyl4-(triethoxysilyl) butanoate (P-Si$(OEt)_3$) and zinc 4-(1,15,22-trimesityl-phthalocyanine-8-yl)benzoic acid (ZnPc) were synthesized at the Department of Chemistry and Bioengineering in Tampere University of Technology.

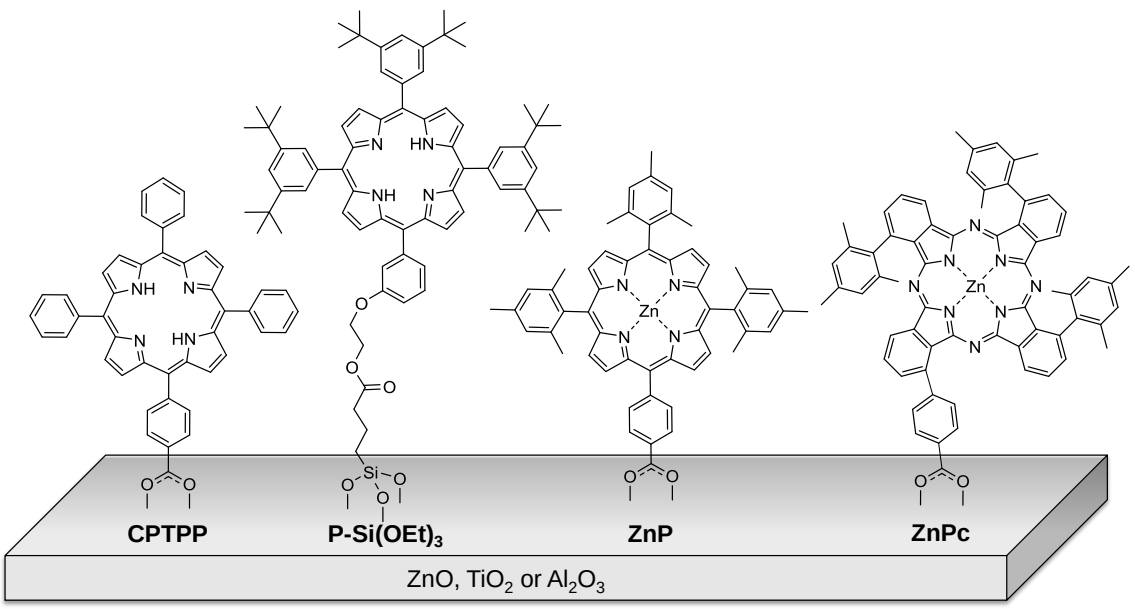

FIGURE 3.2 Molecular structures of chromophores assembled on metal oxide surfaces.

CPTPP, ZnP and ZnPc are bound to metal oxide surfaces with carboxylic acid anchor which is close proximity to the chromophore core. P-Si$(OEt)_3$ has a long, non-conjugated linker connecting the triethoxysilane anchor to the porphyrin core. ZnP resembles structurally CPTPP, but has Zn metal in central cavity and methyl substituents at the 2,4,6-positions of the *meso*-phenyl rings. P-Si$(OEt)_3$ and ZnPc have big substituent groups, *tert*-butyl and mesitylene, respectively.

3.2 Film preparation

The details of the film preparation are described in following Sections 3.2.1 - 3.2.3. Hydrothermal growth of ZnO nanorods and formation of self-assembled layers are described in details because both relay on manual work and small experimental details have an effect on the final result. Atomic layer deposition is a computer controlled process and reproducibility is high therefore only the most important parameters are described.

3.2.1 ZnO nanorods

ZnO nanorods were prepared in two steps. At first, the ZnO seed layer was formed on the substrate and after that the ZnOr were grown by hydrothermal method. Two different seed layers, denoted as A and B, were prepared by the spin coating of zinc acetate dihydrate solution on the ITO substrates followed by annealing. To ensure a good hydrophilicity, the substrates were treated with nitrogen plasma (publications II,III) or UV ozone (publication IV) for 10 minutes before the spin coating. To prepare seed layer A, 0.01 M zinc acetate in ethanol was spin coated on ITO and then annealed in air at 350 °C for 20 min. Both the spin coating and the annealing were repeated three times. Seed layer B was formed by using 0.23 M zinc acetate dissolved in a mixture of 2-methoxyethanol and ethanolamine 96:4. The spin coating and annealing were performed in the same manner as for seed A, but only one layer of zinc acetate was spin coated on ITO.

The actual growth of ZnOr was performed in plastic (polymethylpentane) staining jars in water bath. 10 substrates were placed in the jar filled with $Zn(NO_3)_2$ and HMTA as shown schematically in Figure 3.3. The distance from the substrates to the bottom of the jar was 3 cm and the total volume of reagent solution was 300 ml. For the growth process optimization the concentrations of the reagents were either 0.02 M or 0.05 M and the growth temperature varied from 80 to 90 °C.

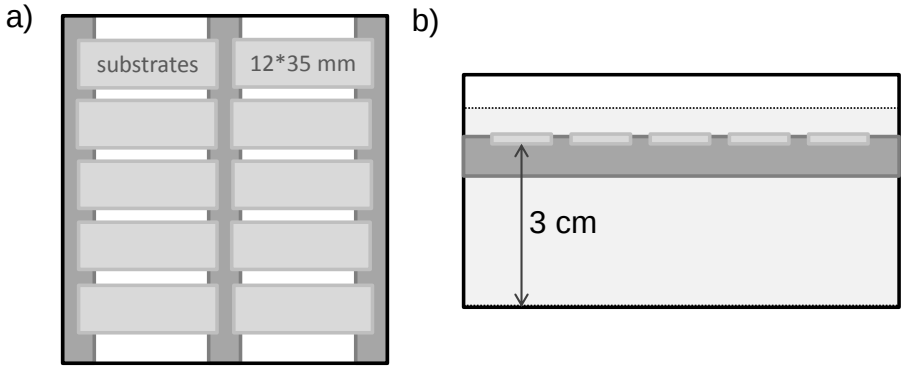

FIGURE 3.3 Schematic illustration of the ZnOr growth arrangement. a) Top view and b) side view. Gray line in figure b) corresponds to the level of the reagent solution.

The growth time of ZnOr varied from 2 to 10 hours. The growth solution was at room temperature when the jar was placed into water bath. The warming up of the solution to the target growth temperature took approximately one hour. The growth time was counted from the time when the growth temperature was reached. For the growth of 1.5 µm long ZnOr, the reagent solution was changed after each 5 hours of growth. This was done by rinsing the samples and the jar with milli-Q water and then placing the plates and a new solution of $Zn(NO_3)_2$ and HMTA again into the jar. After the desired growth time, ZnOr samples were rinsed with milli-Q water and dried in air. Finally, the ZnOr samples were annealed in air at 300 °C for 30 minutes. For the long time storing, the ZnOr jars were filled with nitrogen.

3.2.2 ZnO, TiO_2 and Al_2O_3 by atomic layer deposition

Atomic layer deposited films were used as transparent electrodes in solar cell prototypes and as modification layers of ZnO nanorods. Three materials, ZnO, Al_2O_3, and TiO_2 were deposited. Diethylzinc (DEZ), trimethylaluminum (TMA) and titanium tetrachloride ($TiCl_4$) were used as zinc, aluminum, and titanium precursors, respectively. In all processes water was an oxygen source and nitrogen was a carrier and purging gas. Pulse and purge times were process and device dependent. The resistivity of the ZnO film was reduced by aluminum doping. The relative level of Al-doping was 2.8%. In practice this was achieved by adding one TMA/water cycle after 35 DEZ/water cycles. The aluminum doped ZnO films (AZO) were deposited at two temperatures, 150 and 250 °C. The depositions of ZnO, Al_2O_3 and TiO_2 modification layers on ZnO nanorods were performed at 200 °C at Aalto University.

3.2.3 Self-assembled monolayers

CPTPP, ZnP, and ZnPc were dissolved in alcohols and attached on metal oxide surfaces via carboxylic acid anchors. The experimental details are summarized in Table 3.1.

TABLE 3.1 Concentrations, solvents, and reaction times used for the deposition of self-assembled monolayers of CPTPP, ZnP, and ZnPc, respectively.

Compound	Concentration	Solvent	Reaction time
CPTPP	0.20 mmol/l	ethanol	1 h
ZnP	0.20 mmol/l	methanol	1 h
ZnPc	0.05 mmol/l	butanol	16 h

After measuring the absorption spectrum of each metal oxide substrates, the plates were heated in oven at 150 °C for 30 minutes and cooled to 80 °C before immersing the plates into solution. After the desired reaction time the plates were rinsed carefully with pure solvent to remove any unbound molecules from the surface. The reaction time was optimized to be as short as possible to get saturated absorption. Too long reaction times may increase the degree of aggregation, especially in case of CPTPP, which has no substituents in the porphyrin phenyl rings.

The formation of P-Si$(OEt)_3$ SAM on MO surfaces was based on the reaction between the triethoxysilane anchor and MO. 0.08 mM P-Si$(OEt)_3$ was dissolved in distilled toluene and small amount of isopropyl amine was added to reaction vessel. The reaction was accomplished in two hours under argon at 105 °C. Well dried reaction vessel and substrate were required for the successful SAM formation.

The major practical difference between the carboxylic acid and the triethoxysilane anchor group is the fact that the carboxylic acid anchor can be used for several SAM reactions whereas solution of porphyrin with the triethoxysilane anchor can be used only once. For the real applications this has to be taken into account, but for laboratory test studies this is not essential. Typically, using 20 ml solution of P-Si$(OEt)_3$, seven SAM samples (12*35 mm) could be prepared simultaneously.

3.3 Microscopy

Atomic Force Microscopy (AFM) and Scanning Electron Microscopy (SEM) are versatile methods to characterize the metal oxide surfaces. The measurements were performed to ensure that the surfaces of the prepared metal oxide films could be used further for organic film deposition. The resolution, especially in z-scale is significantly better for AFM than for SEM and therefore the roughness of AZO electrodes is determined by AFM. On the other hand, AFM cannot be used to study non-flat surfaces such as nanorods, in which case SEM becomes the key method of structural characterization. In addition, SEM offers relatively high scanning speed enabling the convenient study of relative large surface areas. In typical SEM measurement, 3 keV accelerating voltage is used and the aperture size is set to 20 or 30 µm depending on the charging of the sample surface. In cross-section SEM imaging, one has to pay attention to sample preparation, because the interface can be damaged easily. Briefly, after scratching part of the front side of the cross section SEM sample by a diamond pen, the plate is cleaved by tilting both halves downwards. As a result, part of the cross-section stayed untouched and is suitable for SEM imaging.

3.4 Spectroscopy

3.4.1 Infrared spectroscopy

Fourier Transform Infrared spectroscopy (FT-IR) is an informative tool for structural characterization of organic molecules. Infrared radiation excites different types of vibration modes of the chemical bonds in the molecule. Each functional group has characteristic absorption band(s) in the infrared spectrum that can be used for the compound identification.[69]

In this thesis, the covalent bonding of ZnP carboxylic acid anchor to the metal oxide was proved by the FT-IR spectroscopy. The spectra were acquired in attenuated total reflectance (ATR) mode. In ATR mode, the IR-beam is directed trough ATR crystal onto sample surface (0.5 - 3 µm), reflected back to the crystal and passed to the detector. The benefit of the ATR-mode is minimal sample preparation. The only requirements are good contact between the sample and the crystal and lower refractive index of the sample than that of the crystal.[69] The bond formation was followed by comparing characteristic carboxylic acid stretching bands (ν(C=O) and ν(C-O)) in the solid compound and ZnP SAMs.[50,70,71]

3.4.2 Steady state absorption and emission spectroscopies

Steady state absorption spectra were recorded with a standard spectrophotometer (Shimadzu UV-360). The measurements reveal the ground state absorption spectra of the chromophores, which is important factor when selecting appropriate excitation wavelengths for time-resolved measurements. Steady state absorption is also simple and fast method to verify the quality of the SAMs. When forming SAMs of chromophores on ZnOr substrates, it is essential to measure each substrate spectrum before SAM formation because the scattering of ZnOr substrate is relatively strong especially in the porphyrin absorption region. If the substrate spectrum is not measured, the accurate estimation of the SAM absorption may be a challenging task.

Steady state emission measurements were the first tool to study the interactions at porphyrin SAM-metal oxide interface. The samples were excited at absorption maximum wavelength. SAMs on Al_2O_3 were used as a reference samples to distinguish between possible reaction pathways. CB of Al_2O_3 is high enough to prevent ET thus the excited state quenching is assumed to take place only by intermolecular interactions in the dye layer.

3.4.3 Time resolved spectroscopy

The fluorescence lifetimes were determined by the time-correlated single photon counting (TCSPC) method. All the measured samples were excited at 405 nm and fluorescence decays were monitored close to the particular emission maximum wavelength. The steady state emission intensities and fluorescence lifetimes of each studied compound on TiO_2 and ZnO were compared to those on Al_2O_3. If the relative quenching of the steady state emission intensity was observed to be greater than the relative shortening of emission lifetime, it indicates that there are some fast processes taking place, which are not resolved by TCSPC system due to instrument time resolution limit (60-70 ps).

The fast photoinduced reactions were studied by recording time resolved transient absorption spectra using the pump-probe method.[72] The method relies on the fact that molecules have different absorption spectra in the ground and excited state and in cationic or anionic form. Therefore intermediate states and their lifetimes can be identified due to their spectral signatures and spectral transformation times, respectively. Based on this information, the reaction pathways can be resolved. As a result of the pump-probe measurements the time dependence of transient absorption (TA) signals at each wavelength are obtained. The data were analyzed by fitting the TA decay curves globally with a multiexponential and/or distributed decay models.[73]

4 Results

This chapter provides a summary of the most important results and findings presented in publications I-IV. At first, the use of aluminum doped zinc oxide films as a transparent electrode in photovoltaic applications is discussed. Secondly, the study of photoinduced reactions at ZnO-organic layer(s) interface is described. Attention has been paid to careful sample preparations and finally to the study of photoinduced reactions.

4.1 Aluminum doped ZnO films as transparent electrodes

Two kind of AZO films prepared by ALD were studied as transparent electrodes in layered organic solar cells. AZO 1 refers to film deposited at 150 °C with the last cycle of TMA/water, the last cycle of AZO 2 film deposited at 250 °C was DEZ/water. The Al-doping level and the number of deposition cycles were the same for both films. The surface morphology of the AZO films was characterized by SEM and AFM. SEM images of the AZO films are shown in Figure 4.1, which illustrates that both films are uniform and have been grown as wedge-shape crystallites, as it is characteristic for ALD grown ZnO films.[74,75]

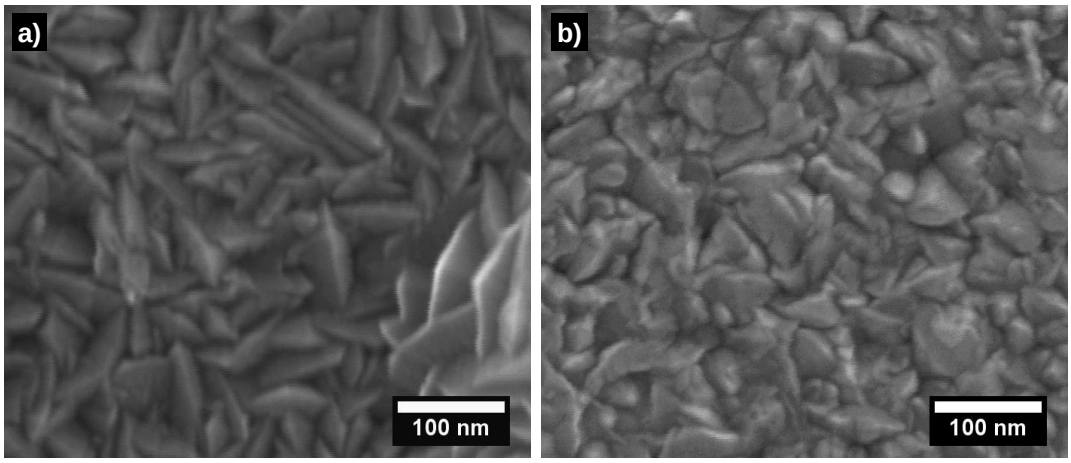

FIGURE 4.1 SEM images of aluminum doped zinc oxide films deposited at a) 150 °C (AZO1) and b) 250 °C (AZO 2).

Root Mean Roughness (RMS) values determined by AFM were 5.9 nm and 2.7 nm for AZO 1 and 2 films, respectively, and 3.3 nm for ITO. Previous studies have shown that the roughness of the ZnO films depends markedly on the film thickness.[76,77] The RMS value of the AZO film doubled when the film thickness increased from 90 nm to 170 nm as the consequence of higher growth rate at lower deposition temperature. Unlike one could expect the resistivity of the films is the same. Although AZO 2 film is thinner than AZO 1 the sheet resistance of both films was approximately 500 Ω/sq. The decreased resistivity with the increased deposition temperature may be related to different crystalline growth direction at different temperatures. At 150 °C the [100] direction is observed to be dominant whereas at 250 °C the [002] direction dominates the crystalline growth.[19] By increasing the film thickness and by optimizing the doping procedure the resistivity of the AZO films can be decreased to the same level as that of the ITO film (25-35 Ω/sq).[19,78,79] In spite of the relatively high resistivity of the AZO, it is not the factor limiting the studied solar cell performance because the photocurrent generated at active layers of P3HT-PTCDI junction was < 20 µA under the experimental conditions used. Thus the voltage drop (< 0.01 V) caused by the AZO electrode resistivity can be neglected.

A series of know photoactive compounds were deposited between the transparent and the metal electrodes. The structure of the layered solar cell is presented in Figure 4.2. The electrode next to electron donor (P3HT) is the anode whereas the electrode next to the electron acceptor (PTCDI) the cathode. Thus, in devices 1 and 2 the expected photoelectron flow is from Au toward AZO and in devices 3 and 4 from ITO or AZO toward Au. Each sample had at least five electrode pairs and at least couple of similar devices were prepared.

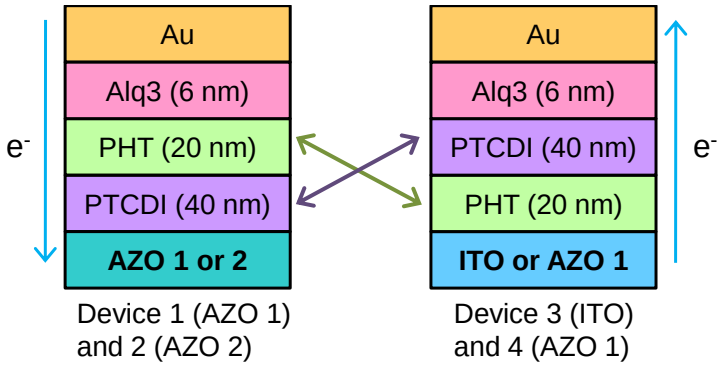

FIGURE 4.2 Schematic illustrations of solar cell structures. The blue arrow indicates the direction of the photoelectron flow.

Absorption spectra of two solar cell prototypes (without top electrodes) are shown in Figure 4.3. The absorption of the organic layers is clearly seen in the range of 450 - 600 nm. Due to the transparency differences between the ITO and AZO electrodes a small difference in absorption spectra is observed, but the spectra of the organic layers are essentially the same. The spin coating of P3HT on AZO|PTCDI does not dissolve evaporated PTCDI layer thus the order of the active layers does not affect the sample absorption.

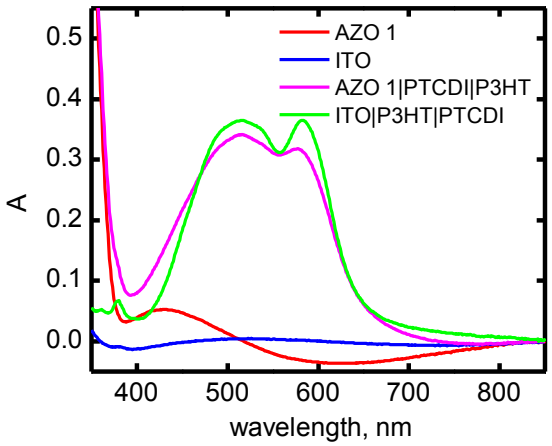

FIGURE 4.3 Absorption spectra of the solar cell prototypes and the transparent electrodes AZO1 and ITO.

Current-voltage (J-V) characteristics of the devices were measured in order to investigate possibility to use AZO electrodes in photovoltaic applications. The J-V characteristics of the devices with AZO and ITO electrodes are presented in Figure 4.4 and the photovoltaic parameters of the devices are summarized in Table 4.1.

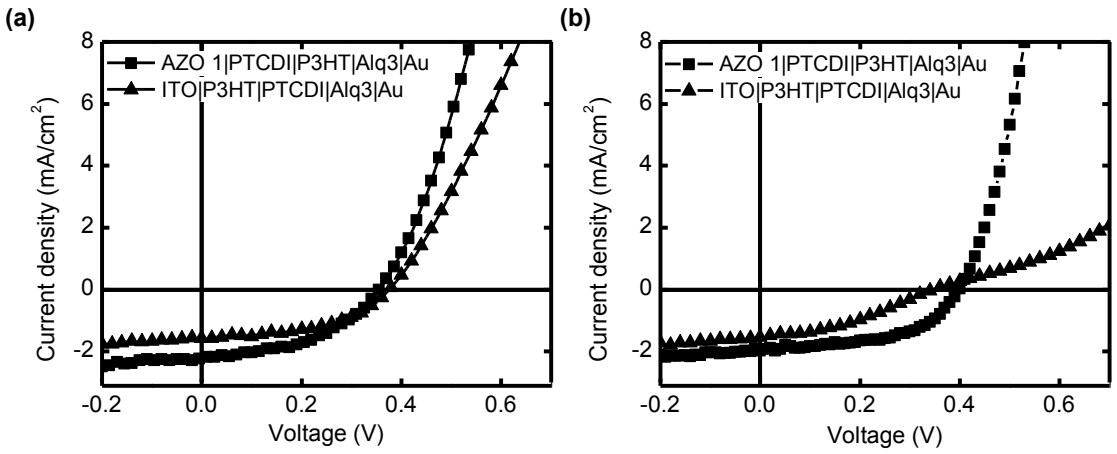

FIGURE 4.4 Current-voltage characteristics of the solar cell prototypes with AZO and ITO electrodes measured a) immediately after device preparation and b) 40 days (AZO) and one day (ITO) after the device preparation.

TABLE 4.1 Effect of time on short circuit current (I_{SC}), open circuit voltage (U_{OC}), fill factor (*FF*) and power conversion efficiency (η) of the measured devices. In the device, 1a refers to the electrode a and 1b to the electrode b.

Device		**Measurement**	I_{sc} **(mA/cm^2)**	U_{oc} **(V)**	***FF***	η **(%)**
1a	AZO1|PTCDI|P3HT|Alq3|Au	immediately	2.13	0.37	0.50	0.36
1a	AZO1|PTCDI|P3HT|Alq3|Au	after 18 days	2.08	0.40	0.52	0.41
1b	AZO1|PTCDI|P3HT|Alq3|Au	Immediately	2.24	0.36	0.45	0.39
1b	AZO1|PTCDI|P3HT|Alq3|Au	after 40 days	1.97	0.39	0.54	0.43
2	AZO2|PTCDI|P3HT|Alq3|Au	immediately	1.95	0.39	0.49	0.38
2	AZO2|PTCDI|P3HT|Alq3|Au	after 8 days	1.88	0.42	0.53	0.42
3	ITO|P3HT|PTCDI|Alq3|Au	immediately	1.58	0.37	0.50	0.29
3	ITO|P3HT|PTCDI|Alq3|Au	after 1 day	1.54	0.34	0.37	0.20

By comparing the results recorded immediately after the deposition of the top electrode, it was observed that the photovoltaic performances of the devices 1 and 2 are very similar to that of the reference device 3, but the order of the organic layers and photo-current generation direction is switched to opposite (the gold is the cathode in case of the device 3 and the anode in the devices 1 and 2). Device 4, which was otherwise identical to the reference device 3 but AZO replaces ITO, had significantly lower efficiency compared to other devices and the results are not shown in the Table 4.1. This result may be related to a poor performance of the AZO-P3HT interface, either the adhesion of P3HT to AZO is weak or the spin coated P3HT layer is too thin to form uni-

form film. From the theoretical point of view, the devices 1 and 2 may have better performance than the device 4 since the HOMO and LUMO levels of the P3HT and PTCDI layers have better matching to the corresponding work functions of the electrodes when AZO is used as the electron collecting electrode and Au is as the hole collecting electrode.[74,80,81]

Considering the measurements right after the device preparation, the results suggest that both of the AZO films work as well as the ITO film in organic photovoltaic devices. The difference in deposition conditions of the AZO electrodes and apparent difference in the crystalline structures has no significant effect on the device performance. Also deposition of aluminum oxide in the last cycle of the ALD process (device 1) had no detectable effect. Taking into account the ambient measurement conditions and the non-optimized active layers the obtained power conversion efficiencies are in the expected level.[82]

For the degradation testing the samples were stored in open air in dark at room temperature and the J-V measurements were repeated after certain period of time. The results are given in Table 4.1. There was no remarkable drop in short circuit current (I_{SC}) for the device 1 after 18 days of storing. When the measurement was performed 40 days after the sample preparation, I_{SC} has decreased by roughly 15%, but due to a small increase in open circuit voltage the total power conversion efficiency has increased slightly. Similar time trend was observed for device 2, indicating that both types of the AZO electrodes have a positive effect on photovoltaic device durability. The biggest difference is found by comparing the AZO and ITO devices. Initially I_{SC} is somewhat lower for ITO and decreases remarkably in one day. The shape of the J-V-curve is also changed as it can be seen from Figure 4.4b, resulting in decreased power conversion efficiency. The ITO-P3HT interface and the ITO electrode itself may be responsible for the fast degradation of the ITO device. Two degradation phenomena have been observed previously. The one is an exchanging reaction between oxygen in the outer monolayer of ITO and diffused oxygen and another is the diffusion of indium through the entire device to the counter electrode.[83-84]

4.2 Growth of ZnO nanorod templates

The study of AZO electrode discussed above have shown that ZnO is suitable wide band gap semiconductor for organic and hybrid semiconductor-organic solar cells. However, the layered structure used in the previous study is not optimal for constructing efficient solar cell, since absorption near the interface area responsible for the primary charge separation is weak. A known approach to solve the problem is to use a nanostructured template to build the interface with increased specific surface area. This approach is used in DSSC, where the working interface is interface between the layer of TiO_2 nanoparticles on a fluorine doped tin oxide electrode and SAM of dye sensitizer. ZnO may provide a more elegant and versatile solution to the problem, since a simple and non-expensive method exists to grow ZnO nanorods on a desired electrode surface. This section is devoted to developing a routine for growing ZnO nanorods suitable for solar cell applications.

4.2.1 Optimization of the hydrothermal growth of ZnO nanorods

The hydrothermal growth of ZnO nanorods was optimized to achieve well-ordered arrays of ZnOr with high specific surface area. This is a prerequisite not only for solar cells but also for time-resolved studies of interfacial photoinduced reactions because the absorption of the dye monolayers on a flat surface is too low for the measurements. Good alignment of ZnOr is essential requirement because it corresponds to ideal morphology. In this hypothesis, the interactions between the porphyrin molecules assembled on the neighboring nanorods can be neglected.

The effect of the ZnO seed layer, precursor concentration, growth temperature, and the growth time on the ZnOr morphology was studied first. Two types of the seed layers, denoted as layers A and B, were prepared by the spin coating. The essential difference in preparation process of seed layers A and B was the precursor concentration and the number of the spin coated layers. Seed layer A was prepared by spin coating of 0.01 M zinc acetate three times, whereas in the case of seed layer B only one layer of 0.23 M zinc acetate was spin coated. Typically, the ZnOr were grown on ITO substrates but also FTO substrates were used for DSSC experiments. The main reason to use the ITO coated (100 nm) glass substrates instead of clean glass plates was a better adhesion of the spin coated seed layer.

SEM images of the layers A and B are shown in Figure 4.5a,b, which demonstrate clearly the difference between them. Seed layer A consists of particles with 10-20 nm diameters and according to the cross-section SEM image (not shown) thickness of the

layer is approximately 10 nm. Seed B is approximately 25 nm thick and has a porous morphology. Small pores in the film (diameter less than 10 nm) are most probably due to the decomposition of zinc copolymers during the annealing.[85]

Figure 4.5c,d shows nanorods grown on seed layers A and B while keeping reaction conditions otherwise the same. The seed layer act as a nuclei for ZnOr growth and has strongest effect on the ZnOr density and orientation.[34,86,87] The alignment of the ZnOr grown on the seed layer B is almost perpendicular to the substrate surface and the density is higher compared to that of seed layer A.

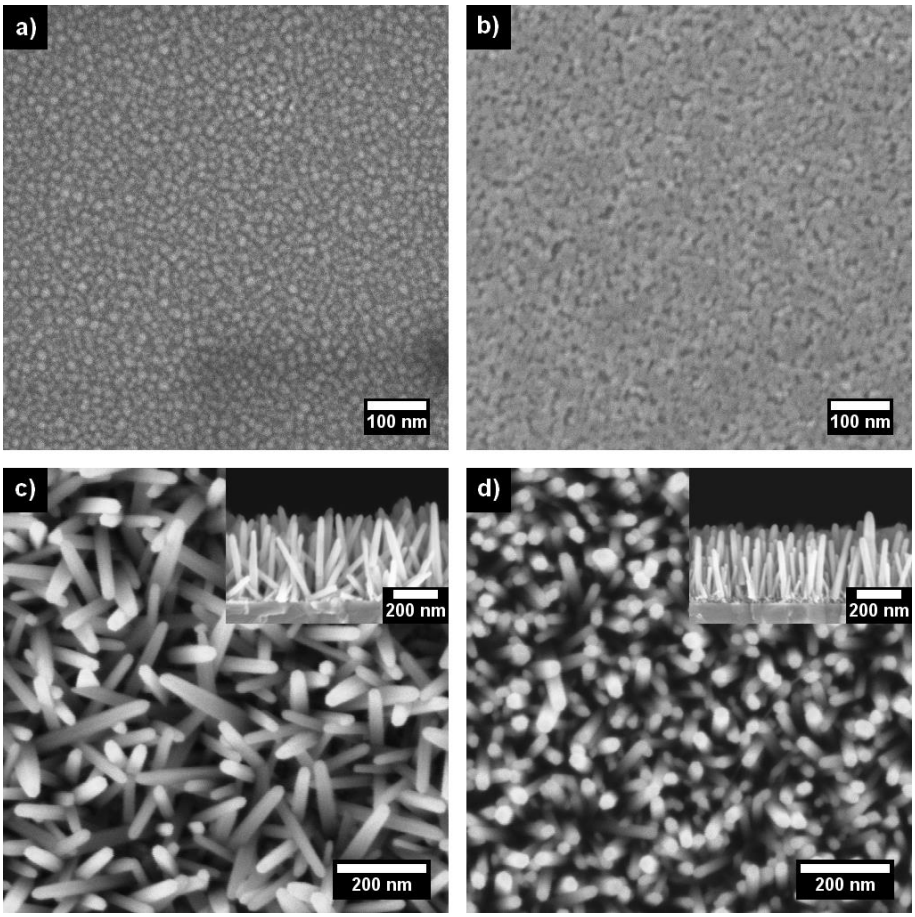

FIGURE 4.5 SEM images of seed layers a) A and b) B, c) ZnOr grown at 80 °C for 4 h on the seed A (diameter 40 nm, average length 350 nm) and d) ZnOr on the seed layer B (diameter 35 nm, average length 250 nm).

In contrast to previous studies, the seed layer has only minor effect on the average diameter of the ZnOr, which is mainly determined by the precursor concentration.[34,88,89] This can be clearly seen in SEM image shown in Figure 4.6, by changing the concentration from 0.02 M to 0.05 M the average diameter increases from 40 nm to 100 nm. In principle, the larger diameter should increase the effective surface area if the density

remains the same. Apparently this is not true because ZnOr with larger diameter start to fuse together leading to smaller surface area.

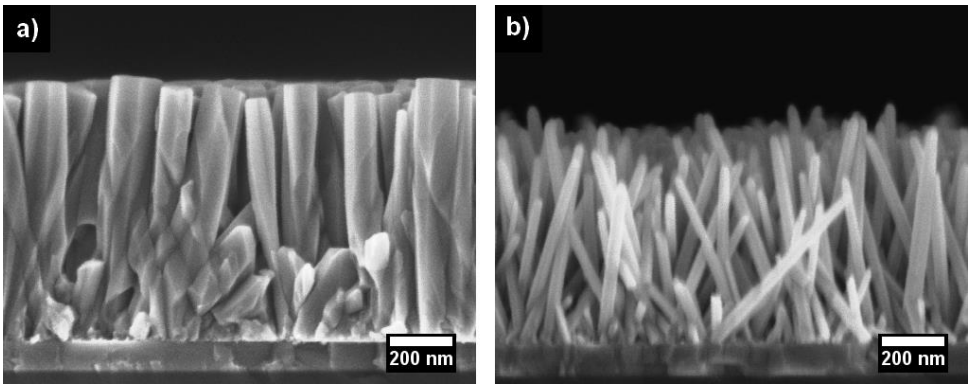

FIGURE 4.6 SEM images of ZnOr grown at 80^0C for 6 h on seed layer A using a) 0.05 M and b) 0.02 M precursors.

The growth temperature determines the ZnOr growth rate if other growth parameters are kept constant. In the 80-90 °C temperature range, both the length and diameter increases with the temperature. The optimum temperature for the growth of high aspect ratio of ZnOr was determined to be 85 °C.

The ZnOr length depends linearly on the growth time as long as precursor concentration is sufficient. When long (> 1 µm) ZnOr were grown, the precursor solution was changed after 5 hours growth to ensure a stable growth rate.

4.2.2 Effective surface area of ZnO nanorods

The effective surface area of the ZnOr was estimated by absorption spectroscopy. CPTPP SAMs were deposited on ZnOr grown in different conditions and the absorption increase was compared to the absorption value of the same monolayer on the flat ZnO surface (0.03). Figure 4.7 shows the dependence of the increased surface area on the length of ZnOr for three different series of the ZnOr substrates.

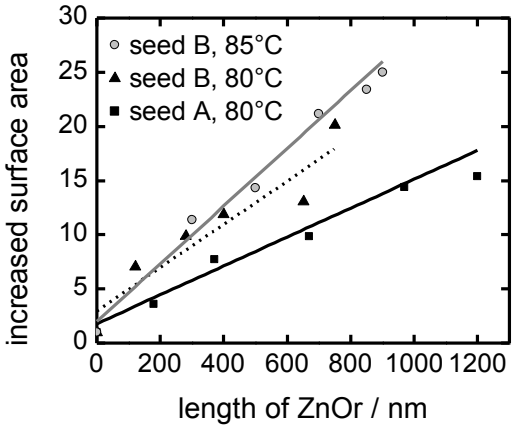

FIGURE 4.7 Dependence of the surface area on the ZnO nanorod lengths grown at 80 °C on seed A (black solid line, squares) and seed B (black dotted line, triangles) and those of grown at 85 °C on seed B (gray solid line, circles).

ZnOr grown on seed A (at 80 °C) have smaller surface area compared to that of the ZnOr grown on seed B (at 80 °C or 85 °C). The main reason for this is the lower density of ZnOr, because the diameter is even greater if seed A is used (see Figure 4.5c). The surface area increases almost linearly with the length of ZnOr, though small deviations from the linear dependence can be attributed to a variation in the seed layer morphology and growth conditions leading to some differences in the ZnOr dimensions. The growth temperature of ZnOr has no detectable effect on the surface area for nanorods of the same length, though the growth rate is higher at higher temperature.

Approximately 1.5 µm long ZnOr were prepared for the study of photoinduced electron-transfer processes at porphyrin-metal oxide interface (publications II and III). The growth was performed at 85 °C using porous seed layer (type B) and 0.02 M precursor solutions. SEM image and schematic illustration of the sample dimensions are shown in Figure 4.8. The increase in the surface area is not linear in the length range of 0.9 - 1.5 µm, because longer ZnOr starts to fuse together at their roots. However, the absorption of studied porphyrin derivatives on 1.5 µm long ZnOr was sufficient for time-resolved absorption measurements. The measurements were also carried out with a thin (2-5 nm) modification layer deposited on top of ZnOr, which had no detectable effect on the effective surface area, as will be discussed later.

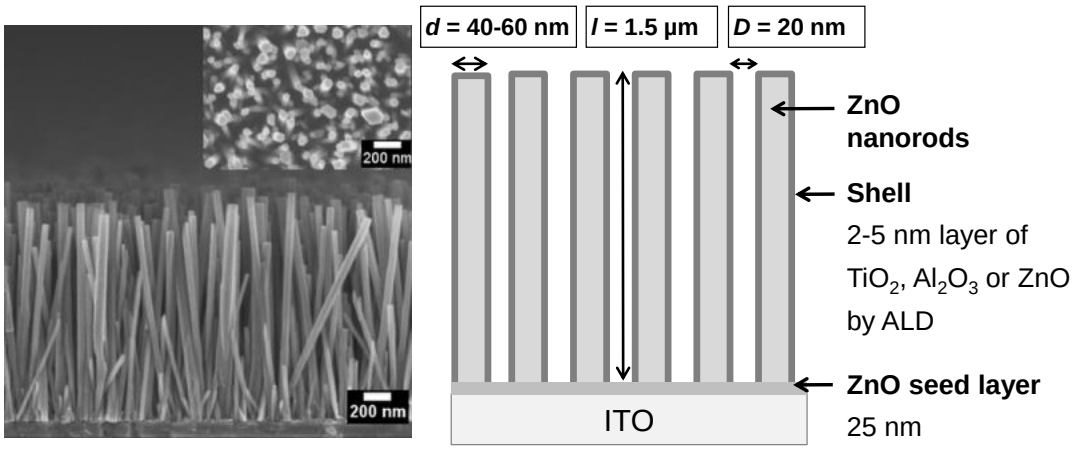

FIGURE 4.8 Optimized structure of ZnO nanorods for the study of photoinduced electron-transfer processes at an porphyrin-metal oxide interface.

For the study of photoinduced charge transfer through ZnPc layer (publication IV), the ZnOr were grown at 85 °C using type B and 0.02 M precursor solutions. In this case the growth time was five hours which resulted in 600 nm long ZnOr. This length was a compromise between reasonably high ZnPc monolayer absorption and the sufficient infiltration of hole transporting materials into ZnOr structure.

4.3 Preparation of photoactive ZnO-organic structures

4.3.1 Porphyrin monolayers on metal oxides

Before studying the photoinduced processes at porphyrin-metal oxide interface, the monolayer formation was confirmed by steady state absorption and FT-IR spectroscopy methods.

Absorption spectra of the free base porphyrin SAMs on the modified ZnOr substrates are shown in Figure 4.9. Typical features of the porphyrin spectrum, Soret band, and four or two Q bands, are observed in all spectra. Among all SAMs, CPTPP SAMs have highest absorption. CPTPP is the only porphyrin derivative, which has no substituents in the porphyrin phenyl rings, thus the packing density is expected to be the highest. Lack of the substituents results also in increased aggregation as indicated by the highest red-shifted absorptions relative to the solution spectra. The effect of ZnOr modification layer (2 or 5 nm layer of TiO_2 or Al_2O_3) on the effective surface area cannot be determined because the variation in surface area of ZnOr grown on identical conditions was stronger than the effect of the modifying layer.

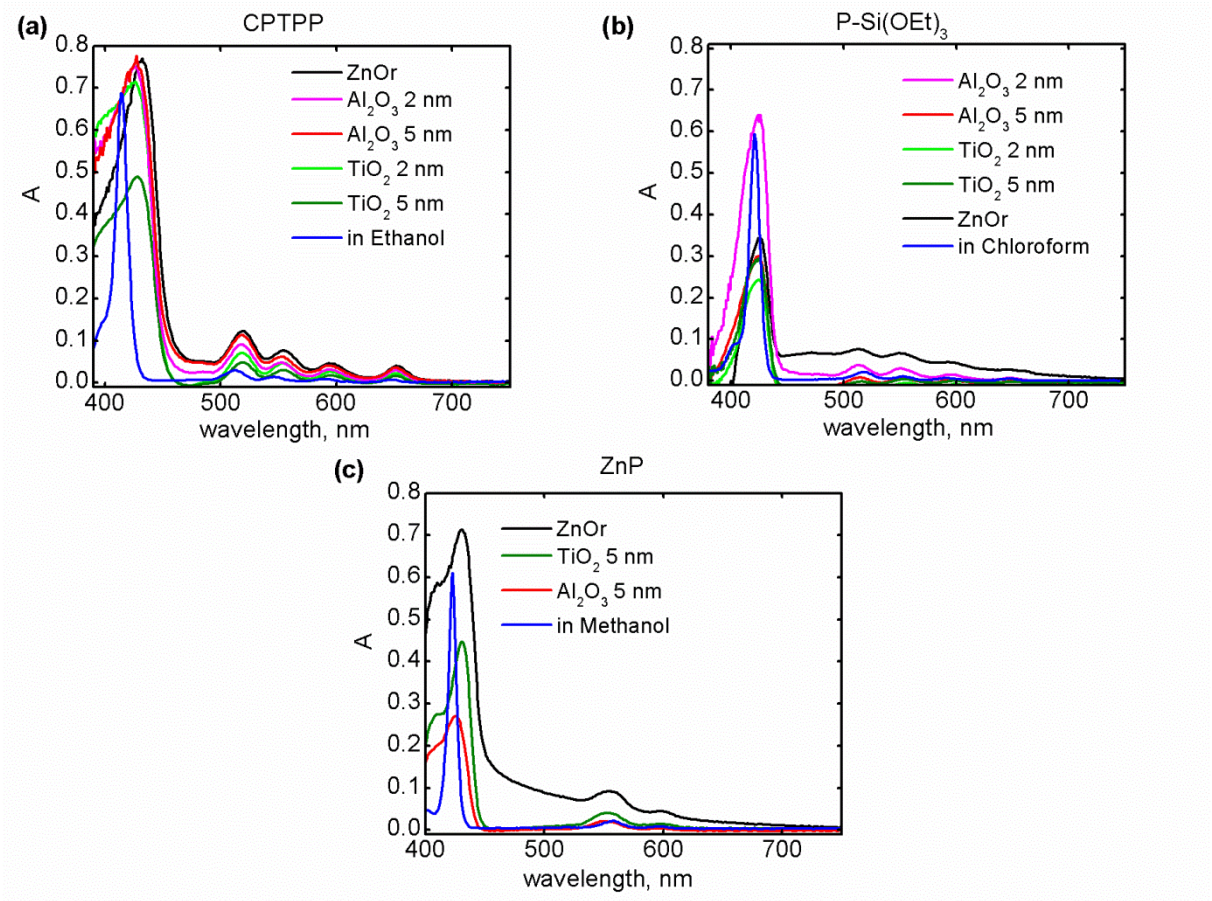

FIGURE 4.9 Absorption spectra of a) CPTPP, b) P-Si(OEt)$_3$ and c) ZnP SAMs on ZnOr, ZnOr|Al_2O_3 (2 or 5 nm) and ZnOr|TiO_2 (2 or 5 nm).

The binding mode of ZnP layer to semiconductors was studied by the FT-IR-ATR spectroscopy method. The ATR spectra of the solid ZnP powder and the ZnP bound to MO substrates are shown in Figure 4.10. The spectrum of solid ZnP has characteristic carboxylic acid stretching bands v(C=O) and v(C-O) at around 1700 and 1280 cm^{-1}, respectively. Upon binding these bands disappear and symmetric (v(COO^-_{as}) and asymmetric (v(COO^-_s) stretching bands of carboxylate groups appear at around 1400 and 1600 cm^{-1}. These characteristic features are observed when ZnP is bound to all studied substrates.

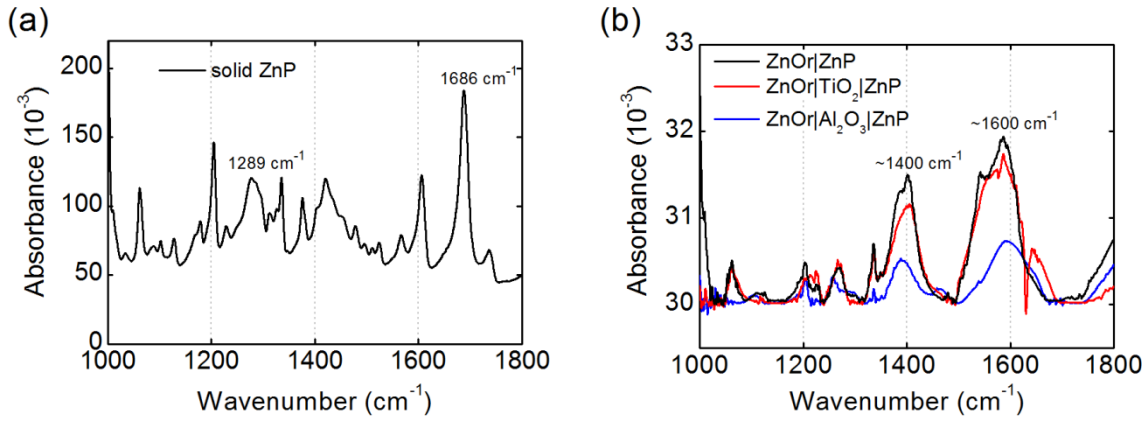

FIGURE 4.10 FT-IR-ATR spectra of a) ZnP powder, b) ZnOr|ZnP, ZnOr|TiO_2|ZnP and ZnOr|Al_2O_3|ZnP samples.

The FT-IR-ATR signal intensity is low in the case of ZnOr based samples, but still a clear difference to the spectrum of solid unbound ZnP is found. The disappearance of strong ν(C=O) band in the ZnP SAM spectra rules out the ester type binding mode and also indicates that no unbound ZnP is left on the metal oxide surfaces. The difference between the symmetric and asymmetric stretching bands of carboxylate group suggests that ZnP is covalently bound to all studied surfaces by bidentate binding mode.

4.3.2 Phthalocyanine monolayer and hole transporting film on ZnO

SEM images of the solid samples consisting of ZnPc monolayers assembled on ZnO nanorods covered with hole transporting material (P3HT or Spiro-OMeTAD) are shown in Figure 4.11.

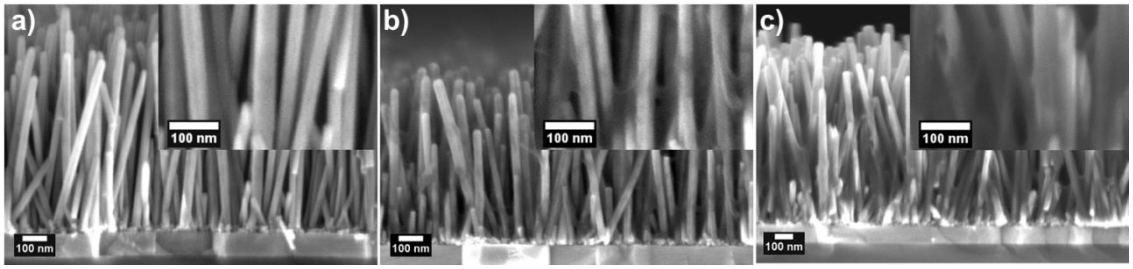

FIGURE 4.11 Cross section SEM images of a) ZnOr|ZnPc, b) ZnOr|ZnPc|P3HT, and c) ZnOr|ZnPc|Spiro-OMeTAD.

The spatial resolution of the SEM used in this study is limited to 5-10 nm, thus ZnPc SAM on ZnOr cannot be distinguished. However, P3HT and Spiro-OMeTAD layers fill relatively large volumes and are seen in the images as gray areas around and between

the ZnOr. As a result single nanorods are not seen in Figure 4.11b and c as clearly as in Figure 4.11a. SEM images illustrate that Spiro-OMeTAD infiltrates better to ZnOr compared to P3HT. This is expected since it has lower molecular weight and spatial size than P3HT.[90]

The absorption spectra of ZnPc in butanol and the studied samples are shown in Figure 4.12. The absorption maximum of the Q-band ZnPc in butanol is at 679 nm. ZnPc SAM on ZnOr has maximum at 681 nm and the spectrum is slightly broadened as compared to the solution spectrum, having bandwidths (FWHM) of 35 and 19 nm in SAM and butanol, respectively. Such a small shift in the absorption maximum position and only a minor increase in the band width indicates a relatively small degree of aggregation of ZnPc in SAM. As illustrated in Figure 4.11 and discussed in chapter 4.2.2, there is always variation in effective surface area of ZnOr which explains the observed difference in the ZnPc absorption between the samples. P3HT film has characteristic broad absorption in the range 400-620 nm. Film of Spiro-OMeTAD on ZnOr is almost transparent; the main absorption band around 390 nm is seen as a sharp absorbance rise towards shorter wavelengths starting from 450 nm.[91] The spectra of ZnOr|ZnPc|P3HT and ZnOr|ZnPc|Spiro are almost superposition of its components, but ZnPc Q band is red-shifted by 7 nm. The shift is an indication of the change in the environment of ZnPc SAM caused by the close contact to HTM.

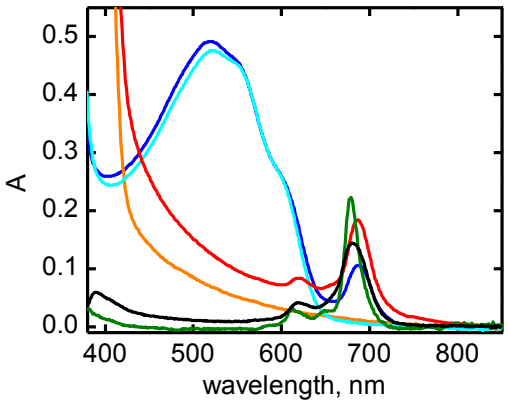

Figure 4.12 Absorption spectra of ZnPc in BuOH (gray), ZnOr|ZnPc (black), ZnOr|P3HT (cyan), ZnOr|ZnPc|P3HT (blue), ZnOr|Spiro-OMeTAD (orange), and ZnOr|ZnPc|Spiro-OMeTAD (red). Spectrum of ZnOr has been subtracted from each film structure.

4.4 Photoinduced processes at semiconductor-dye interface

Photoinduced interactions between the porphyrin SAMs and two semiconductors, ZnO and TiO_2, were studied. (II and III) The effect of semiconductor was investigated by modifying the ZnOr surface by a thin layer of TiO_2 or Al_2O_3 and by comparing interfacial ET kinetics on TiO_2 nanoparticle film and on TiO_2 coated ZnOr substrates. In most complex system, a layer of hole transporting material was added on top of the ZnO-zinc phthalocyanine nanostructure. (IV) The charge transfer reactions were followed both at ZnO-ZnPc and ZnPc-hole transporting material interfaces.

4.4.1 Role of the chromophore

The interactions at metal oxide-porphyrin SAM interfaces were monitored first by comparing emission intensities and fluorescence lifetimes of the SAMs. The aim was to find out, how the structure of arrangement of porphyrins in the SAM affects the photoinduced interfacial reactions. At the same time, it was possible to determine the optimum thickness for TiO_2 and Al_2O_3 modification layers. The steady state emission spectra of the porphyrin SAMs on ZnOr, ZnOr|TiO_2 and ZnOr|Al_2O_3 are shown in Figure 4.13.

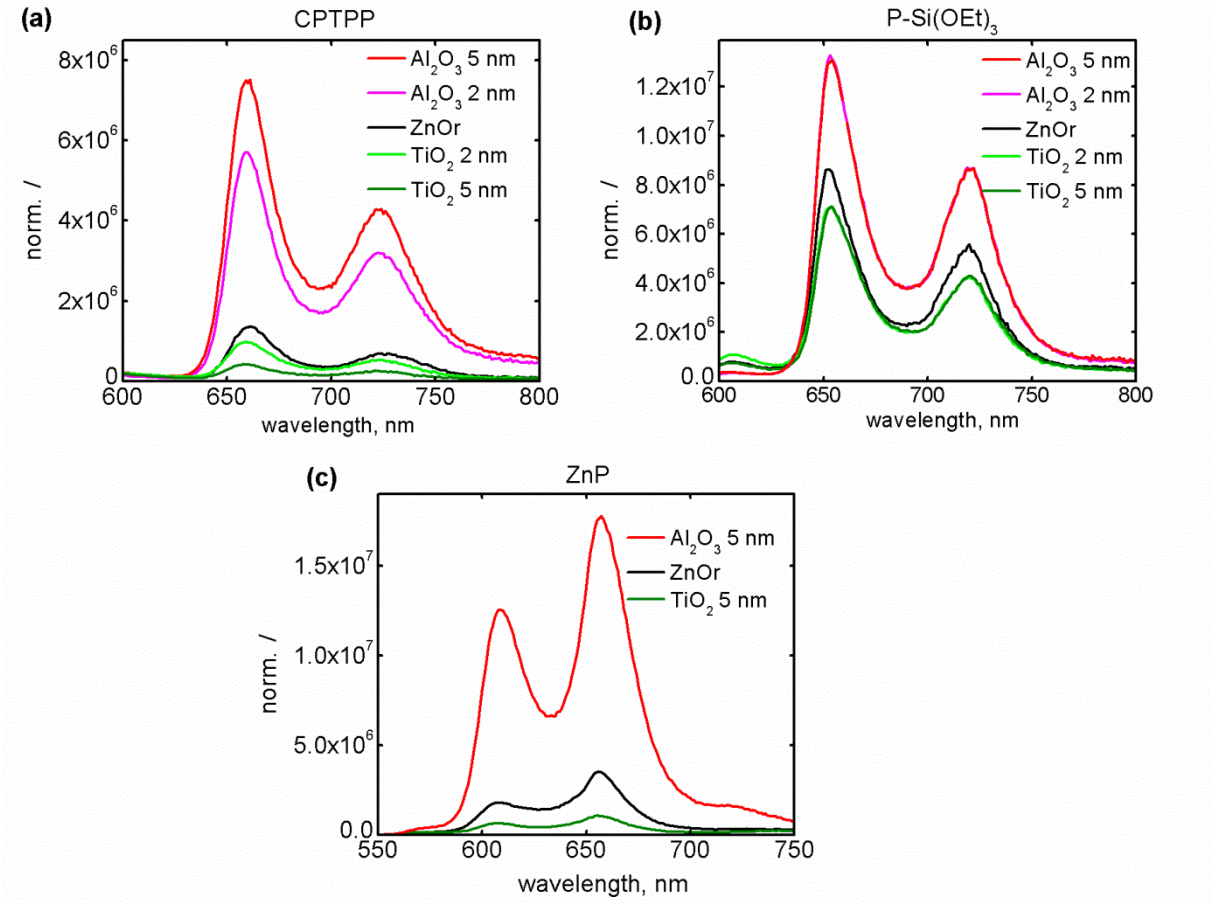

FIGURE 4.13 Normalized emission spectra with respect to the relative amount of the excitation light absorbed by the films of a) CPTPP, b) P-Si(OEt)$_3$, and c) ZnP SAMs on ZnOr, ZnOr|Al_2O_3 (2 or 5 nm) and ZnOr|TiO_2 (2 or 5 nm).

Even though all the porphyrins SAMs have compatible absorptions, the emission properties are quite different. P-Si(OEt)$_3$ SAM shows only a weak emission intensity dependence on the metal oxide properties compared to that of CPTPP and ZnP SAMs. The difference in the emission intensities of CPTPP and ZnP on ZnOr|Al_2O_3 (5 nm) and on ZnOr|TiO_2 (5 nm) are approximately 17 times, whereas there is only two times difference in the case of P-Si(OEt)$_3$. The weak dependence can be attributed to the relative long linker in P-Si(OEt)$_3$ resulting in an increased distance between the chromophore and the metal oxide and thus reduced the interaction between the two.[60]

Emission decays of the porphyrin SAMs on ZnOr, ZnOr|TiO_2 and ZnOr|Al_2O_3 were measured by TCSPC method and fitted with the bi-exponential fit model. The calculated average lifetimes together with relative emission intensities and lifetimes are presented in Table 4.2. The relative emission intensities and the average lifetimes were

normalized with respect to those on ZnOr|Al_2O_3 (5 nm), where only intra-molecular interactions are expected to occur.

TABLE 4.2 Average emission lifetimes (τ_{avg}) of CPTPP, P-Si(OEt)$_3$, and ZnP SAMs on metal oxides. χ^2 is weighted mean square deviation. Relative the emission intensities and lifetimes relative to sample on ZnOr|Al_2O_3 (5 nm) are presented in the last two columns.

	τ_{avg} (ns)	χ^2	rel. em. (660 nm)	rel. τ_{avg} (ns)
CPTPP				
ZnOr|Al_2O_3 (5 nm)	0.69	1.19	1.00	1.00
ZnOr|Al_2O_3 (2 nm)	0.59	1.29	0.77	0.86
ZnO	0.20	1.88	0.18	0.29
ZnOr|TiO_2 (2 nm)	0.21	1.74	0.13	0.30
ZnOr|TiO_2 (5 nm)	0.08	1.40	0.06	0.12
P-Si(OEt)$_3$				
ZnOr|Al_2O_3 (5 nm)	1.37	1.21	1.00	1.00
ZnOr|Al_2O_3 (2 nm)	1.62	1.16	1.01	1.18
ZnOr	1.04	1.65	0.61	0.76
ZnOr|TiO_2 (2 nm)	1.09	1.77	0.54	0.80
ZnOr|TiO_2 (5 nm)	1.11	1.72	0.55	0.81
ZnP				
ZnOr|Al_2O_3 (5 nm)	0.34	1.9	1.00	1.00
ZnOr	0.10	1.1	0.20	0.29
ZnOr|TiO_2 (5 nm)	0.12	1.4	0.06	0.35

CPTPP SAM shows a strong emission intensity and lifetime dependence on the type of metal oxide substrate; therefore it was selected as a model compound for the thickness optimization of the ZnOr modification layer (2 or 5 nm). A relatively thick layer of Al_2O_3 is expected to cancel all interfacial electronic interactions. The difference in the emission lifetimes of CPTPP SAM on the ZnOr|Al_2O_3 (2 and 5 nm) is rather small. Therefore

one may safely assume that 5 nm layer is thick enough to prevent the interactions and the emission quenching is exclusively due to CPTPP aggregation in the SAM. On the contrary, there is more than two-fold difference in the emission intensity and lifetime of CPTPP SAM on 2 and 5 nm TiO_2 layers. Based on these observations, a 2 nm layer of TiO_2 is not thick enough to switch surface properties completely from that of ZnO to TiO_2 one.

Another method to ensure complete ZnOr surface modification with 5 nm layer of Al_2O_3, DSSC experiments were performed using ZnP which is a well-studied sensitizer in DSSC.[54] The photocurrent-voltage characteristics are shown in Figure 4.14 and the performance parameters are summarized in Table 4.3. The efficiency of the ZnOr|Al_2O_3|ZnP solar cell is almost zero (η = 0.001%). On the other hand, the ZnOr|ZnP, ZnOr|ZnO, and ZnOr|TiO_2|ZnP cells have reasonable efficiencies compared to the low cell absorbance. Based on these results, 5 nm thick layers of Al_2O_3 and TiO_2 were concluded to be sufficient to modify the ZnO surface and were used in the further time-resolved absorption experiments.

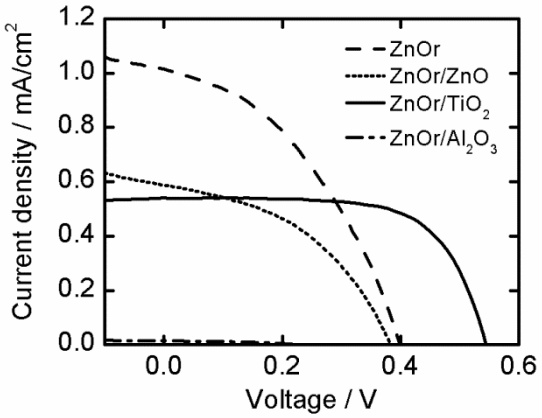

FIGURE 4.14 J-V characteristics DSSCs based on ZnOr photoanodes and ZnP sensitizer.

TABLE 4.3. Photovoltaic properties of the studied DSSCs.

Photoanode	J_{sc} **(mA/cm^2)**	U_{oc} **(V)**	***FF***	η **(%)**
ZnOr	1.0	0.40	0.42	0.17
ZnOr|ZnO	0.59	0.39	0.43	0.10
ZnOr|Al_2O_3	0.01	0.24	0.43	0.001
ZnOr|TiO_2	0.54	0.55	0.67	0.20

Estimation of the CPTPP, or specially ZnP SAM-metal oxide interactions by comparing emission lifetimes is not accurate. There is more than two fold difference in the relative emission intensities and lifetimes. This indicates that faster (< 70 ps) quenching processes may take place and those cannot be resolved by TCSPC method.

4.4.2 Role of the semiconductor

The photoinduced ultrafast processes at the semiconductor-ZnP interface, which were not resolved by TCSPC, were studied by the time-resolved absorption method. With the excitation at 560 nm, the singlet excited state is populated and it yields an instant rise of the TA signal at 660 nm as shown in Figure 4.15. The slower rise of the absorption at this wavelength can be attributed to the electron transfer from ZnP to metal oxide i.e. formation of ZnP cation. Only the decay of the signal observed for ZnOr|Al_2O_3|ZnP sample, therefore there is no ET from ZnP to the underlying semiconductor through Al_2O_3 layer.

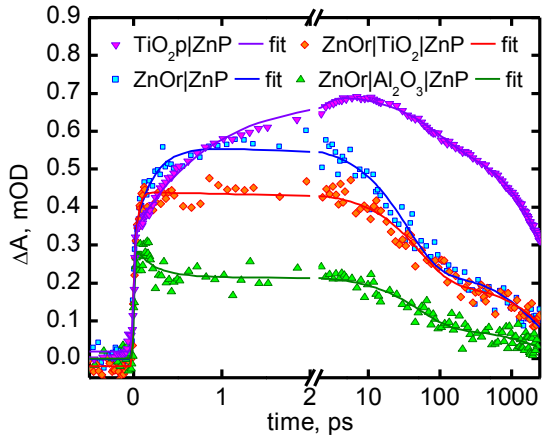

FIGURE 4.15 Transient absorption responses of the ZnP SAMs on metal oxides. The time scale is linear up to 2 ps and logarithmic after 2 ps. The signal intensity of sensitized TiO_2 nanoparticle film, TiO_2p|ZnP, is divided by the factor of ten to fit the scale.

Although 660 nm is the optimum wavelength for monitoring ZnP cation state, the singlet excited state also has a contribution to the TA response at this wavelength.[58,92] Thus the contributions of these two states cannot be separated totally. The decay profiles of the ZnOr|Al_2O_3|ZnP, ZnOr|TiO_2|ZnP, and ZnOr|ZnP in Figure 4.15 look roughly the same. However, TCSPC measurements summarized in Table 4.2 show that the lifetime of the ZnP singlet excited state is much shorter in ZnOr|TiO_2|ZnP, and ZnOr|ZnP samples than that in ZnOr|Al_2O_3|ZnP. Therefore the TA response of ZnOr|TiO_2|ZnP and ZnOr|ZnP at this delay time can be attributed to the ZnP cation state. In addition, the DSSC measurements (Table 4.3) suggest that the ET is very inefficient process in the case of ZnOr|Al_2O_3|ZnP. These three observations, i) the rise of the absorption at 660 nm in sub-picosecond time, ii) much shorter emission lifetime for ZnOr|TiO_2|ZnP and ZnOr|ZnP only, and iii) negligible photocurrent generation for ZnOr|Al_2O_3|ZnP, lead us to a conclusion that origin of the transient absorption decays of these systems at 660 nm are different, although the lifetimes shown in Table 4.4 are roughly the same. For ZnOr|TiO_2|ZnP and ZnOr|ZnP the signals at few ps delay and longer are mainly due to ZnP cation, whereas in the case of ZnOr|Al_2O_3|ZnP it arises from the singlet excited state. The signal intensities in the TA responses are rather weak thus the accuracy of the calculated lifetimes is approximately 30%.

TABLE 4.4 Lifetimes and amplitudes of decay components obtained from transient absorption decays. τ_1: formation of porphyrin radical cation, τ_2 and τ_3: two decay time constants.

sample	τ_1 **rise**	τ_2 **decay**	τ_3 **decay**
ZnOr|ZnP	0.3 ps	50 ps [60%]	2.3 ns [40%]
ZnOr|TiO_2|ZnP	< 0.2 ps, unresolved	50 ps [50%]	3.1 ns [50%]
ZnOr|Al_2O_3|ZnP	not formed	50 ps [60%]	2.5 ns [40%]
TiO_2p|ZnP	0.9 ps	84 ps [20%]	> 2 ns [80%]

The formation of ZnP cation after ET from excited ZnP to metal oxide is fastest in ZnOr|TiO_2|ZnP (< 0.2 ps). The reaction is slightly slower in ZnOr|ZnP (0.3 ps) but still much faster than in TiO_2|ZnP system (0.9 ps). This is a clear indication that the semiconductor nanostructure has a strong influence on the ET rate. The TiO_2 nanoparticle film is randomly packed and has grain boundaries and therefore electronic states differ from the bulk at every nanoparticle interface. On the contrary, one-dimensional ZnOr are single crystals and can provide a direct pathway for electron transport along the nanorods.[27] A 5 nm thick TiO_2 shell modifies the ZnOr surface electronic properties thus resulting in faster ET reaction (< 0.2 ps vs. 0.3 ps). The layer may be too thin to have well defined crystal structure, but is thick enough to change the electronic structure of the ZnOr surface. Although the band gaps of bulk ZnO and TiO_2 are very close to each other, TiO_2 has higher density of states than ZnO which is one reason for the faster ET rate.[6,63] The role of the surface electronic states in ET reaction rate has been under discussion.[93] It has been suggested that at ZnO-sensitizer interface the ET proceeds via an intermediate state of coupled electron-hole pair and this state is a major factor limiting the ET rate. The intermediate state is related to the ZnO properties because no stepwise ET was observed for the reference TiO_2 samples, and its origin remains still unclear. Moreover, it is known that the ET at the ZnP-semiconductor interface is sensitive to the molecule arrangement because the reaction takes place through the space.[58,62,94] The surfaces of the semiconductors are heterogeneous and despite similar sensitizing conditions, variation in the tilt angles as well as different types of the porphyrin aggregates are possible. So far, the effect of these factors on the ET is under discussion since experimental determination of exact molecular organization on semiconductor surface is extremely challenging task.[62]

Although the TiO_2 layer on ZnOr increases the ET rate, only a small difference in the charge recombination rate between the ZnOr|ZnP and ZnOr|TiO_2|ZnP was observed. Though the calculated longer lifetimes are somewhat different for these samples, there is no visible difference in the decay profiles (Figure 4.15). Addition of TiO_2 layer results in a small decrease in the amplitude of the ~50 ps decay component. Reasons for the decrease can be the higher conductivity of the ZnOr core than that of the TiO_2 shell and the slightly lower energy level of the ZnO conduction band of than that of TiO_2.[95] Therefore photo-injected electrons in the ZnOr|TiO_2|dye structures move across the TiO_2 layer into ZnOr and the recombination rate is mainly determined by ZnOr. Among all measured samples, the charge recombination is slowest in TiO_2p|ZnP. One possible explanation can be that the bulk carrier mobility of ZnO and TiO_2 contributes to the rate of charge recombination – the faster charge migration in ZnO makes the charge recombination faster. The latter should not have a negative effect on the solar cell performance, since the higher carrier mobility is also beneficial for the efficient charge transport to the external circuit.

4.4.3 Role of hole transporting material

Charge transfer reactions in a three component systems consisting of zinc phthalocyanine monolayer on ZnO nanorods and a layer of hole transporting material (HTM) on top were studied by transient absorption method. The reaction steps after selective excitation of ZnPc and P3HT were identified and corresponding rate constants were determined.

At first, electron injection from excited ZnPc to ZnO nanorods without HTM was followed. In principle, the ET is the first order reaction for each individual ZnPc molecules and should follow exponential decay kinetics, but the measured signal is cumulative response of large number ZnPc molecules in SAM on the ZnO nanorods and there is variation in local environment between ZnPcs, which converts exponential decay kinetics to a sum of exponents with time constants randomly distributed around some average value. A mathematical model to deal with the case was developed and successfully applied to analyze ET in molecular films, and it was used in this study as well.[96,97] A tentative interpretation of the results shown in Figure 4.16 is the electron injection from the photo-excited ZnPc to ZnO nanorods with 1.4 ps average time constant and the charge recombination with 850 ps average time constant. The important spectral features to distinguish between the singlet excited state and ZnPc cation, $ZnPc^+$, are the featureless excited state absorption in the ranges 470-600 nm and 900-1300 nm and the bands located at 550 nm and 850 corresponding to the ZnPc cation.[98,99]

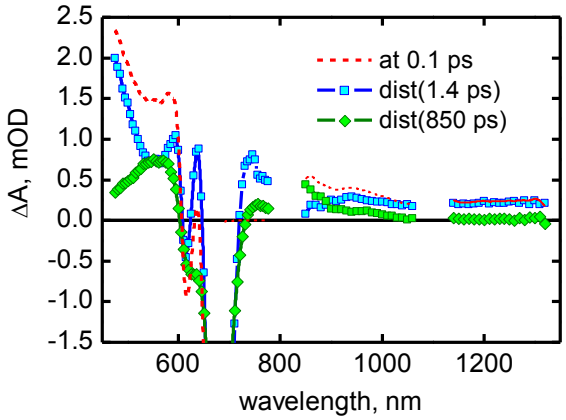

FIGURE 4.16 Decay component (line+symbol) and time resolved (dashed line) spectra of ZnOr|ZnPc. The spectrum of singlet excited ZnPc is shown by the red dashed line and the spectrum of the ZnPc cation by the green line.

Time resolved transient absorption spectra of ZnOr|P3HT were obtained with excitation at 500 nm and are shown in Figure 4.17. Except of very fast subpicosecond spectral perturbations in the 600-650 nm range the main features of the transient absorption response is the bleaching of the ground state absorption of P3HT at < 630 nm and smoothly rising absorbance in the NIR region (850-1050 nm). To fit the data with reasonable accuracy, a five exponential model had to be used. 0.2, 0.8, 7, 100 and > 10 ns time constants have equal contribution to the decay and rather minor differences in corresponding decay component spectra. Considering a very wide divergence of the time constants, the results characterization by a single (average) lifetime is rather meaningless.

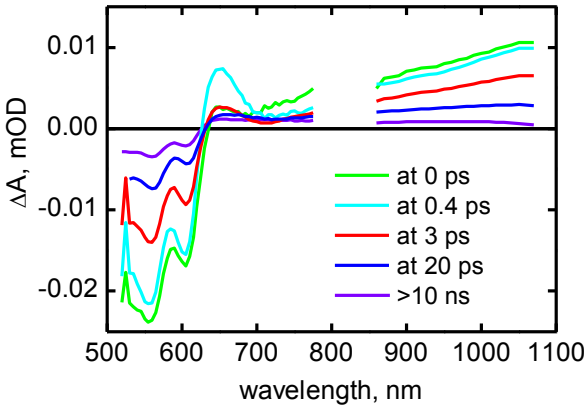

FIGURE 4.17 Calculated time resolved spectra of ZnOr|P3HT. Excitation wavelength was 500 nm.

The transient absorption response of ZnOr|ZnPc|P3HT to the excitation at 680 nm (selective excitation of ZnPc) is more complex, but can be understood at qualitative level by comparing the responses at different wavelengths and time resolved spectra at different delay time, as presented in Figure 4.18. A distinct feature of the transient absorption response is that the recovery of the ZnPc ground state absorption (decay at 707 nm) coincides with bleaching development of the P3HT ground state (decay at 551 nm and negative band at 500-600 nm).

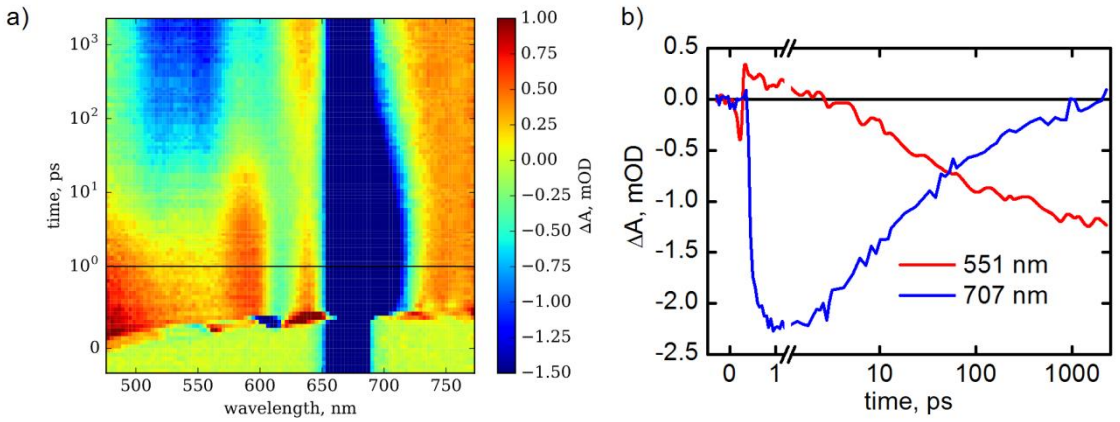

FIGURE 4.18 2D map of TA signals of a) ZnOr|ZnPc|P3HT, and b) transient absorption decay curves of the same sample at 551 and 707 nm (linear time scale till 1 ps and logarithmic after 1 ps). Excitation wavelength was 680 nm.

Since P3HT is not excited directly, the only possibility how it gets involved is considering electronic interaction between the ZnPc layer and P3HT. The energy transfer can be excluded from the very beginning since excited state energy of P3HT is much higher in energy than that of ZnPc. The interaction cannot be only an electron transfer between the photo-excited ZnPc and P3HT since as P3HT gets involved, ZnPc returns to the ground state. Thus, the most reasonable and simple explanation is two step electron transfer as denoted in the Scheme (1).

(1) $ZnOr \mid ZnPc^{*} \mid P3HT \rightarrow ZnOr^{-} \mid ZnPc^{+} \mid P3HT \rightarrow ZnOr^{-} \mid ZnPc \mid P3HT^{+}$

The second reaction step is hole transfer from the ZnPc cation to P3HT. Based on this reaction scheme the transient absorption data were fitted globally using a model consisting of a picosecond exponent to account for the primary electron transfer from ZnPc singlet excited state, a distributed decay to account for the hole transfer from $ZnPc^{+}$ to P3HT, and a long-lived exponent accounting for the long-lived holes in $P3HT^{+}$. Results

of the fit are presented in Figure 4.19. The obtained exponential lifetime (1.8 ps) for the ZnOr|ZnPc* → $ZnOr^-|ZnPc^+$ reaction correlates well with that obtained for the sample without P3HT layer (1.4 ps). The hole transfer is much faster than the charge recombination at the ZnOr|ZnPc interface (30 ps *vs*. 850 ps), which means that an efficient hole transfer can be expected in this system.

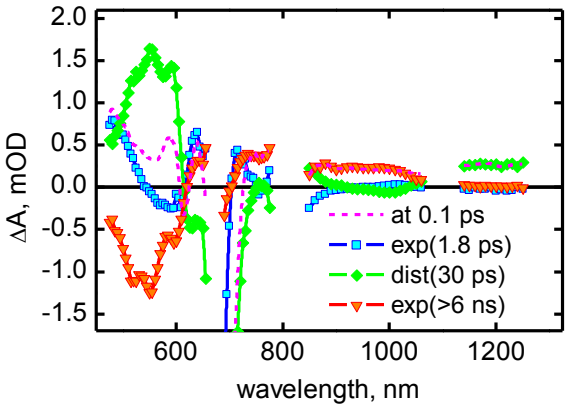

FIGURE 4.19 Transient absorption decay component spectra (lines with symbols) and time resolved spectrum at 0.1 ps after excitation (dashed line) of ZnOr|ZnPc|P3HT.

Results of global fitting of the transient absorption data of ZnOr|ZnPc|Spiro are presented in Figure 4.20. Reference sample ZnOr|Spiro was also measured but no signal was detected with 680 nm excitation.

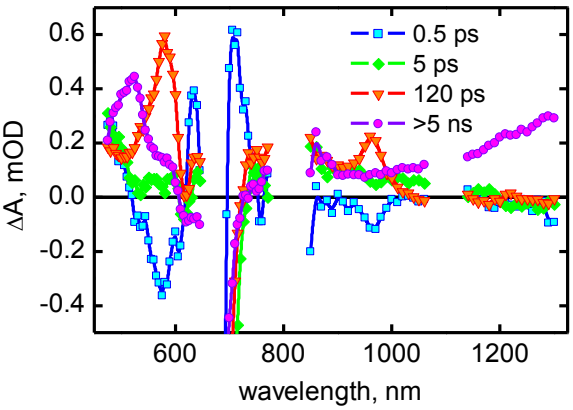

FIGURE 4.20 Decay component spectra of ZnOr|ZnPc|Spiro. Excitation wavelength was 680 nm.

The essential features of the transient absorption spectra are (1) bands at 575 and 960 nm which are formed and decayed with 0.5 and 120 ps time constants, respectively, (2) a component with time constant > 5 ns which has a band at 525 nm, and (3) a rising absorption at > 1100 nm. The most reasonable assignment of the bands at 575 and 960 nm is to ZnPc anion[100] and of the bands at 525 nm and the broad band at 1150-1350 nm is to Spiro-oMeTAD cation.[91,101,102] The scheme (2) describes the reaction steps.

(2) $ZnOr|ZnPc^*|Spiro \rightarrow ZnOr|ZnPc^-|Spiro^+ \rightarrow ZnOr^-|ZnPc|Spiro^+$

The primary charge separation takes place between the excited ZnPc* and Spiro-OMeTAD with roughly 0.5 ps time constant, and the following electron injection from ZnPc anion to ZnOr takes place with 120 ps time constant.

According to the results obtained for ZnOr|ZnPc, the electron transfer from the photo-excited ZnPc to ZnOr takes place in the same time domain (1.4 ps) as the first reaction in the scheme (2). Therefore one can expect a competing relaxation pathway to be:

(3) $ZnOr|ZnPc^*|Spiro \rightarrow ZnOr^-|ZnPc^+|Spiro \rightarrow ZnOr^-|ZnPc|Spiro^+$

In this case the 5 ps time constant shown in Figure 4.20 can be attributed to the second reaction step ($ZnOr|ZnPc^+|Spiro \rightarrow ZnOr|ZnPc|Spiro^+$) and the time constant 0.5 ps is the total relaxation time of the singlet excited state (ZnPc*) via both channels, $ZnOr|ZnPc^*|Spiro \rightarrow ZnOr|ZnPc^-|Spiro^+$ and $ZnOr|ZnPc^*|Spiro \rightarrow ZnOr^-|ZnPc^+|Spiro$, respectively.

Selective excitation of P3HT in ZnOr|ZnPc|P3HT structure is achieved using 500 nm as excitation wavelength. As shown in Figure 4.21 the TA response of ZnOr|ZnPc|P3HT is at short delay time (0.3 ps) almost identical to the response of ZnOr|P3HT. The only noticeable difference is the negative absorption in the ZnPc Q band region at 690 nm which appears after few picoseconds delay time.

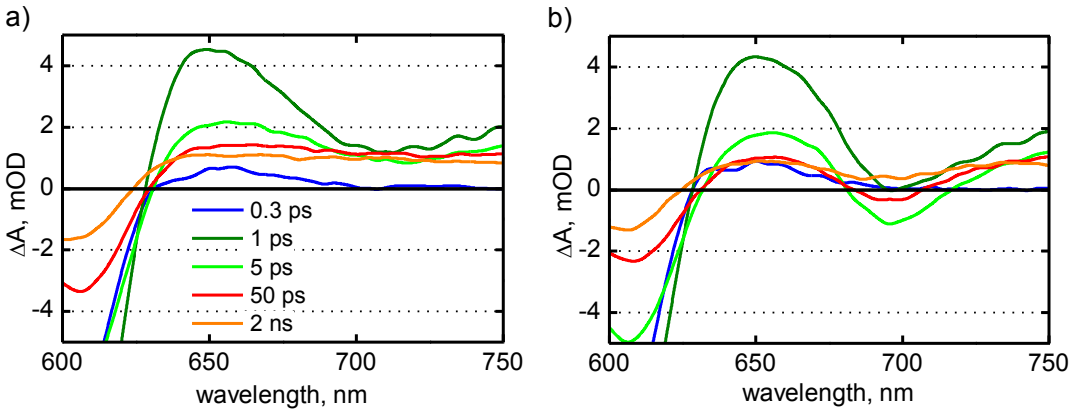

FIGURE 4.21Time resolved spectra of a) ZnOr|P3HT and b) ZnOr|ZnPc|P3HT after 500 nm excitation. The delay times indicated in a) applies also in b).

There are two possible explanations for the negative band around 690 nm, an energy transfer[103] ZnPc|P3HT* → ZnPc*|P3HT and an electron transfer ZnPc|P3HT* → $ZnPc^-|P3HT^+$. In both cases, a long distance charge separated state $ZnOr^-|ZnPc|P3HT^+$ is expected to be formed in few tens – few hundred picoseconds time domain. If there would be energy transfer leading to formation of a ZnPc excited species, the charge separated state is formed in 30 ps time constant (Figure 4.19). In the case of the electron transfer, the corresponding time constant is 120 ps like it was observed for ZnOr|ZnPc|Spiro (Figure 4.20) and ZnPc anion band centered at 575 nm should be seen in the TA spectrum. However, there were no sign of ZnPc anion neither in the visible nor in the infrared part of the spectrum and the recovery of ZnPc ground state bleaching at 690 nm agrees well with 30 ps time constant. Therefore the energy transfer is the proposed mechanism for the interaction between excited P3HT and ZnPc.

The charge generation in the studied systems, ZnOr|ZnPc|P3HT and ZnOr|ZnPc|Spiro-OMeTAD was different but the both mechanisms are known for this type of hybrid structures.[104] Figure 4.22 summarizes the results from the transient absorption measurements. In ZnOr|ZnPc|P3HT system, the excitation of either ZnPc or P3HT leads to an electron transfer from ZnPc to ZnO nanorods which is followed by the hole transfer to P3HT. The first charge transfer step in ZnOr|ZnPc|Spiro is electron transfer from Spiro-OMeTAD to ZnPc followed by electron transfer from the ZnPc anion to ZnO nanorods.

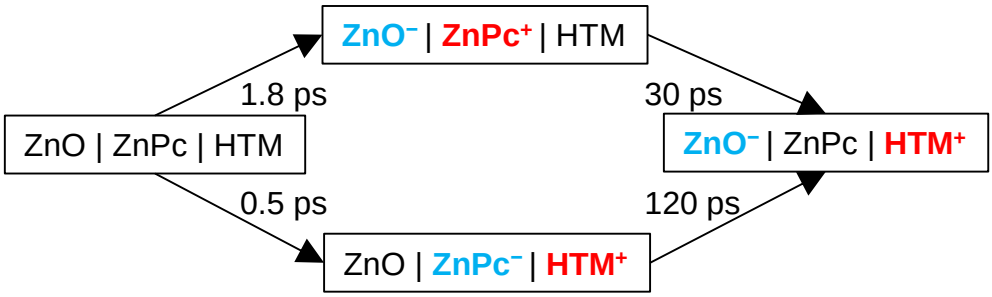

FIGURE 4.22 Schematic illustration of the main charge generation mechanism in the studied system. ZnO corresponds ZnO nanorods, HTM corresponds to hole transporting material, P3HT or Spiro-OMeTAD. Also the measured time constants for each reaction step are shown.

The reason for the different charge generation mechanism in such similar samples is interesting question to be discussed. Only few studies were undertaken to compare these HTM and the comparison was based on the final solar cell performance leaving the photoinduced charge generation mechanism unanswered.[90] In general, the prerequisite for the hole transfer from excited ZnPc to HTM is the lower lying HOMO level for ZnPc than that for HTM. Apparently both HTMs have higher HOMO level than ZnPc but reported values for P3HT[66,67] and Spiro-OMeTAD[67,105,106] are too close to each other to explain different reaction pathway (-4.8 to -5.2 eV vs. -4.9 to -5.1 eV). Another important factor can be the distance between ZnPc and HTM. Spiro-OMeTAD is relatively small molecule, at least if compared to P3HT which has hexyl chains surrounding the hole conducting polythiophene core. If the alkyl chains are separating ZnPc and P3HT core, the short intermolecular distance in ZnPc|Spiro interface is the reason for the primary electron transfer at ZnPc|Spiro interface.

Both ZnOr|ZnPc|P3HT and ZnOr|ZnPc|Spiro-OMeTAD are promising designs for solid state solar cell applications. ZnOr can be considered as an ideal template to build interpenetrating network of electron and hole conducting materials where the ZnOr would conduct the electrons to an electrode. In order to prepare a reasonably efficient device the surface area of ZnOr should be optimized and the infiltration of the HTM material into ZnOr should be so complete that no rods are pointing towards the metal electrode.

4.5 Outlook and prospects

New materials are a prerequisite to improve the existing ones and to design new photovoltaic devices. The actual devices are rather complex structures having several interfaces where the photoinduced reactions are taking place. In this thesis, the study of the reactions triggered by light was started from the simple sample configurations. At the same time, the method to prepare semiconductor nanostructures suitable for solar cell applications was developed. Finally, the photoinduced reactions were studied both at semiconductor-organic and organic-organic interfaces in ultrashort time domain from femtoseconds to nanoseconds.

Atomic layer deposition is a versatile method to prepare aluminum doped zinc oxide films which were tested as transparent electrodes in organic solar cells. The films were successfully deposited at 150 °C and probably even lower temperatures are possible to use to deposit the same films onto flexible polymer substrates. The film morphology depended on the deposition temperature but it did not affect the device performance.

Once the usability of ZnO semiconductor for solar cell applications was confirmed, the focus of the studies was turned to ZnO nanostructures with special attention paid to photoinduced interfacial interactions. The sample requirement for the time resolved absorption measurements is high enough absorption thus monolayers of porphyrins and phthalocyanine derivatives were formed on arrays of ZnOr. Therefore a routine procedure was developed to produce desired ZnOr substrates. As was pointed out in the results and also observed experimentally recently, the seed layer formation is the most critical factor in order to get well-aligned ZnOr. The actual energy alignments in the ZnO-dye systems can be determined by the advanced spectroscopy methods such as X-ray and ultraviolet photoemission spectroscopy.[107,108]

Electron transfer and charge recombination from ZnP and ZnPc to ZnOr were observed to take place in the same time domain (0.3 ps vs 1.4 ps and 1.2 ns vs. 0.85 ns). Taking into account the different absorption spectrum of ZnP and ZnPc, the time constants correlate reasonably well with the reported power conversion efficiencies in DSSCs. ZnP has been studied by other groups as a sensitizer in TiO_2 DSSC with liquid electrolyte for which power conversion efficiency of 4.4 % was reported.[54] ZnPc studied here was synthesized during this thesis and is not yet used as sensitizer is DSSC. However, the power conversion efficiency for similar type of phthalocyanine is reported to be 3.5 %.[109]

The results of photoinduced interfacial interactions presented here are good continuation for the study of the same phenomena in solutions and in organized, solid films. A natural continuation for this study would be the preparation of hybrid solar cells based on the studied structures. The time-resolved spectroscopy results suggest that the primary electron transfer reaction from the excited dye to semiconductor is fast and is not limiting the final device performance. Instead, the future studies should focus on optimization of the efficient hole collection and transport in the system. Also by using the model sample template developed in this thesis, the photoinduced interactions at ZnO-dye interface could be studied using other organic chromophores such as perylene derivatives.[110,111]

5 Conclusions

This thesis was devoted to the preparation and the photochemical studies of hybrid semiconductor-organic structures. The main focus was at fundamental characterization of the photoinduced reactions in the structures, though some photovoltaic devices were prepared to demonstrate the functionality of the structures in practice. The following conclusions can be drawn based on the reported results:

1. Aluminum doped zinc oxide films are superior transparent electrodes in photovoltaic applications compared to traditionally used ITO. Atomic layer deposition method enables to prepare films at relatively low temperatures with accurate control of doping level.

2. ZnO nanorod arrays are versatile model substrates to study electronic interactions at semiconductor-organic interface. The hydrothermal growth method of nanorods provides reasonable control of morphology, and electronic properties of nanorods can be further altered by atomic layer deposition of alternative semiconductors.

3. Knowledge of the photoinduced charge transfer reaction mechanisms and their rates at the semiconductor-dye interface is obtained by ultrafast spectroscopy methods. Semiconductor surface properties have a clear influence to electron transfer rate. A thin layer of TiO_2 on ZnO nanorods accelerated charge separation at semiconductor- zinc porphyrin interface but does not affect charge recombination.

4. Array of ZnO nanorods is a versatile platform to construct both DSSC-like and organic bulk heterojunction like solar cells. This was demonstrated by first functionalizing nanorods by zinc phthalocyanine monolayer and covering the structure by a layer of hole transporting material. A cascade of photoinduced reactions in organic layers results in electron localized in ZnO and hole in the hole transporting layer within few hundreds of picoseconds.

References

1. IEA, Energy Technology Perspectives OECD/IEA, **2014**. http://www.iea.org/publications/freepublications/publication/Solar_Energy_Perspectives2011.pdf 19.2.2016

2. IEA, Technology Roadmap, Solar Photovoltaic Energy OECD/IEA, **2014**. http://www.iea.org/publications/freepublications/publication/TechnologyRoadmapSolarPhotovoltaicEnergy_2014edition.pdf, 19.2.2016

3. Hoppe, H.; Saricifti, N.S. Organic solar cells: An overview. *J. Mater. Res.* **2004**, *19*, 1924-1945.

4. Hagfeldt, A.; Boschloo, G.; Sun, L.; Kloo, L.; Pettersson, H. Dye-sensitized solar cells. *Chem. Rev.* **2010**, *110*, 6595-6663.

5. Zhao, Z.; Liu, H.; Chen, S. Charge transport at the metal oxide and organic interface. *Nanoscale* **2012**, *4*, 7301-7308.

6. Thavasi, V.; Renugopalakrishnan, V.; Jose, R., Ramakrishna, S. Controlled electron injection and transport at materials interfaces in dye sensitized solar cells. *Mater. Sci. Eng. R* **2009**, *63*, 81-99.

7. Prezhdo, O.V.; Duncan, W.R.; Prezhdo, V.V. Photoinduced electron dynamics at the chromophore-semiconductor interface: A time-domain *ab initio* perspective. *Prog. Surf. Sci.* **2009**, *84*, 30-68.

8. Listorti, A.; O´Regan, B.; Durrant, J.R. Electron transfer dynamics in dye-sensitized solar cells. *Chem. Mat.* **2011**, *23*, 3381-3399.

9. Grätzel, M. Photoelectrochemical cells *Nature* **2001**, 414, 338-344.

10. Liu, H.; Avrutin, V.; Izyumskaya, N.; Özgür, Ü.; Morkoc, H. Transparent conducting oxides for electrode applications in light emitting and absorbing devices. *Superlattices Microstr.* **2010**, *48*, 458-484.

11. Rao, C.N.R.; Lingampalli, S.R. Generation of hydrogen by visible light-induced water splitting with use of semiconductors and dyes. *Small* **2016**, *12*, 13-23.

12. Faria, J.C.D.; Campbell, A.J.; McLachlan, M.A. ZnO Nanorod Arrays as Electron Injection Layers for Efficient Organic Light Emitting Diodes. *Adv. Funct. Mat.* **2015**, *25*, 4657-4663.

13. Ellmer, K.; Klein, A. ZnO and its applications, in K. Ellmer, A. Klein, B. Rech (Eds.), Transparent Conductive Zinc Oxide, Spinger-Verlag, Berlin Heidelberg, **2008**, 1-34.

14. Adurodija, F.O. Lasers in thin film processing, in H.S. Nalwa (Eds.), Handbook of Thin Film Materials, Academic Press, San Diego, **2002**, 162.

15. Tanaka, A.; Hirata, M.; Kiyohara, Y.; Nakano, M.; Omae, K.; Shiratani, M.; Koga, K. Review of pulmonary toxicity of indium compounds to animals and humans. *Thin Solid Films* **2009**, 518, 2934-2936.

16. White, M.S.; Olson, D.C.; Shaheen, S.E.; Kopidakis, N.; Ginley, D.S. Inverted bulk-heterojunction organic photovoltaic device using a solution-derived ZnO underlayer. *Appl.Phys.Lett.* **2006**, *89*, 1435171.

17. Sun, N.; Fang, G.; Qin, P.; Zheng, Q.; Wang, M.; Fan, X.; Cheng, F.; Wan, J.; Zhao, X. Bulk heterojunction solar cells with NiO hole transporting layer based on AZO anode. *Sol. Energy Mat. Sol. Cells* **2010**, *94,* 2328-2331.

18. Alberti, A.; Pellegrino, G.; Condorelli, G.G.; Bongiorno, C.; Morita, S.; La Manga, A.; Miyasaka, T. Efficiency enhancement in ZnO:Al-based dye-sensitized solar cells structured with sputtered TiO_2 blocking layers. *J. Phys. Chem. C* **2014**, *118*, 6575-6585.

19. Lujala, V.; Skarp, J.M.; Tammenmaa, M.; Suntola, T. Atomic layer epitaxy growth of doped zinc oxide films from organometals. *Appl. Surf. Sci.* **1994**, *82-83*, 34-40.

20. Zhang, Q.; Dandeneau, C.S.; Zhou, X.; Cao, G. ZnO nanostructures for dye-sensitized solar cells. *Adv. Mat.* **2009**, *21*, 4087-4108.

21. Xu, S.; Wang, Z.L. One-dimensional ZnO nanostructures: solution growth and functional properties. *Nano Research* **2011**, *4*, 1013-1098.

22. McCune, M.; Zhang, W.; Deng, Y. High efficiency dye-sensitized solar cells based on three-dimensional multilayered ZnO nanowire arrays with “caterpillar-like” structure. *Nano Lett.* **2012**, *12*, 3656-3662.

23. Xu, X.L.; Chen, Y.; Ma, S.Y.; Mao, Y.Z.; Wang, T.; Bian, H.Q. CTAB-assisted synthesis of unique 3D ZnO and the acetone sensing properties. *Mater. Lett.* **2015**, *151*, 5-8.

24. Wang, Y.; Yang, J.; Jia, H.; Yu, M.; Jin, H. Self-assembled urchin-like ZnO nanostructures fabricated by electrodeposition-hydrothermal method. *J. Alloys Comp.* **2016**, *665*, 62-68.

25. Bielinski, A.R.; Kazyak, E.; Schlepütz, C.M.; Joon Jung, H.; Wood, K.N.; Dasgupta, N.P Hierarchical ZnO nanowire growth with tunable orientations on versatile substrates using atomic layer deposition seeding. *Chem. Mat.* **2015**, *27*, 4799-4807.

26. Ko, S.H.; Lee, D.; Kang, H. W.; Nam, K.H.; Yeo, J.Y.; Hong, S.J.; Grigoropoulos, C.P.; Sung, H.J. Nanoforest of hydrothermally grown hierarchical ZnO nanowires for a high efficiency dye-sensitized solar cell. *Nano Lett.* **2011**, *11*, 686-671.

27. Galoppini, E.; Rochford, J.; Chen, H.; Saraf, G.; Lu, Y.; Hagfeldt, A.; Boschloo, G. Fast electron transport in metal organic vapor deposition grown dye sensitized ZnO nanorod solar cells. *J. Phys Chem. B* **2006**, *110*, 16159-16161.

28. Xu, C.; Wu, J.; Desai, U.V.; Gao, D Multilayer assembly of nanowire arrays for dye-sensitized solar cells. *J. Am. Chem. Soc.* **2011**, *133*, 8122-8125.

29. Anta, J. A.; Guillen, E.; Tena-Zaera, R. ZnO-based dye sensitized solar cells. *J. Phys. Chem. C* **2012**, *116*, 11413-11425.

30. Weintraub, B.; Zhou, Z.; Li, Y.; Deng, Y. Solution synthesis of one-dimensional ZnO nanomaterials and their applications. *Nanoscale* **2010**, *2*, 1573-1587.

31. Vayssieres, L.; Keis, K.; Lindquist, S.-E.; Hagfeldt, A. Purpose-built anisotropic metal oxide material: 3D highly oriented microrod array of ZnO. *J. Phys. Chem. B* **2001**, *105*, 3350-3352.

32. Na, J.S.; Gong, B.; Scarel, G.; Parsons, G.N. Surface polarity shielding and hierarchical ZnO nano-architectures produced using sequential hydrothermal crystal synthesis and thin film atomic layer deposition. *ACS Nano* **2009**, *3*, 3191-3199.

33. Liu, J.; She, J.; Deng, S.; Chen, J.; Xu, N. Ultrathin seed-layer for tuning density of ZnO nanowire arrays and their field emission characteristics. *J. Phys. Chem. C* **2008**, *112*, 11685-11690.

34. Guo, M.; Diao, P.; Cai, S. Hydrothermal growth of well-aligned ZnO nanorod arrays: dependence of morphology and alignment ordering upon preparing conditions, *J. Solid State Chem.* **2005**, *178*, 1864-1873.

35. Guo, M.; Diao, P.; Wang, X.; Cai, S. The effect of hydrothermal growth temperature on preparation and photoelectrochemical performance of ZnO nanorod array films. *J. Solid State Chem.* **2005**, *178*, 3210-3215.

36. Andrés Vergés, M.; Mifsud, A.; Serna, C.J. Formation of rod-like microcrystals in homogenous solutions. *J. Chem. Soc. Faraday Trans.* **1990**, *86*, 959-963.

37. Guillemin, S.; Rapenne, L.; Roussel, H.; Sarigiannidou, E.; Brémond, G.; Consonni, V. Formation mechanismc of ZnO nanowires: the crucial role of crystal orientation and polarity. *J. Phys. Chem. C* **2013**, *117*, 20738-20745.

38. Pakkala, A.; Putkonen, M., *Atomic layer deposition*, in: P.M. Martin (Eds.) Handbook of Deposition Technologies for Films and Coatings, **2010**, Elsevier Inc. 364-391.

39. Ritala, M.; Leskelä, M.; *Atomic layer deposition*, in: H.S. Nalwa (Eds.), Handbook of Thin Film Materials, San Diego **2002**, Academic Press. 103–159.

40. http://www.beneq.com/sites/default/files/documents/nSILVER%20brochure.pdf, 19.2.2016

41. Puurunen, R.L.; Surface chemistry of atomic layer deposition: A case study for trimethylaluminum/water process. *J. Appl. Phys.* **2005**, *97*, 121301.

42. Schreiber, F. Structure and growth of self-assembling monolayers. *Prog. Surf. Sci.* **2000**, *65*, 151-256.

43. Love, J.C.; Estroff, L.A.; Kriebel, J.K.; Nuzzo, R.G.; Whitesides, G.M. Self-assembled monolayers of thiolates on metals as a form of nanotechnology. *Chem. Rev.* **2005**, *105*, 1103-1169.

44. Galoppini, E. Linkers for anchoring sensitizers to semiconductor nanoparticles. *Coord. Chem. Rev.* **2004**, *248*, 1283-1297.

45. Zhang, L.; Cole, J.M. Anchoring groups for dye-sensitized solar cells. *ACS Appl. Mater. Interfaces* **2015**, *7*, 3427-3455.

46. Zhang, B.; Kong, T.; Xu, W.; Su, R.; Gao, Y. Cheng, G. Surface functionalization of zinc oxide by carboxyalkylphosphonic acid self-assembled monolayers. *Langmuir* **2010**, *26*, 4514-4522.

47. Baik, C.; Kim, D.; Kang, M.-S.; Kang, S. O.; Ko, J.; Nazeeruddin, M. K.; Grätzel, M. Organic dyes with a novel anchoring group for dye-sensitized solar cell applications. *J. Photochem. Photobiol. A* **2009**, *201*, 168-174.

48. Gómez-Ortíz, N.M.; Idígoras, J.; Guillén, E.; Hernández, A.; Sastre-Santos, A.; Fernández, F.; Anta, J.A.; Oskam, G. Influence of dye chemistry and electrolyte solution on interfacial processes at nanostructured ZnO in dye-sensitized solar cells. *J. Photochem. Photobiol. A.* **2013**, *204*, 26-33.

49. López-Duarte, I.; Wang, M.; Humphry-Baker, R.; ince, M.; Martínez-Díaz, M.V.; Nazeerudding, M.K.; Torres, T.; Grätzel, M. Molecular Engineering of Zinc Phthalocyanines with Phosphinic Acid Anchoring Groups. *Angew. Chem. Int. Ed.* **2012**, *51*, 1895-1898.

50. Imahori, H.; Hayashi, S.; Hayashi, H.; Oguro, A.; Eu, S.; Umeyama, T.; Matano, Y. Effects of porphyrin substituents and adsorption conditions on photovoltaic properties of porphyrin-sensitized TiO_2 cells. *J. Phys. Chem. C* **2009**, *113*, 18406-18413.

51. Thyagarajan, S.; Galoppini, E.; Persson, P.; Giaimuccio, J.M.; Meyer, G.J. Large footprint pyrene chromophores anchored to planar and colloidal metal oxide thin films. *Langmuir* **2009**, *25*, 9219-9226.

52. Anderson, N.A.; Lian, T. Ultrafast electron transfer at the molecule-semiconductor nanoparticle interface. *Ann. Rev. Phys. Chem.* **2005**, *56*, 491-519.

53. Kalyanasundaram, K.; Grätzel, M. Applications of functional transition metal complexes in photonic and optoelectronic devices. *Coord. Chem. Rev.* **1998**, *77*, 347-414.

54. Imahori, H.; Matsubara, Y.; Iijima H.; Umeyama, T.; Matano, Y.; Ito, S.; Tkachenko, N.V.; Lemmetyinen, H. Effects of *meso*-diarylamino group of porphyrin sensitizers in dye-sensitized solar cells on optical, electrochemical and photovoltaic properties. *J. Phys. Chem. C* **2010**, *114*, 10656-10665.

55. Hart, A.S.; KC, C.B.; Gobeze, H.B.; Sequeira, L.R.; D´Souza, F. Porphyrin-sensitized solar cells: effect of carboxyl anchor group orientation on the cell performance. *ACS Appl. Mater. & Interf.* **2013**, *5*, 5314-5323.

56. Sharma, D.; Steen, G.; Korterik, J.P.; García-Iglesias, M.; Vázquez, P.; Torres, T.; Herek, J.L.; Huijser, A. Impact of the anchoring ligand on electron injection and recombination dynamics at the interface of novel asymmetric push-pull zinc phthalocyanines and TiO_2. *J. Phys. Chem. C* **2013**, *117*, 25397-25404.

57. Lu, H.-P.; Tsai, C.-Y.; Yen, W.-N.; Hsich, C.-P.; Lee, C.-W.; Yeh, C.-Y, Diau, E.W.-G. Control of dye aggregation and electron injection for highly efficient porphyrin sensitizers adsorbed on semiconductor films with varying ratios of coadsorbate. *J. Phys. Chem. C* **2009**, *113*, 20990-20997.

58. Imahori, H.; Kang, S.; Hayashi, H.; Haruta, M.; Kurata, H.; Isoda, S.; Canton, S.E.; Infahsaeng, Y.; Kathiravan, A.; Pascher, T.; Chábera, P.;Yartsev, A.P.; Sundström, V. Photoinduced charge carrier dynamics of Zn-porphyrin-TiO_2 electrodes: the key role of charge recombination for solar cell performance. *J. Phys. Chem. A* **2011**, *115*, 3679-3690.

59. Matsuzaki H.; Murakami T.N.; Masaki N.; Furube A.; Kimura M.; Mori S. Dye aggregation effect on interfacial electron-transfer dynamics in zinc phthalocyanine-sensitized solar cells. *J. Phys Chem. C* **2014**, *118*, 17205-17212.

60. Luo, L.; Lin, C.-J.; Tsai, C.-Y.; Wu, H.-P.; Li, L.-L.; Lo, C.-F.; Lin, C.-Y.; Diau, E.W.-G. Effects of aggregation and electron injection on photovoltaic performance of porphyrin-based solar cells with oligo(phenylethynyl) links inside TiO_2 and Al_2O_3 nanotube arrays. *Phys. Chem. Chem. Phys.* **2010**, *12*, 1064-1071.

61. Rochford, J.; Chu, D.; Hagfeldt, A.; Galoppini, E. Tetrachelate porphyrin chromophores for metal oxide semiconductor sensitization: effect of the spacer length and anchoring group position. *J. Am. Chem. Soc.* **2007**, *129*, 4655-4665.

62. Ye, S.; Kathiravan, A.; Hayashi, H.; Tong, Y.; Infahsaeng, Y.; Chabera, P.; Pascher, T.; Yartsev, A.P.; Isoda, S.; Imahori, H.; Sundström, V. Role of adsorption structures of Zn-porphyrin on TiO_2 dye-sensitized solar cells studied by sum frequency generation vibrational spectroscopy and ultrafast spectroscopy. *J. Phys. Chem. C* **2013**, *117*, 6066-6080.

63. Asbury, J.B.; Hao, E.; Wang, Y.; Ghosh, H.N.; Lian, T. Ultrafast electron transfer dynamics from molecular adsorbates to semiconductor nanocrystalline thin films *J. Phys. Chem. B* **2001**, *105*, 4545-4557.

64. Huss, A.S.; Bierbaum A.; Chitta, R.; Ceckanowicz, D.J.; Mann, K.R.; Gladfelter, W.L.; Blank, D.A. Tuning electron transfer rates via systematic shifts in the acceptor state density using size-selected ZnO colloids. *J. Am. Chem. Soc.* **2010**, *132*, 13963-13965.

65. Lu, L.; Zheng, T.; Wu, Q.; Schneider, A.M.; Zhao, D.; Yu, L. Recent advances in bulk heterojunction polymer solar cells. *Chem. Rev.* **2015**, *115*, 12666-12731.

66. Lee, H.J.; Leventis, H.C.; Haque, S.A.; Torres, T.; Grätzel, M.; Nazeeruddin, M.K. Panchromatic response composed of hybrid visible-light absorbing polymers and near-IR absorbing dyes for nanocrystalline TiO_2-based solid-state solar cells. *J. Power Sources* **2011**, *196*, 596-599.

67. Docampo P.; Guldin S.; Leijtens T.; Noel N.K.; Steiner U.; Snaith H.J. Lessons learned: from dye-sensitized solar cells to all-solid-state hybrid devices. *Adv. Mat.* **2014**, *26*, 4013-4030.

68. Bach U.; Lupo D.; Comte P.; Moser J.E.; Weissörtel F.; Salbeck J.; Spreitzer H.; Grätzel M. Solid-state dye-sensitized mesoporous TiO2 solar cells with high photon-to-electron conversion efficiencies *Nature* **1998**, *395*, 583-585.

69. Lambert, J.B.; Shurvell, H.F.; Lightner, D.A.; Cooks, R.G. *Organic structural spectroscopy* Prentice-Hall, New Jersey **1998**, 152-172.

70. Nazeeruddin, Md.K.; Humphry-Baker, R.; Officer, D.L.; Campbell, W.M.; Burrell, A.K.; Grätzel, M. Application of metalloporphyrins in nanocrystalline dye-sensitized solar cells for conversion of sunlight into electricity. *Langmuir* **2004**, *20*, 6514-6517.

71. Rochford, J.; Galoppini, E. Zinc(II) tetraarylporphyrins anchored to TiO_2, ZnO and ZrO_2 nanoparticle films through rigid-rod linkers. *Langmuir* **2008**, *24*, 5366-5374.

72. Tkachenko, N.V. Pump-probe, in *Optical spectroscopy materials and instrumentations* Elsevier Science, Amsterdam **2006**, 135-153.

73. Lehtivuori, H.; Efimov, A.; Lemmetyinen, H.; Tkachenko, N.V. Distributed decay kinetics of charge separated state in solid film. *Chem. Phys. Lett.* **2007**, *437*, 238-242.

74. Park, S.-H. K.; Lee, J.-I.; Hwang, C.-S.; Chu, H.Y. Characteristics of organic light emitting diodes with Al-doped ZnO anode deposited by atomic layer deposition. *Jpn. J. Appl. Phys.* **2005**, *44*, L242-L245.

75. Lim, J.; Lee, C. Effects of substrate temperature on the microstructure and photoluminescence properties of ZnO thin films prepared by atomic layer deposition.*Thin Solid Films* **2007**, *515*, 3335-3338.

76. Kowalik, I.A.; Guziewich, E.; Kopalko, K.; Yatsunenko, S.; Wójcik-Glodowska, A.; Godlewski, M.; Dłuzewski, P.; Łusakowska, E.; Paszkowicz, W. Stuctural and optical properties of low-temperature ZnO films grown by atomic layer deposition with diethylzinc and water precursors. *J. Cryst. Growth* **2009**, *311*, 1096-1101.

77. Elam, J.W.; Sechrist, Z.A.; George, S.M. ZnO/Al_2O_3 nanolaminates fabricated by atomic layer deposition: growth and surface roughness measurements. *Thin Solid Films* **2002**, *414*, 43-55.

78. Na, J.-S.; Peng, Q.; Scarel, G.; Parsons, G.N. Role of gas doping sequence in surface reactions and dopant incorporation during atomic layer deposition of Al-doped ZnO. *Chem. Mater.* **2009**, *21*, 5585-5593.

79. Na, J.-S.; Scarel, G.; Parsons, G.N. In situ analysis of dopant incorporation, activation, and film growth during thin film ZnO and ZnO:Al atomic layer deposition. *J. Phys. Chem. C* **2010**, *114*, 383-388.

80. Yun, J.-J.; Jung, H.-S.; Kim, S.-H.; Han, E.-M.; Chlorophyll-layer-inserted poly(3-hexyl-thiophene) solar cell having a high light-to-current conversion efficiency up to 1.48%. *Appl. Phys. Lett.* **2005**, *87*, 123102.

81. Chiş, V.; Mile, G.; Ştiufiuc, R.; Leopold, N.; Oltean, M. Vibrational and electronic structure of PTCDI and melamine-PTCDI complexes. *J. Mol. Struct.* **2009**, *924-926*, 47-53.

82. Vivo, P.; Ojala, M.; Chukharev, V.; Efimov, A.; Lemmetyinen, H. Role of a phthalocyanine-fullerene dyad in multilayered organic solar cells. *J. Photochem. Photobiol. A* **2009**, *203*, 125-130.

83. Krebs, F.C.; Norrman, K. Analysis of the failure mechanism for a stable organic photovoltaic during 10 000 h of testing. *Prog. Photovolt.: Res. Appl.* **2007**, *15*, 697-712.

84. Jørgensen, M.; Norrman, K.; Krebs, F.C. Stability/degradation of polymer solar cells. *Sol. Energy Mater. Sol. Cells* **2008**, *91*, 686-714.

85. Wang, M.; Wang, J.; Chen, W.; Cui, Y.; Wang, L. Effect of preheating and annealing temperatures on quality characteristics of ZnO thin film prepared by sol-gel method. *Mater. Chem. Phys.* **2006**, *97*, 219-225.

86. Greene, L. E.; Law, M.; Tan, D. H.; Montano, M.; Goldberger, J.; Somorjai, G.; Yang, P. General route to vertical ZnO nanowire arrays using textured ZnO seeds. *Nano Lett.* **2005**, *5*, 1231-1236.

87. Ma, T.; Guo, M.; Zhang, M.; Zhang, Y.; Wang, X. Density-controlled hydrothermal growth of well-aligned ZnO nanorod arrays. *Nanotechnology* **2007**, *29*, 035605.

88. Vayssieres, L. Growth of arrayed nanorods and nanowires of ZnO from aqueous solutions. *Adv. Mater.* **2003**, *15*, 464-466.

89. Gonzalez-Valls, I.; Yu, Y.; Ballesteros, B.; Oro, J.; Lira-Cantu, M. Synthesis conditions, light intensity and temperature effect on the performance of ZnO nanorods-based dye sensitized solar cells. *J.Power Sources* **2011**, *196*, 6609-6621.

90. Yang, L.; Cappel, U.B.; Unger, E.L.; Karlsson, M.; Karlsson, K.M.; Gabrielsson, E.; Sun, L., Boschloo, G., Hagfeldt, A., Johansson, E.M.J. Comparing Spiro and P3HT hole conductors in efficient solid state dye-sensitized solar cells. *Phys. Chem. Chem. Phys.* **2012**, *14*, 779-789.

91. Burschka, J.; Dualeh, A.; Kessler, F.; Baranoff, E.; Cevey-Ha, N.-L.; Yi, C.; Nazeeruddin, M.K.; Grätzel, M. nTris(2-(1 H -pyrazol-1-yl)pyridine)cobalt(III) as p-type dopant for organic semiconductors and its application in highly efficient solid-state dye-sensitized solar cells. *J. Am. Chem. Soc.* **2011**, *133*, 18042-18045

92. Gasyna, Z.; Browett, W.R.; Stillman, M.J. π-cation-radical formation following visible light photolysis of porphyrins in frozen solution using alkyl chlorides or quinones as electron acceptors. *Inorg. Chem.* **1985**, *24*, 2440-2447.

93. Strothkämper, C.; Bartelt, A.; Sippel, P.; Hannappel, T.; Schütz, R.; Eichberger, R. Delayed electron transfer through interface states in hybrid ZnO/organic-dye nanostructures. *J. Phys. Chem. C* **2013**, *117*, 17901-17908.

94. Niskanen, M.; Kuisma, M.; Cramariuc, O.; Golovanov, V.; Hukka, T.I.; Tkachenko, N.; Rantala, T. Porphyrin adsorbed on the (1010) surface of the wurtzite structure

of ZnO-conformation induced effects on the electron transfer characteristics. *Phys. Chem. Chem. Phys.* **2013**, *15*, 17408-17418.

95. Law, M.; Greene, L.M.; Radenovic, A.; Kuykendall, T.; Liphardt, J.; Yang, P. ZnO-Al_2O_3 and ZnO-TiO_2 core-shell nanowire dye-sensitized solar cells. *J. Phys. Chem.* **2006**, *110*, 22652-22663.

96. Stranius, K.; George, L.; Efimov, A.; Ruoko, T.-P.; Pohjola, J.; Tkachenko, N.V. Photophysical study of a self-assembled donor-acceptor two-layer film on TiO_2. *Langmuir* **2015**, *31*, 944-952.

97. Lehtivuori, H.; Kumpulainen, T.; Efimov, A.; Lemmetyinen, H.; Kira, A.; Imahori, H.; Tkachenko, N.V. photoinduced electron transfer in langmuir−blodgett monolayers of double-linked phthalocyanine−fullerene dyads. *J. Phys. Chem. C* **2008**, *112*, 9896-9902.

98. Fukuzumi, S.; Ohkubo, K.; Ortiz, J.; Gutiérrez, A.M.; Fernandez-Lázaro, F.; Sastre-Santos, A. Formation of a long-lived charge-separated state of a zinc phthalocyanine-perylenediimide dyad by complexation with magnesium ion. *Chem. Comm.* **2005**, *30*, 3814-3816.

99. Guldi, D.M.; Zilbermann, I.; Gouloumis, A.; Vázquez, P.; Torres, T. Metallophthalocyanines: Versatile electron-donating building blocks for fullerene dyads. *J. Phys. Chem. B* **2004**, *108*, 18485-18494.

100. Mack, J.; Stillman, M.J. Photochemical formation of the anion radical of zinc phthalocyanine and analysis of the absorption and magnetic circular dichroism spectral data. Assignment of the optical spectrum of [ZnPc(-3)]-. *J. Am. Chem. Soc.* **1994**, *116*, 1292-1304.

101. Cappel, U.B.; Gibson, E.A.; Hagfeldt, A.; Boschloo, G. Dye regeneration by Spiro-MeOTAD in solid state dye-sensitized solar cells studied by photoinduced absorption spectroscopy and spectroelectrochemistry. *J. Phys. Chem. C* **2009**, *113*, 6275-6281.

102. Kim, H.-S.; Lee, C.-R.; Im, J.-H.; Lee, K.-B.; Moehl, T.; Marchioro, A.; Moon, S.-J.; Humphry-Baker, R.; Yum, J.-H.; Moser, J.E.; Grätzel, M.; Park, N.-G. Lead iodide perovskite sensitized all-solid-state submicron thin film mesoscopic solar cell with efficiency exceeding 9%. *Scientific Reports* **2012**, *2*, 591.

103. Humphry-Baker, N.; Driscoll, K.; Rao, A.; Torres, T.; Snaith, H.J.; Friend, R.H. Time-evolution of poly(3-hexylthiophene) as an energy relay dye in dye-sensitized solar cells. *Nano Lett.* **2012**, *12*, 634-639.

104. Howard, I.A.; Meister, M.; Baumeier, B.; Wonneberger, H.; Pschirer, N.; Sens, R.; Bruder, I.; Li C.; Müllen, K.; Andrienko, D.; Laquai, F. Two channels of charge generation in perylene monoimide solid-state dye-sensitized solar cells. *Adv. Energy Mat.* **2014**, *4*, 1300640.

105. Driscoll, K., Fang, J., Humphry-Baker, N., Torres, T., Huck, W.T.S., Snaith, H.J., Friend, R.H. Enhanced photoresponse in solid-state excitonic solar cells via resonant energy transfer and cascaded charge transfer from a secondary absorber. *Nano Lett.* **2010**, *10*, 4981-4988.

106. Game, O.; Singh, U.; Kumari, T.; Banpurkar, A.; Ogale, S. ZnO(N)-Spiro-MeOTAD hybrid photodiode: an efficient self-powered fast-response UV (visible) photosensor. *Nanoscale* **2014**, *6*, 503-513.

107. Rangan, S.; Katalinic, S.; Thorpe, R.; Bartynski, R.A.; Rochford, J.; Galoppini, E. Energy level alignment of a zinc(II) tetraphenylporphyrin dye adsorbed onto TiO_2(110) and ZnO(1120) surfaces. *J. Phys. Chem. C* **2010**, *114*, 1139-1147.

108. Rangan, S.; Coh, S.; Bartynski, R.A.; Chitre, K.P.; Galoppini, E.; Jaye, C.; Fisher, D. Energy alignment, molecular packing and electronic pathways: zinc(II) tetraphenylporphyrin derivatives adsorbed on TiO_2(110) and ZnO(11-20) surfaces. *J. Phys. Chem. C* **2012**, *116*, 23921-23930.

109. Cid, J. J.; Yin, J.-H.; Jang, S.-R.; Nazeeruddin, M. K.; Martinez-Ferrero, E.; Palomares, E.; Ko, J.; Grätzel, M.; Torres, T., Molecular Cosensitization for Efficient Panchromatic Dye-Sensitized Solar Cells. *Angew. Chem. Int. Ed.* **2007**, *46*, 8358-8362.

110. Ahmed, Z.; George, L.; Hiltunen, A.; Lemmetyinen, H.; Hukka, T.; Efimov, A. Synthesis and study of electrochemical and optical properties of substituted perylenemonoimides in solutions and on solid surfaces. *J. Mater. Chem. A* **2015**, *3*, 13332-13339.

111. Sariola-Leikas, E.; Ahmed, Z.; Vivo, P.; Ojanperä, A.; Lahtonen, K.; Saari, J.; Valden, M.; Lemmetyinen, H.; Efimov, A. Color bricks: building of highly organized and strongly absorbing multi-component arrays of terpyridyl-perylenes on metal oxide surfaces. *Chem. – Eur. J.* **2016**, *22*, 1501-1510.

ORIGINAL PAPERS

I

ALUMINUM DOPED ZINC OXIDE FILMS GROWN BY ATOMIC LAYER DEPOSITION FOR ORGANIC PHOTOVOLTAIC DEVICES

by

Hanna Hakola, Tapio Niemi, Antti Tukiainen, Helge Lemmetyinen and Nikolai Tkachenko, 2010

Solar Energy Materials and Solar Cells vol. 94, 1379-1383

Solar Energy Materials & Solar Cells 94 (2010) 1379–1383

Contents lists available at ScienceDirect

Solar Energy Materials & Solar Cells

journal homepage: www.elsevier.com/locate/solmat

Aluminum doped zinc oxide films grown by atomic layer deposition for organic photovoltaic devices

Hanna Saarenpää [a,*], Tapio Niemi [b], Antti Tukiainen [b], Helge Lemmetyinen [a], Nikolai Tkachenko [a]

[a] Department of Chemistry and Bioengineering, Tampere University of Technology, P.O. Box 541, FIN-33101 Tampere, Finland
[b] Optoelectronics Research Centre, Tampere University of Technology, P.O. Box 692, FIN-33101 Tampere, Finland

ARTICLE INFO

Article history:
Received 9 February 2010
Received in revised form
30 March 2010
Accepted 4 April 2010
Available online 24 April 2010

Keywords:
Aluminum doped zinc oxide
Atomic layer deposition
Organic solar cells

ABSTRACT

Aluminum doped zinc oxide (AZO) films were studied as an alternative transparent electrode material to indium tin oxide (ITO) in organic photovoltaic devices. The AZO films were prepared by atomic layer deposition from diethylzinc, water and trimethylaluminum precursors. The same number of deposition cycles resulted in 170 and 90 nm thick films at deposition temperatures of 150 and 250 °C, respectively. Uniform films with wedge-shaped crystallites were observed at both temperatures. The functionality of the AZO electrodes in photovoltaic applications was tested using known organic photoactive layers. Devices with AZO electrode showed comparable performance to the reference device where ITO was used as transparent electrode. Moreover, the devices with AZO electrode were stable in open air showing no degradation during 40 days time interval.

1. Introduction

Transparent conductive oxides (TCO) are widely used as electrodes in thin film photovoltaic devices such as solar cells and light emitting diodes. Among TCO films indium tin oxide (ITO) is most used because of its combination of technologically important properties [1]. However, the development of other semiconductors is important because availability of ITO is limited, which makes it an expensive material. Moreover, indium is harmful for the environment [2,3] and for humans [4]. When considering the total environmental aspects and recycling of the organic solar cell the thin layers of electrode and active materials become minor factors since the weight fraction is very small compared to, e.g., the carrier substrate [5]. Zinc oxide (ZnO) is attractive alternative for ITO and has received great attention in recent years. The main advantages of ZnO are low materials costs and prerequisites for large-area technology [6]. An n-type conductivity of ZnO can be increased by doping with trivalent atom, such as aluminum, gallium or indium [7]. In photovoltaic applications ZnO is used as a buffer layer or, when doped, as a transparent conductor [2,3,8–12]. ZnO thin films can be prepared by a variety of methods, including sputtering [2,3,10,13], pulsed laser deposition [14] and chemical vapor deposition [15]. Recently ZnO films are prepared by novel techniques such as solution coating/printing [16,17]. If cost effective, low-temperature process for the deposition of ZnO and other TCOs on large-area substrates is considered, atomic layer deposition (ALD) is an attractive deposition method. ALD is the chemical vapor deposition technique based on alternate pulsing of the precursor gases and vapors onto the reaction chamber and self-terminating gas–solid reactions. Gas-phase reactions are prevented by the inert gas purge between the precursor pulses and the film thickness is controlled by the number of reaction cycles. Films can be easily doped by switching a fraction of deposition cycles to precursor containing a dopant. The self-limiting nature of the growth yields conformal films with accurate thickness control and relatively straightforward scale-up. Major drawback of ALD is generally rather low growth rate since at a best case only one atomic layer is deposited during one cycle. This can be partly compensated by scaling up the process and expressing the productivity in terms of film volume [18]. Method was developed by Suntola and co-workers in the 1970s for the fabrication of thin films for electroluminescent flat panel displays [19]. Nowadays ALD has a wide range of applications including catalysts, sensor technology and microelectronics. More detailed description of the method and its applications can be found elsewhere [20–22].

This work has a few motivations. First one is to find a cost effective way to fabricate TCO. Secondly, materials differ in their work functions and their adhesion to organic layers may vary. Therefore, it is of fundamental interest to study the effect of the TCO electrode on organic solar cell performance. Finally, the particular interest to ZnO TCO layers deposited by ALD method is driven by the fact that ZnO layers can be deposited at relatively low temperature (<150 °C) using reactive, volatile organometallic precursors which opens possibility to design structures with alternating organic-TCO layers.

* Corresponding author. Tel.: +358 3 3115 2002; fax: +358 3 3115 2108.
E-mail address: hanna.saarenpaa@tut.fi (H. Saarenpää).

0927-0248/$ - see front matter © 2010 Elsevier B.V. All rights reserved.
doi:10.1016/j.solmat.2010.04.006

In this work aluminum doped zinc oxide (AZO) films grown by ALD were studied as light transparent electrodes in photovoltaic applications. A series of known photoactive layers of polyhexylthiophene and perylene diimide derivatives [23] were deposited on top of AZO electrodes and their performance was compared with similar structures deposited on ITO electrodes. Also the stability of the devices was tested.

2. Experimental

Depositions of the AZO films were carried out in a flow-type reactor F-120 manufactured by ASM-Microchemistry Ltd. Diethylzinc (DEZ) and trimethylaluminum (TMA) purchased from Strem Chemicals Inc. were used as zinc and aluminum precursors, respectively. In both cases water was used as an oxygen source and nitrogen (99.999%) as a carrier and purging gas. During the process the pressure inside the reactor was about 10 mbar. Pulsing times of the precursors were 0.7 s for DEZ and water and 0.4 s for TMA. Nitrogen purges were 1.0 s long. In order to reduce film resistivity, the ZnO was doped by aluminum at relative level of 2.8% [24]. Two different procedures were used for AZO deposition on optical grade glass substrates. In the first method the deposition was performed at 150 °C. After 35 cycles of DEZ/water pulses one cycle of TMA/water pulses was introduced into the reactor. This series was repeated 26 times in order to deposit 170 nm thick film. Because the last deposition cycle was TMA/water the top surface layer of the film is expected to be aluminum oxide (AZO 1). In the second method the deposition temperature was 250 °C. The deposition cycles were the same as in the first method, but followed by 5 cycles of DEZ/water pulses after the last TMA/water pulse. In this case ZnO is expected to be the surface layer (AZO 2). Due to lower growth rate of AZO at higher temperatures the film thickness is only 90 nm for the same number of cycles as in the first method [24,25]. The lower growth rate was observed previously and was attributed to the increased decomposition of water at higher temperatures and therefore the density of hydroxyl groups on the surface is decreased [18,21,24]. Before deposition of the active organic layers AZO films were cleaned from the dust in ultrasonic bath using 2-propanol as a solvent. Plates were dried under vacuum at 120 °C for 60 min.

The reference device was fabricated on ITO-coated glass substrate (Pgo Germany) with sheet resistance of 8 Ω/□. Before deposition of the active layers ITO plates were cleaned carefully in ultrasonic bath in acetone, chloroform, sodium dodecyl sulphate (40 mg/l), distilled water and 2-propanol. Plates were dried under vacuum at 150 °C for 60 min.

All organic compounds were commercially available and used without purification. PHT (regioregular poly(3-hexyl thiophene-2,5-diyl, purchased from Rieke Metals) was spin coated at 2000 rpm for 60 s from a 2 g/l chloroform solution and annealed under vacuum at 120 °C for 30 min. The thickness of the PHT film was estimated from the steady-state absorption spectra calibrated by WYKO NT1100 profilometer. PTCDI (3,4,9,10 perylene-tetracarboxylic diimide, purchased from Alfa Aesar) and Alq3 (tris(8-hydroxyquinoline) aluminum, purchased from Sigma Aldrich) were deposited by thermal evaporation in BOC Edwards Auto-306 evaporation chamber. The thickness of the PTCDI and Alq3 layers were monitored during evaporation process using quartz crystals calibrated by optical profilometer. Finally, approximately 50 nm thick Au electrodes were thermally evaporated through a mask. The active areas of resulting photovoltaic devices (the overlapping areas between TCO bottom electrodes and top gold electrodes) were approximately 3 and 1 mm^2 for AZO and ITO devices, respectively. Samples were measured and stored in air at room temperature.

Table 1
Structures of the studied devices.

Device	Cell structure
1	AZO 1 | PTCDI | PHT | Alq3 | Au
2	AZO 2 | PTCDI | PHT | Alq3 | Au
3	ITO | PHT | PTCDI | Alq3 | Au
4	AZO 1 | PHT | PTCDI | Alq3 | Au

The structures of the devices are shown in Table 1. The thicknesses for the AZO 1 and 2 films were 170 and 90 nm, respectively, and 40, 20 and 6 nm for PTCDI, PHT and Alq3 films, respectively. PHT was used as an electron donor and PTCDI as an electron acceptor layer. The role of the Alq3 layer was to block the diffusion of Au atoms into the active layer [26]. Device 3 was prepared for the reference and the characteristics of the structure have been studied earlier [23].

Absorption spectra of the samples were measured by Shimadzu UV-360 spectrophotometer. Surface morphology was studied with Carl Zeiss Ultra 55 field emission scanning electron microscope (SEM) and Veeco dimension 3100 atomic force microscope (AFM). The resistivities of the AZO films were measured by multimeter applying gold plated stripe electrodes to the samples. Current–voltage (I–V) characteristics in dark and under simulated AM 1.5 (1000 W/m^2) sunlight illumination were measured by Agilent E5272A source/monitor unit. AM 1.5 sunlight illumination was produced by Luzchem LZC-SSL solar simulator with the filtered Xe-lamp.

3. Results and discussions

SEM and AFM measurements were performed to investigate the surface properties of the deposited films to ensure that the newly prepared electrodes can be used for organic film deposition. Roughness of the films was determined by AFM. Root mean roughness (RMS) values were 5.9 and 2.7 nm for AZO 1 and 2 films, respectively, and 3.3 nm for ITO. AFM images of the films can be found in Appendix A. Previous studies have shown that the roughness of the ZnO films depends markedly on the film thickness [27,28]. The RMS value of the AZO film doubled when the film thickness increases from 90 to 170 nm.

Figs. 1 and 2 shows SEM micrographs of the AZO films. Figures with lower magnification can be found in Appendix A. As Figs. 1 and 2 illustrate, the films are uniform and have been grown as wedge-shape crystallites. The morphology of the surface is characteristic for ALD grown ZnO films and it is in agreement with previously published studies [8,25,29]. The size of the crystallites is approximately 80–100 nm for AZO 1 and 60–80 nm for AZO 2 electrode types. The smaller crystallites in AZO 2 can be attributed to the higher deposition temperature when the film thickness is almost two times lower compared to deposition at lower temperature. Unlike one could expect, the resistivity of the film is independent of the film thickness. Although AZO 2 film is thinner than AZO 1, the sheet resistance of both films is approximately 500 Ω/□. The decreased resistivity with increased deposition temperature may be related to different crystalline growth directions at different temperatures. At 150 °C the [1 0 0] direction is observed to be dominant whereas at 250 °C the [0 0 2] direction dominates the crystalline growth. In order to decrease the resistivity of the AZO films to the same level as the ITO film the thickness of the AZO film should be increased up to 1 μm, which would decrease the transparency of the layer gradually [25]. Also by optimizing the doping procedure the resistivity of the AZO films can be decreased [30,31]. In spite of

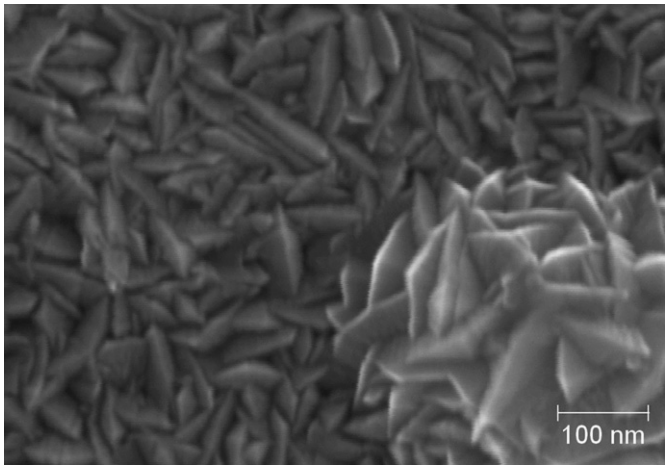

Fig. 1. SEM image of aluminum doped zinc oxide deposited at 150 °C (AZO 1).

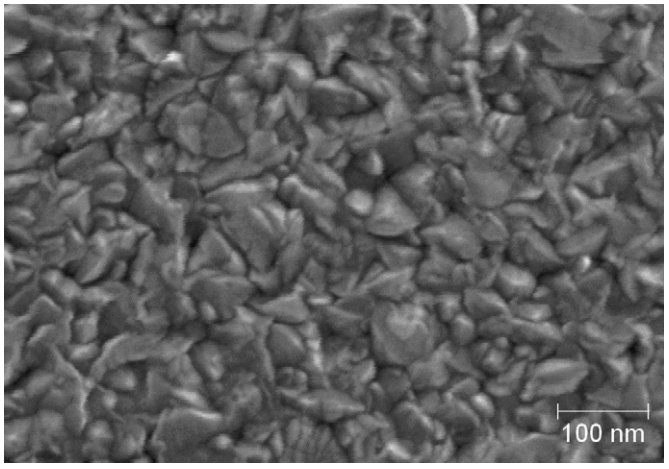

Fig. 2. SEM image of aluminum doped zinc oxide deposited at 250 °C (AZO 2).

the relatively high resistivity of the AZO this is not the factor limiting the device performance because the photocurrent generated at PHT-PTCDI junction was $<20\,\mu A$ under experimental conditions used. Thus, the voltage drop (<0.01 V) caused by the AZO electrode can be neglected.

Absorption spectra of two films (without top electrodes) are shown in Fig. 3. The absorption of the organic layers is clearly seen in the range 450–600 nm. Due to the transparency differences between the ITO and AZO electrodes a small difference in absorption spectra is observed. The order of the active layers does not affect the sample absorption.

Current–voltage characteristics of the devices were measured in order to investigate possibilities to use AZO electrodes in photovoltaic applications. The electrode next to electron donor (PHT) is an anode and electrode next to electron acceptor (PTCDI), a cathode. Thus, in devices 1 and 2 the expected photoelectron flow is from Au toward AZO and in devices 3 and 4 from ITO or AZO toward Au. Each sample had at least five electrode pairs and couple of similar devices was prepared. Because of the defects on the structure (e.g. dust particles shown in Fig. 1) few of the electrodes were short-circuited. The photovoltaic parameters of the devices are summarized in Table 2 and the *I–V* characteristics of the devices 1 and 3 are presented in Fig. 4. In Table 2 the letters "a" and "b" indicates different contacts in the same device.

By comparing the results recorded immediately after the removing of the samples from the vacuum it was observed that the photovoltaic performance of the devices 1 and 2 is very

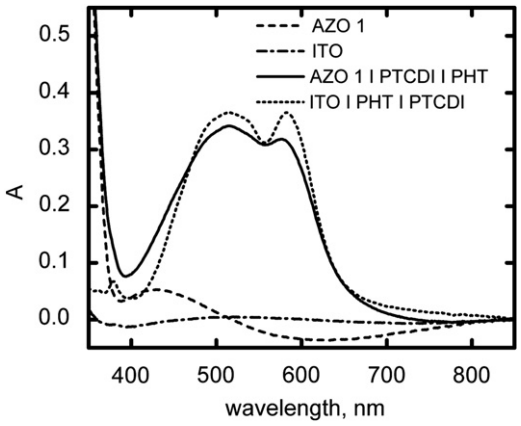

Fig. 3. Absorption spectra of the devices 1 (AZO 1 | PTCDI | PHT) and device 3 (ITO | PHT | PTCDI), and of the electrodes before deposition of organic layers (sample codes AZO 1 and ITO).

Table 2
Effect of time on short-circuit current (I_{SC}), open-circuit voltage (U_{OC}), fill factor (*FF*) and power conversion efficiency (η) of the measured devices. In the device names "1a" and "1b", "a" refers to electrode a and "b" to electrode b.

Device	Measurement	I_{SC} (mA/cm^2)	U_{OC} (V)	*FF*	η (%)
1a	Immediately	2.13	0.37	0.50	0.36
1a	After 18 days	2.08	0.40	0.52	0.41
1b	Immediately	2.24	0.36	0.45	0.39
1b	After 40 days	1.97	0.39	0.54	0.43
2	Immediately	1.95	0.39	0.49	0.38
2	After 8 days	1.88	0.42	0.53	0.42
3	Immediately	1.58	0.37	0.50	0.29
3	After 1 day	1.54	0.34	0.37	0.20

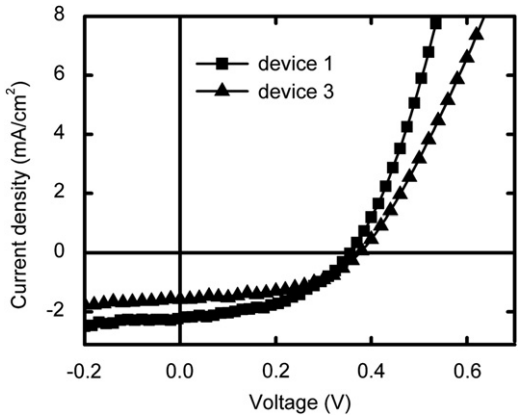

Fig. 4. Current–voltage characteristics of the device 1 (square) and 3 (triangle) under 1000 W/m^2 simulated AM 1.5 solar illumination.

similar to that of the reference device 3. The order of the organic layers and photocurrent generation direction is switched to opposite (the gold is cathode in case of device 3 and anode in devices 1 and 2). Device 4, which is structurally identical to the reference device 3, had significantly lower efficiency compared to other devices and therefore the results are not presented here. The reasons for the weak performance of AZO as a hole collecting electrode is not clear. It may be related to a poor performance of the AZO–PHT interface, either the adhesion of PHT to AZO is weak or the spin coated PHT layer is too thin to form uniform film. From the theoretical point of view, devices 1 and 2 may have better performance than device 4 since the HOMO and LUMO levels of

the PHT and PTCDI layers have better matching to the corresponding work functions of the electrodes when AZO is as the electron collecting electrode and Au is as the hole collecting electrode [8,32,33]. Additionally the work function of AZO could be adjusted by ozone treatment [12].

A few minor differences between devices utilizing the ITO and AZO electrodes can be noted from Table 2 and Fig. 4. The most essential is a higher short-circuit current of the AZO-based devices. A small variation in the performance is observed between device 1 and device 2 and between different electrodes in device 1, but the deviations are not significant. The results suggest that both of the AZO films work as well as the ITO film in organic photovoltaic devices despite the difference in deposition conditions of the AZO electrodes and apparent difference in the crystalline structures. Also deposition of aluminum oxide in the last cycle of ALD process (device 1) had no detectable effect. Taking into account the ambient measurement conditions and non-optimized active layers the obtained power conversion efficiencies are in the expected level [23,26].

In general, relatively poor stability of the organic solar cell is one of its major drawbacks and numbers of studies have shown that degradation of the cells is a complex process, which is not yet fully understood [34]. In previous studies doped ZnO was used as the anode together with the Al cathode and devices were operated in inert atmosphere to prevent fast oxidation of Al [2,8,10]. To allow device operation in open air the Au top electrodes were used in this study. Au has a higher work function than Al and is considered to be a less favorable electrode material [3,23,26]. For the purpose of degradation testing the samples were stored in open air in dark at room temperature and the *I–V* measurements were repeated after certain period of time. The results are given in Table 2.

There was no remarkable drop in short-circuit current (I_{SC}) for device 1 after 18 days of storing. When the measurement was performed after 40 days from the sample preparation, I_{SC} has decreased about 15% but due to small increase in open-circuit voltage the power conversion efficiency is even increased. Similar time trend was observed for device 2, indicating that both types of the AZO electrodes have a positive effect on photovoltaic device durability. The biggest difference is found by comparing the AZO and ITO devices. Initially, I_{SC} is somewhat lower for ITO and decreases remarkably in one day. The shape of the *IV*-curve is also changed as it can be seen from Fig. 5, resulting in decreased power conversion efficiency.

The ITO–PHT interface and the ITO electrode itself may be responsible for the fast degradation of the ITO device. Two degradation phenomena have been observed previously. One is an exchanging reaction between oxygen in the outer monolayer of ITO and diffused oxygen and the other is the diffusion of indium through the entire device to the counter electrode [35]. Stability and efficiency of the ITO based devices has been improved by inserting a buffer layer between ITO and active layers [9,11], which is not required in the case of AZO electrode.

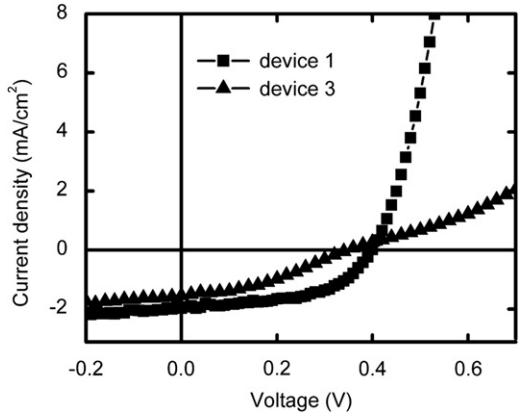

Fig. 5. Current–voltage characteristics of device 1 (square) measured 40 days after device fabrication and device 3 (triangle) measured one day after the device fabrication.

4. Conclusions

In summary, the AZO thin films have been studied as an alternative transparent electrode material to ITO for organic photovoltaic applications, using known donor (PHT) and acceptor (PTCDI) layers as device testing platform. AZO films were deposited successfully at 150 and 250 °C using an ALD technique resulting in 170 and 90 nm thick films, respectively. Films were grown uniformly with reasonably low surface roughness. Both the AZO films showed performance comparable to that of the reference device where ITO was used as TCO electrode. It is important to emphasize that the aim of this study was to find alternative TCO for ITO and deposition method, which offers the possibility to use low temperatures. Better power conversion can be obtained by optimizing the active layers. The biggest advantage of the AZO electrodes compared to the ITO electrode containing reference device was the stability—no sample degradation was observed in ambient conditions during 40 days.

The presented results demonstrate that ALD is a promising method for the deposition of AZO thin films at relatively low temperatures and can be used as replacement for the ITO electrode.

Acknowledgments

This work was supported by the Finnish Funding Agency for Technology and Innovation (TEKES), Project "PELOTON". The authors are very grateful to Deep Sea Engineering Oy for ALD depositions.

Appendix A. Supplementary material

Supplementary data associated with this article can be found in the online version at doi:10.1016/j.solmat.2010.04.006.

References

[1] F.O. Adurodija, Lasers in thin film processing, in: H.S. Nalwa (Ed.), Handbook of Thin Film Materials, Academic Press, San Diego, 2002, p. 162.
[2] D. Xu, Z. Deng, Y. Xu, J. Xiao, C. Liang, Z. Pei, C. Sun, An anode with aluminum doped on zinc oxide thin films for organic light emitting devices, Phys. Lett. A 346 (2005) 148–152.
[3] J. Owen, M.S. Son, K.-H. Yoo, B.D. Ahn, S.Y. Lee, Organic photovoltaic devices with Ga-doped ZnO electrode, Appl. Phys. Lett. 90 (2007) 033512.
[4] A. Tanaka, M. Hirata, Y. Kiyohara, M. Nakano, K. Omae, M. Shiratani, K. Koga, Review of pulmonary toxicity of indium compounds to animals and humans, Thin Solid Films 518 (2009) 2934–2936.
[5] M. Strange, D. Plackett, M. Kaasgaard, F.C. Krebs, Biodegradable polymer solar cells, Sol. Energy Mater. Sol. Cells 92 (2008) 805–813.
[6] K. Ellmer, A. Klein, ZnO and its applications, in: K. Ellmer, A. Klein, B. Rech (Eds.), Transparent Conductive Zinc Oxide Basics and Applications in Thin Film Solar Cells, Spinger-Verlag, Berlin, Heidelberg, 2008, pp. 1–34.
[7] K. Ellmer, Electrical properties, in: K. Ellmer, A. Klein, B. Rech (Eds.), Transparent Conductive Zinc Oxide Basics and Applications in Thin Film Solar Cells, Spinger-Verlag, Berlin, Heidelberg, 2008, pp. 1–34.
[8] S.-H.K. Park, J.-I. Lee, C.-S. Hwang, H.Y. Chu, Characteristics of organic light emitting diodes with Al-doped ZnO anode deposited by atomic layer deposition, Jpn. J. Appl. Phys. 44 (2005) L242–L245.
[9] M.S. White, D.C. Olson, S.E. Shaheen, N. Kopidakis, D.S. Ginley, Inverted bulk-heterojunction organic photovoltaic device using a solution-derived ZnO underlayer, Appl. Phys. Lett. 89 (2006) 143517-1–143517-3.

[10] K. Schulze, B. Maenning, K. Leo, Y. Tomita, C. May, J. Hüpkes, E. Brier, E. Reinold, P. Bäuerle, Organic solar cells on indium tin oxide and aluminum doped zinc oxide anodes, Appl. Phys. Lett. 91 (2007) 073521-1–073521-3.
[11] S. Park, S.J. Tark, J.S. Lee, H. Lim, D. Kim, Effects of intrinsic ZnO buffer layer based on P3HT/PCBM organic solar cells with Al doped ZnO electrode, Sol. Energy Mater. Sol. Cells 93 (2009) 1020–1023.
[12] G.B. Murdoch, S. Hinds, E.H. Sargent, S.W. Tsang, L. Mordoukhovski, Z.H. Lu, Aluminum doped zinc oxide for organic photovoltaics, Appl. Phys. Lett. 94 (2009) 213301-1–213301-3.
[13] S. Fernández, F.B. Naranjo, Optimization of aluminum-doped zinc oxide films deposited at low temperature by radio-frequency sputtering on flexible substrates for solar cell applications, Sol. Energy Mater. Sol. Cells 94 (2010) 157–163.
[14] V. Bhosle, J.T. Prater, F. Yang, D. Burk, S.R. Forrest, J. Narayan, Gallium-doped zinc oxide films as transparent electrodes for organic solar cell applications, J. Appl. Phys. 102 (2002) 023501-1–023501-5.
[15] S. Faÿ, U. Kroll, C. Bucher, E. Vallat-Sauvain, A. Shah, Low pressure chemical vapour deposition of ZnO layers for thin film solar cells: temperature-induced morphological changes, Sol. Energy Mater. Sol. Cells 86 (2005) 385–397.
[16] F.C. Krebs, M. Jørgensen, K. Norrmann, O. Hagemann, J. Alstrup, T.D. Nielsen, J. Fyenbo, K. Larsen, J. Kristensen, A complete process for production of flexible large area polymer solar cells entirely using screen printing—first public demonstration, Sol. Energy Mater. Sol. Cells 93 (2009) 422–441.
[17] F.C. Krebs, Polymer solar cell modules prepared using roll-to-roll methods: knife-over-edge coating, slot die coating and screen printing, Sol. Energy Mater. Sol. Cells 93 (2009) 465–475.
[18] M. Ritala, M. Leskelä, Atomic layer deposition, in: H.S. Nalwa (Ed.), Handbook of Thin Film Materials, Academic Press, San Diego, 2002, pp. 103–159.
[19] T. Suntola, J. Antson, US Patent 4058430 (1977).
[20] M. Leskelä, M. Ritala, Atomic layer deposition (ALD): from precursors to thin films structures, Thin Solid Films 498 (2002) 138–146.
[21] R.L. Puurunen, Surface chemistry of atomic layer deposition: a case study for trimethylaluminum/water process, J. Appl. Phys. 97 (2005) 121301-1–121301-52.
[22] L. Niinistö, J. Päiväsaari, J. Niinistö, M. Putkonen, M. Nieminen, Advanced electronic and optoelectronic materials by ALD: an overview with special emphasis on recent progress in processing of high-*k* dielectrics and other oxide materials, Phys. Status Solidi A 201 (2004) 1443–1452.
[23] P. Vivo, M. Ojala, V. Chukharev, A. Efimov, H. Lemmetyinen, Role of a phthalocyanine–fullerene dyad in multilayered organic solar cells, J. Photochem. Photobiol. A 203 (2009) 125–130.
[24] M. Ritala, T. Asikainen, M. Leskelä, J. Skarp, ALE growth of transparent conductors, Mater. Res. Soc. Symp. Proc. 426 (1996) 513–518.
[25] V. Lujala, J. Skarp, M. Tammenmaa, T. Suntola, Atomic layer epitaxy growth of doped zinc oxide films from organometals, Appl. Surf. Sci. 82–83 (1994) 34–40.
[26] P. Vivo, J. Jukola, M. Ojala, V. Chukharev, H. Lemmetyinen, Influence of Alq3/Au cathode on stability and efficiency of a layered organic solar cell in air, Sol. Energy Mater. Sol. Cells 92 (2008) 1416–1420.
[27] I.A. Kowalik, E. Guziewich, K. Kopalko, S. Yatsunenko, A. Wójcik-Glodowska, M. Godlewski, P. Dłuzewski, E. Łusakowska, W. Paszkowicz, Structural and optical properties of low-temperature ZnO films grown by atomic layer deposition with diethylzinc and water precursors, J. Cryst. Growth 311 (2009) 1096–1101.
[28] J.W. Elam, Z.A. Sechrist, S.M. George, ZnO/Al_2O_3 nanolaminates fabricated by atomic layer deposition: growth and surface roughness measurements, Thin Solid Films 414 (2002) 43–55.
[29] J. Lim, C. Lee, Effects of substrate temperature on the microstructure and photoluminescence properties of ZnO thin films prepared by atomic layer deposition, Thin Solid Films 515 (2007) 3335–3338.
[30] J.-S. Na, Q. Peng, G. Scarel, G.N. Parsons, Role of gas doping sequence in surface reactions and dopant incorporation during atomic layer deposition of Al-doped ZnO, Chem. Mater. 21 (2009) 5585–5593.
[31] J.-S. Na, G. Scarel, G.N. Parsons, In situ analysis of dopant incorporation, activation, and film growth during thin film ZnO and ZnO:Al atomic layer deposition, J. Phys. Chem. C 114 (2010) 383–388.
[32] J.-J. Yun, H.-S. Jung, S.-H. Kim, E.-M. Han, Chlorophyll-layer-inserted poly(3-hexyl-thiophene) solar cell having a high light-to-current conversion efficiency up to 1.48%, Appl. Phys. Lett. 87 (2005) 123102.
[33] V. Chiș, G. Mile, R. Știufiuc, N. Leopold, M. Oltean, Vibrational and electronic structure of PTCDI and melamine–PTCDI complexes, J. Mol. Struct. 924–926 (2009) 47–53.
[34] M. Jørgensen, K. Norrman, F.C. Krebs, Stability/degradation of polymer solar cells, Sol. Energy Mater. Sol. Cells 91 (2008) 686–714.
[35] F.C. Krebs, K. Norrman, Analysis of the failure mechanism for a stable organic photovoltaic during 10,000 h of testing, Prog. Photovoltaics: Res. Appl. 15 (2007) 697–712.

Supplementary material

Aluminum doped zinc oxide films grown by atomic layer deposition for organic photovoltaic devices

Hanna Saarenpää, Tapio Niemi, Antti Tukiainen, Helge Lemmetyinen, Nikolai Tkachenko

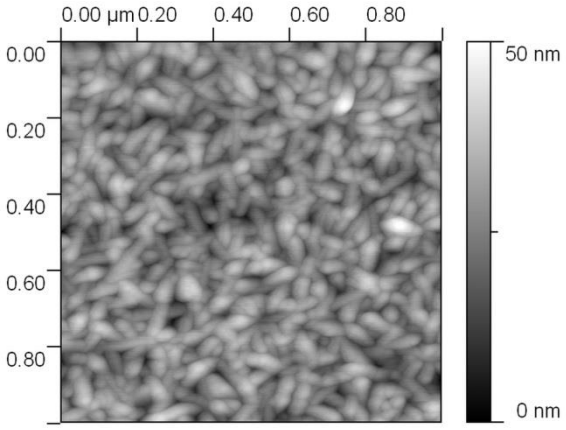

Figure S1. AFM image of AZO 1 film.

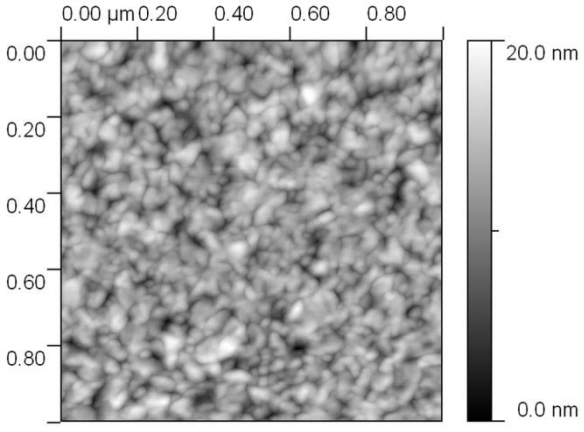

Figure S2. AFM image of AZO 2 film.

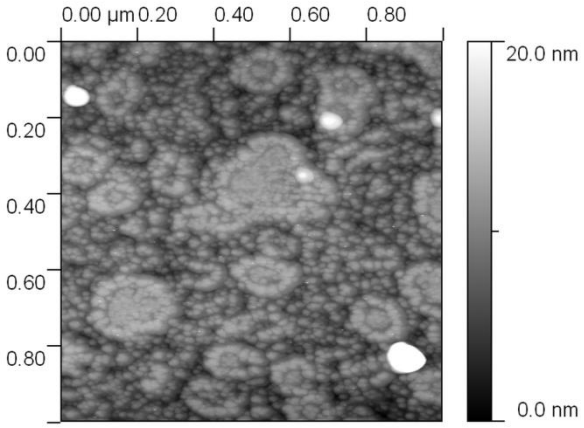

Figure S3. AFM image of ITO film.

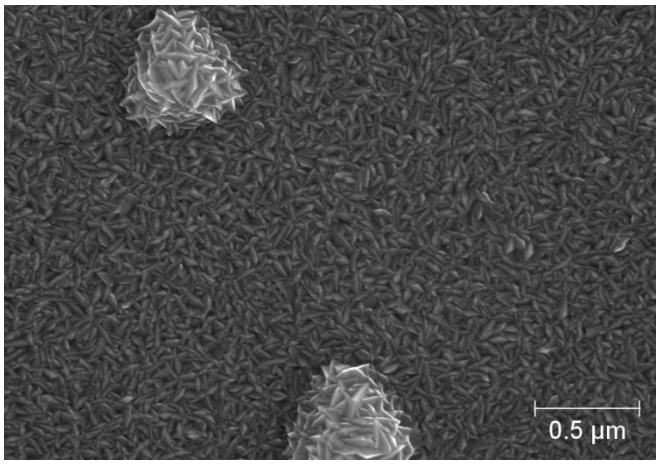

Figure S4. SEM micrograph of aluminum doped zinc oxide deposited at 150 °C (AZO 1).

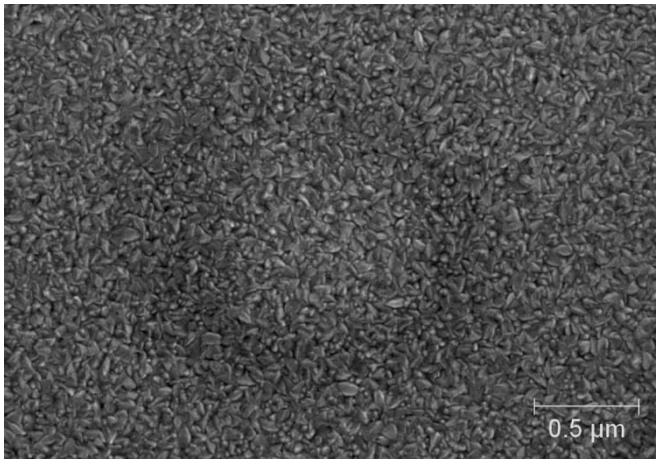

Figure S5. SEM micrograph of aluminum doped zinc oxide deposited at 250 °C (AZO 2).

II

SELF-ASSEMBLED PORPHYRINS ON MODIFIED ZINC OXIDE NANORODS: DEVELOPMENT OF MODEL SYSTEMS FOR IN-ORGANIC-ORGANIC SEMICONDUCTOR INTERFACE STUDIES

by

Hanna Saarenpää, Essi Sariola-Leikas, Alexander Pyymaki Perros, Juha M. Kontio, Alexander Efimov, Hironobu Hayashi, Harri Lipsanen, Hiroshi Imahori, Helge Lemmetyinen and Nikolai V. Tkachenko, 2012

The Journal of Physical Chemistry C vol.116, 2336-2343

THE JOURNAL OF PHYSICAL CHEMISTRY C

Article

pubs.acs.org/JPCC

Self-Assembled Porphyrins on Modified Zinc Oxide Nanorods: Development of Model Systems for Inorganic–Organic Semiconductor Interface Studies

Hanna Saarenpää,*[,†] Essi Sariola-Leikas,[†] Alexander Pyymaki Perros,[§] Juha M. Kontio,[‡] Alexander Efimov,[†] Hironobu Hayashi,[∥] Harri Lipsanen,[§] Hiroshi Imahori,[∥,⊥] Helge Lemmetyinen,[†] and Nikolai V. Tkachenko[†]

[†]Department of Chemistry and Bioengineering and [‡]Optoelectronics Research Centre, Tampere University of Technology, FI-33101 Tampere, Finland

[§]Department of Micro- and Nanosciences, Aalto University, P.O. Box 13500, FI-00076 Aalto, Finland

[∥]Department of Molecular Engineering, Graduate School of Engineering and [⊥]Institute for Integrated Cell-Material Sciences (iCeMS), Kyoto University, Nishikyo-ku, Kyoto 615-8510, Japan

Supporting Information

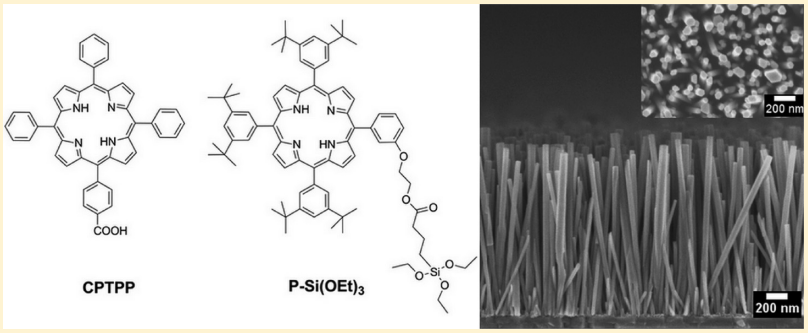

ABSTRACT: Dense arrays of zinc oxide nanorods with high specific surface areas were grown by hydrothermal method and functionalized by self-assembled monolayer (SAM) of porphyrins. The growth process was optimized to obtain dense arrays of nanorods with diameter of 60–80 nm and length up to 1.5 μm. The increase in the effective surface area was monitored by comparing the absorbances of SAM deposited both on the flat and nanorod surfaces of ZnO. To alter further semiconductor-organic SAM interactions, a 2 or 5 nm thick layer of either Al_2O_3 or TiO_2 was deposited on the ZnO nanorods. The present results show that both carboxylic acid and triethoxysilane anchors can be used to form porphyrin SAMs on the studied metal oxide substrates, and the electronic interactions between the metal oxide and porphyrin SAM are strongly modified by a thin layer of Al_2O_3 or TiO_2. These hybrid semiconductor-organic SAM constructions present promising model systems for advanced spectroscopy studies of semiconductor-organic interfaces with high degree of control over electronic interactions and system morphology.

INTRODUCTION

Photoinduced electron-transfer properties at an organic–inorganic semiconductor interface play an important role in many systems such as photovoltaic and sensor devices.[1] In real devices, the interface structure is a complex one, and several reactions take place simultaneously; therefore, effects of individual reactions are difficult to distinguish.[2] To study any specific reaction in details, we need simple model systems consisting of metal oxide substrate and organic dye molecule attached on it. Moreover, the semiconductor-organic interfacial electronic interactions are extremely fast taking place in picosecond and subpicosecond time domains. To resolve them, advanced time-resolved optical spectroscopy methods must be used, which, in turn, requires systems with relatively high absorptions. This kind of model systems can be constructed by depositing organic layer on nanostructured semiconductor layers with high specific surface area such as arrays of nanorods grown on flat substrates.[3]

Zinc oxide (ZnO) is well known for its versatile ability to form several types of nanostructures with controlled morphology. Great attention has been paid to synthesis techniques of ZnO nanorods (ZnOr) and in particular to hydrothermal growth, which is a convenient method due to its simplicity and low costs. Although ZnO nanorods have smaller surface area than ZnO nanoparticles at the same nanostructure thickness, the ZnO nanorods have advantages of well-controlled surface

Received: November 1, 2011
Revised: December 20, 2011
Published: December 29, 2011

   dx.doi.org/10.1021/jp2104769 | J. Phys. Chem. C 2012, 116, 2336–2343

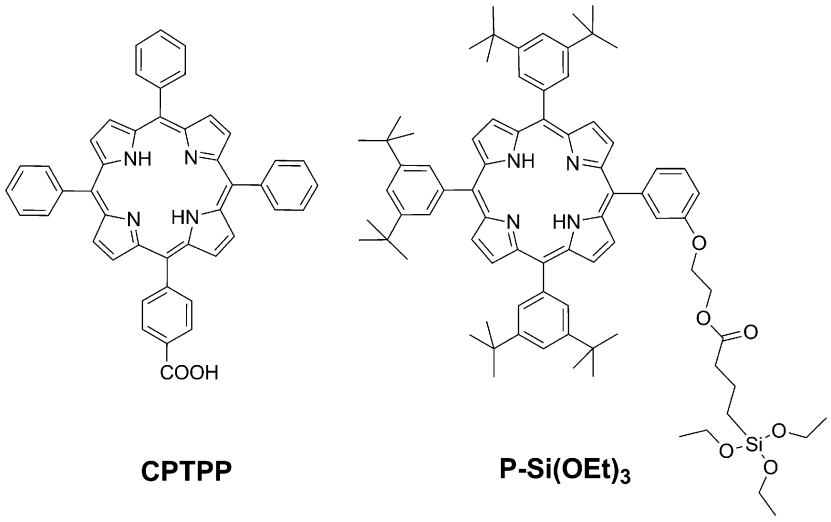

Figure 1. Molecular structures of the studied CPTPP and P-Si$(OEt)_3$ porphyrins.

morphology and 1-D crystallinity, which both are important properties in optoelectronic applications.[4]

Well-defined semiconductor-organic interfaces can be constructed by forming self-assembled monolayers (SAMs) of organic compounds on metal oxides.[5] The self-assembly method has been in active development during past decades. It can be used to form uniform layers of different classes of organic and bio-organic compounds on variety of metal and metal oxide surfaces, including ZnO.[6] Among the dye molecules used for the organic−inorganic semiconductor interface, porphyrins are one of the most attractive molecules because of their high absorption in the visible part of the spectrum, excellent electron-donating properties, and well-developed synthetic routes.[7] Several types of model porphyrins have been synthesized, and the effect of distance and orientation on the photophysical and electrochemical properties at the organic dye-semiconductor interface has been intensively studied.[8] Studies have been focused on the synthesis of porphyrins with different substituents and anchoring units, whereas less effort has been paid to constructing the model hybrid inorganic semiconductor-organic interfaces.

The electronic properties of the supporting semiconductor substrate, ZnOr in this report, can be altered by depositing a thin layer of other metal oxide on it by atomic layer deposition (ALD) method. Conformal coatings can be deposited by ALD also for nonflat substrates.[9] An important advantage of ALD method is that morphology of the substrate remains essentially the same, whereas the band gap and positions of valence and conduction bands can be tuned in a rather wide range. This allows the comparison of the electronic interaction between different metal oxides and organic SAM under otherwise the same conditions.

In the first part of this work, a hydrothermal growth of vertically oriented ZnOr was optimized to prepare semiconductor substrates with a high specific surface area. Several studies have been done to understand factors affecting the properties of the ZnOr grown by hydrothermal method,[4] although the growth conditions have to be optimized for each application separately because small changes in reaction conditions may affect significantly the ZnOr morphology.[4d] Second, SAMs of free-base porphyrins with carboxylic acid or triethoxysilane anchor groups were formed on the metal oxide substrates. The carboxyl acid group is widely used as an anchor in immobilization of dye molecules on metal oxide surfaces,[7,8] whereas the triethoxysilane anchor is less common because of synthetic and stability reasons.[10] However, triethoxysilane is an excellent alternative because it has been observed to have strong binding properties to TiO_2, thus improving the durability of photovoltaic devices,[10a] and it can be used to form SAMs on many other oxides.[10b] In the third part of the study, the ZnOr surface was modified by a thin layer of Al_2O_3 or TiO_2 deposited by ALD method. The present results show that both the carboxylic acid and triethoxysilane anchor groups can attach porphyrins to all studied metal oxide substrates. In addition, preliminary photophysical studies of the SAMs show that the electronic interactions between the metal oxide and porphyrin SAM can be strongly modified by a thin layer of Al_2O_3 or TiO_2.

EXPERIMENTAL SECTION

Hydrothermal Growth of ZnO Nanorods. ZnO nanorods were fabricated by a two-step hydrothermal method: formation of seed layers on flat substrates and the actual growth of the nanorods.[11] The chemicals and solvents utilized in this study were purchased from Sigma Aldrich and used without purification. ITO coated glass substrates were cleaned by the method previously described.[12] Two types of seed layers, denoted as layers A and B, were prepared by spin coating. To prepare seed layer A, 0.01 M zinc acetate ($C_4H_6O_4Zn{\cdot}2H_2O$, ≥98%) in ethanol was spin-coated on N_2 plasma-treated (10 min) ITO surface (1500 rpm, 60 s), followed by annealing in air at 350 °C for 20 min. Spin coating and annealing were repeated three times. Seed layer B was formed by using 0.23 M zinc acetate dissolved in a mixture of 2-methoxyethanol ($CH_3OCH_2CH_2OH$) and ethanolamine ($NH_2CH_2CH_2OH$) 96:4. Solution was stirred at 60 °C for 2 h and cooled to room temperature. Spin coating and annealing were performed in the same manner as that for seed A, but only one layer of zinc acetate was spin-coated on ITO. Precursor solutions for growth of ZnOr were prepared in ion-exchanged Milli-Q-water by mixing zinc nitrate ($Zn(NO_3)_2$, ≥99%) and hexamethylenetetramine ($C_6H_{12}N$, 99%), keeping their volume ratio 1:1. The concentration was either 0.02 or 0.05 M. The growth at 80, 85, or 90 °C was carried out in a sealed beaker by immersing the substrates upside down in the precursor solutions for 2−10 h.

dx.doi.org/10.1021/jp2104769 | J. Phys. Chem. C 2012, 116, 2336−2343

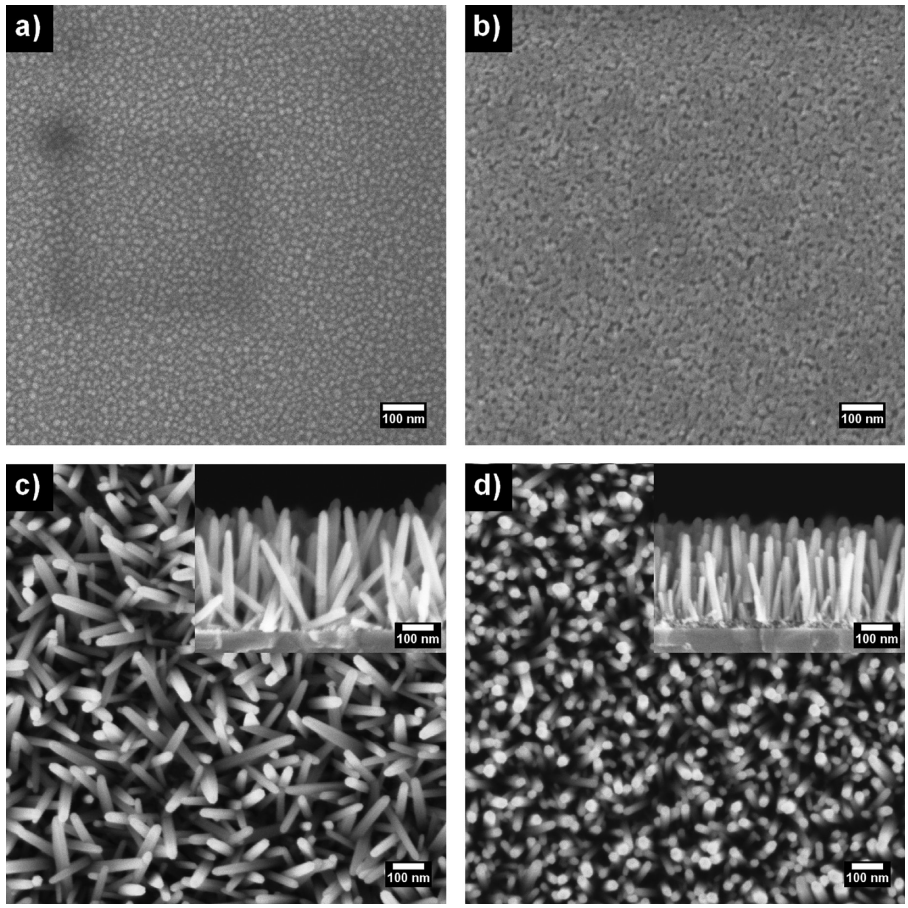

Figure 2. SEM images of (a) seed layer A, (b) seed layer B, (c) ZnOr grown at 80 °C for 4 h on the seed A (diameter 40 nm, average length 350 nm), and (d) ZnOr on the seed layer B (diameter 35 nm, average length 250 nm).

After the reaction, the samples were removed from the solution, rinsed with Milli-Q water, and dried in air.

Modification of the Nanorods. ZnO nanorods grown by using the seed layer B, 0.02 M precursors, the growth temperature of 85 °C, and growth time of 10 h (changing precursor solution after 5 h), were used for surface modification study. The nanorods were ∼1.5 μm in length and 60−80 nm in diameter. The ZnOr surfaces were modified by depositing either 2 or 5 nm thick layer of TiO_2, Al_2O_3, or ZnO by atomic layer deposition (ALD) using Beneq TFS-500 reactor. The growth temperature for all films was 200 °C. TiO_2 was deposited using titanium tetrachloride and water, Al_2O_3 using trimethylaluminum and water, and ZnO using diethylzinc and water, respectively. The flow rate for all precursors was 200 sccm (standard cubic centimeters per minute). The average growth rates are expected to be 0.7 to 0.9, 1.1, and 2 Å per cycle for TiO_2,[13] Al_2O_3,[14] and ZnO,[14a] respectively. The modified ZnOr substrates are denoted as ZnOr|ZnO, ZnOr|Al_2O_3, and ZnOr|TiO_2 in the Results and Discussion.

Self-Assembled Monolayers of Porphyrins on Nanorod Surfaces. Studied porphyrin chromophores are shown in Figure 1. The synthesis of the 2-{3-[10,15,20-tris(3,5-ditert-butylphenyl)porphyrin-5-yl]phenoxy}ethyl 4-(triethoxysilyl)-butanoate (P-Si$(OEt)_3$) and the procedure of one-step self-assembling is published elsewhere.[10b] Porphyrin (2 mg) was dissolved in toluene (20 mL), and isopropylamine (0.4 mL) was added. Solution was injected in the reaction vessel under argon flow. After 2 h of reaction at 105 °C, samples were removed from reaction vessel and washed by sonicating twice in toluene and once in dichloromethane for 15 s. To form 5-(4-carboxyphenyl)-10,15,20-triphenyl-21,23*H*-porphyrin (CPTPP, 98%, purchased from Porphyrin Systems) SAM on ZnO, TiO_2, and Al_2O_3 surfaces, ∼0.0002 M solution of CPTPP in ethanol was prepared. Substrates were heated to 150 °C for 30 min and cooled to 80 °C before immersion into solution for 1 h. After reaction, the samples were rinsed and immersed in ethanol to remove residual porphyrin molecules.[8a]

Characterization. The morphology and the size distribution of the ZnO nanorods were studied using field-emission scanning electron microscope (FE-SEM, Carl Zeiss Ultra 55). Absorption spectra of the samples were measured by Shimadzu UV-360 spectrophotometer. Fluorescence spectra were recorded with a Fluorolog 3 fluorimeter using the correction function supplied by the manufacturer. A time-correlated single-photon counting (TCSPC) system (PicoQuant) consisting of a PicoHarp controller and PDL-800-B driver was used for time-resolved fluorescence measurements. The samples were excited by the pulsed LED (LDH-P-C-405B) at 405 nm. Fluorescence decays were monitored at 660 and 650 nm for CPTPP and P-Si$(OEt)_3$ samples, respectively. Time resolution of the TCSPC measurements was approximately 60−70 ps (fwhm).

RESULTS AND DISCUSSION

Optimization of the Hydrothermal Growth of ZnO Nanorods. The effect of the ZnO seed layer, precursor

dx.doi.org/10.1021/jp2104769 | *J. Phys. Chem. C* 2012, 116, 2336−2343

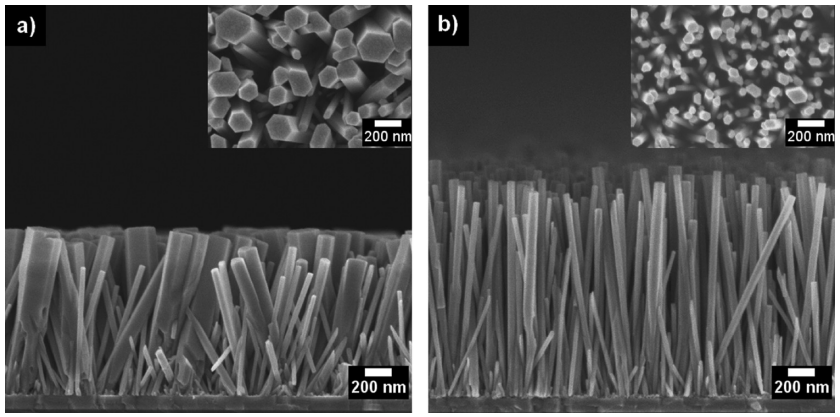

Figure 3. SEM images ZnOr grown at 85 °C for 10 h using (a) seed layer A (diameter 40−250 nm, length 1200 nm) and (b) seed layer B (right, diameter 50−100 nm, length 1500 nm). The concentration of precursors was 0.02 M.

concentration, growth temperature, and the growth time on the ZnOr morphology was studied.

Two types of seed layers, denoted as layers A and B, were prepared by spin coating. The essential difference in preparation process of seed layers A and B was the precursor concentration (higher for B) and number of spin-coated layers. (See the Experimental Section for details.) SEM images of the layers A and B are shown in Figure 2a,b, which demonstrate clearly the difference between them. Seed layer A consists of particles with 10−20 nm diameters, and according to the SEM image (not shown), thickness of the layer is ∼10 nm. Seed B is ∼25 nm thick and has a porous morphology. Small pores in the film (diameter <10 nm) are most probably due to the decomposition of zinc copolymers during the annealing.[15]

As previously described, the seed layer acts as a nuclei and thus directly affects the growth of ZnOr.[4a,b,e] Figure 2c,d show nanorods grown on seed layers A and B while keeping reaction conditions otherwise the same. The seed layer has strongest effect on the ZnOr density and orientation. The alignment of ZnOr grown on the seed layer B is almost perpendicular to the substrate surface, and the density is higher compared with A. The effective surface area of ZnOr is increased with the density, which is confirmed by the increased absorption of the porphyrin SAM on the surface, as will be later discussed. In contrast with previous studies,[4b] the seed layer has only a minor effect on the average diameter of the ZnOr, which is mainly determined by the precursor concentration.

One interesting and not so much reported finding is that the seed layer has an effect on the diameter distribution of the ZnOr.[4d] As illustrated in Figure 3, thin nanorods (d = 40 nm) grown on seed A were fused together resulting in nanorods with diameter of ∼200 nm. This is due to the poor alignment of the nanorods. The ZnOr growing in a direction deviating from the substrate normal will easily meet other rods and grow together.[4a] Wide diameter distribution is observed only at the growth temperature of 85 °C. Further experiments are needed to find out the reason why individual rods do not fuse together at lower growth temperature (80 °C), but those are beyond the aim of this study.

The precursor concentration has the largest effect on the diameter of ZnOr. Our results are consistent with the previous studies by Vayssieres[4f] and others.[4b,d] The diameter of ZnOr increases with the precursor concentration, no matter which seed layer is used (Supporting Information Figures S1 and S2). In principle, larger diameter should result in an increase in the effective surface area if the density of nanorods remains the same. Apparently, this is not the case because nanorods fuse together approximately half of their length (Supporting Information Figure S2a).

Three growth temperatures (80, 85, and 90 °C) were tested to increase the aspect ratio of ZnOr. The growth rate increases with the temperature;[4g] that is, the length of ZnOr increases (Supporting Information Figure S3). At the highest studied temperature (90 °C) also the diameter of ZnOr is slightly increased. Therefore longer (l > 1 μm) ZnOr for interface studies was grown at 85 °C.

Regardless of the seed layer type, almost a linear increase in the length as a function of the growth time can be observed at the growth temperature of 80 °C (Supporting Information Figure S4). The consumption of the precursor ions is faster at higher temperatures (85 °C), and thus the growth rate slows down after 6 h of reaction.

Effective Surface Area of ZnOr Estimated by the Absorbance of SAM. An important property of SAMs is that they can be deposited on high curvature surfaces including porous surfaces if the characteristic size of pores is much greater than the size of molecules. Absorption of a SAM deposited on any nonflat surface is expected to be proportional to the effective surface area if the monolayer formation is completed. In the case of ZnOr, the length of nanorods is the main factor determining the effective surface area, although the diameter and density vary during the growth process and affect the effective area as well. Therefore comparison of absorptions of SAMs deposited on different types of nanorods is a relatively simple but informative way to monitor the morphology of ZnOr.[5d]

To estimate the effective surface area of ZnOr grown in different conditions, CPTPP SAMs were deposited on the ZnOr. Absorption spectra of CPTPP SAMs on one series of ZnOr substrates (l = 300−900 nm) are shown in Figure 4. The scattering of the longer ZnOr is relatively high at the porphyrin Soret band region around 420 nm (Supporting Information, Figure S5). Although the absorption spectra for each ZnOr substrate, measured before the deposition of SAM, were subtracted from the sample spectra, accurate estimation of the SAM absorption is not possible in this wavelength range. The absorption maxima of CPTPP in SAM Soret bands are red-shifted (15 nm) compared with that in ethanol, and the bands are broadened.[8e] Figure 5 shows the dependence of CPTPP SAM absorption at 430 nm on the nanorods length for three

dx.doi.org/10.1021/jp2104769 | J. Phys. Chem. C 2012, 116, 2336−2343

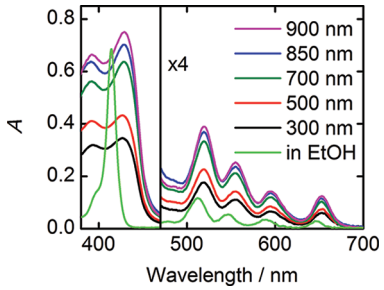

Figure 4. Absorption spectra of CPTPP SAMs on ZnOr substrates grown on seed B at 85 °C with different lengths of nanorods (indicated in the plot) and of CPTPP in ethanol solution.

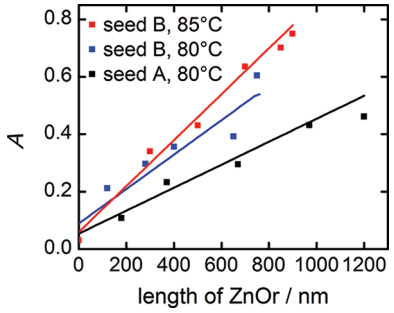

Figure 5. Dependence of absorbances (at 430 nm) of CPTPP SAMs on the ZnO nanorod length grown at 80 °C on seed A (blue) and seed B (black) and those of grown at 85 °C on seed B (red).

different series of the ZnOr substrates. ZnOr grown on seed A (at 80 °C) has a smaller surface area compared with that of the ZnOr grown on seed B (at 80 or 85 °C), as indicated by the lower absorbances of CPTPP SAMs. The main reason for this is the lower density of ZnOr because the diameter is even greater if seed A is used (Figure 2c). The absorption increases almost linearly with the length of ZnOr, although small deviations from the linear dependence can be attributed to a small variation in nanorods deposition conditions leading to some differences in the nanorod lengths. Some of the nanorods grow slower than others or start to grow later, and the relative amount of such nanorods increases with the growth time (Figure 3). The growth temperature of ZnOr has no detectable effect on the surface area; the higher growth temperature increases only the growth rate of ZnOr.

Emission spectra of CPTPP SAMs on ZnOr (l = 300–900 nm) were measured and are presented in Supporting Information (Figure S6). The estimation of the effective surface area in terms of the emission intensity is not as simple as that of the absorption. The number of emitted photons depends nonlinearly on the absorption at high absorbances at the excitation wavelength. In the present study, if ZnOr is shorter than 500 nm (A = 0.4 at 430 nm), the emission intensity of CPTPP SAM increases almost proportionally with the absorption, whereas for longer ZnOr (A > 0.65 at 430 nm), the increase in the emission intensity is somewhat slower than that of the sample absorption.

The dependence of the effective surface area increase on the ZnOr size and density can be estimated quantitatively using a simple geometrical model. If the nanorods are supposed to be packed in square lattice with a period D and have square cross-section with a thickness of d (obviously $D > d$) and length l, then the area of one nanorod wall is $4ld$ and the increase in the effective surface area is

$$r = (4ld + D^2)/D^2 = 1 + (4ld)/D^2 \quad (1)$$

There are always some variations in the diameter and length of ZnOr grown by the hydrothermal method, and only rough estimations of the dimensions can be done based on the SEM figures shown in Figure 6. According to eq 1 after reactions for 2 and 4 h at 85 °C, the expected increases in the effective surface areas of ZnOr are 15 (l = 300 nm, d = 30 nm, D = 50 nm) and 22 (l = 500 nm, d = 40 nm, D = 60 nm) times, respectively.

For the quantitative determination of the absorption increase due to increase in the effective surface area, one needs to measure absorption of the CPTPP SAM formed on a flat surface. Because CPTPP cannot self-assemble on quartz or glass substrates, a 2 nm layer of ZnO was deposited on glass substrate by ALD, and the SAM was formed on it under conditions similar to that on ZnOr (absorption spectrum is presented in Supporting Information Figure S7). It should be kept in mind that the effective surface area of 2 nm ZnO layer on glass can be more than 1 due to the layer roughness. Therefore the absorption is expected to be slightly higher than that on ideal flat surface. At 430 nm, the absorbances of the CPTPP SAMs formed on ZnOr are 0.34 (l = 300 nm) and 0.42 (l = 500 nm), respectively. The absorbance of the monolayer on the flat surface is 0.03. Therefore, the increase in the effective surface area leads to 11- and 14-fold increases in absorption for 300 and 500 nm long nanorods, respectively. For shorter ZnOr (l = 300 nm), the estimation is reasonably accurate, but for the longer (l = 500 nm), the expected value, 22, is apparently higher than the actually measured, 14. Longer ZnOr is partially fused at its roots, which is the most probable reason why the actual surface area is smaller compared with the theoretical one.

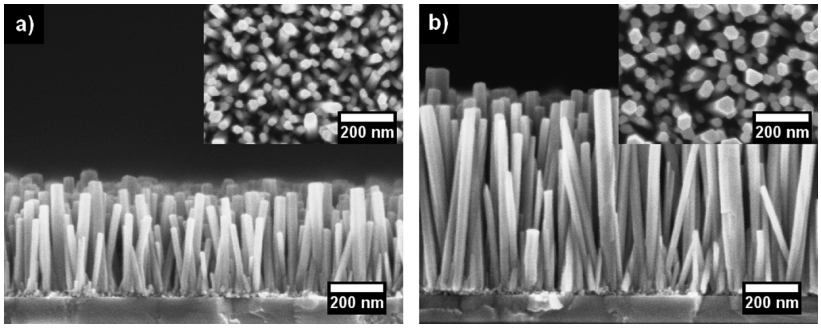

Figure 6. SEM images of ZnOr grown at 85 °C for (a) 2 and (b) 4 h (Seed B, 0.02 M precursors).

dx.doi.org/10.1021/jp2104769 | J. Phys. Chem. C 2012, 116, 2336–2343

Evaluation of Electronic Interactions between TiO_2, Al_2O_3, or ZnO and SAM. Electronic interactions between three metal oxides, TiO_2, Al_2O_3, and ZnO, and porphyrin SAM were studied. The difference between TiO_2 and ZnO is not expected to be large because these semiconductors have rather similar band gaps, but Al_2O_3 is an insulator and may have a large effect on semiconductor−SAM interactions. Two types of porphyrins were used to form SAMs: CPTPP and P-Si$(OEt)_3$. As illustrated in Figure 1, these porphyrins differ from each other: CPTPP has carboxylic acid anchor directly in the *meso*-phenyl ring, whereas P-Si$(OEt)_3$ has a much longer linker with triethoxysilane anchor and bulky *tert*-butyl groups at the meta positions of the *meso*-phenyl substituents. Taking these structural factors into account, one may expect that the two porphyrin SAMs have different degree of aggregation, tilt angles, and distance between chromophores and metal oxide surfaces. As a consequence, differences in the interactions between the porphyrin SAM and the semiconductor are expected.[2a]

Absorption spectra of the CPTPP and P-Si$(OEt)_3$ SAMs on the modified ZnOr substrates are shown in Figure 7. Typical

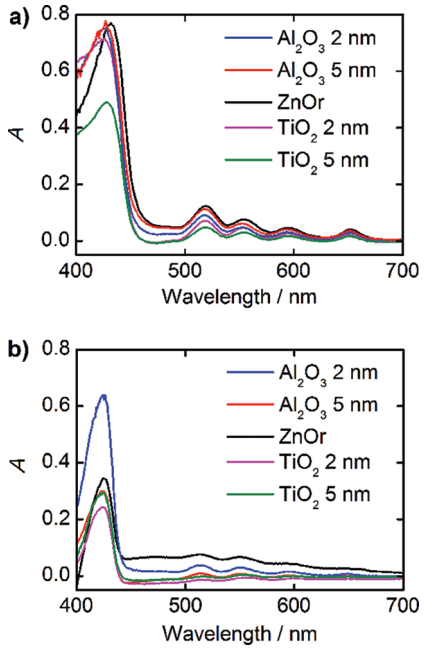

Figure 7. Absorption spectra of CPTPP (a) and P-Si$(OEt)_3$ (b) SAMs on ZnOr, ZnOr|Al_2O_3 (2 or 5 nm) and ZnOr|TiO_2 (2 or 5 nm).

features of the free base porphyrin, Soret band, and four Q bands are observed in all spectra. Small shifts in absorption spectra of CPTPP SAMs on different metal oxide surfaces are attributed to inaccurate subtraction of the substrate spectra (Supporting Information, Figure S8). The absorbances of CPTPP SAMs are roughly 1.5 times higher, and the absorption maxima are red-shifted by ∼5 nm compared with those of P-Si$(OEt)_3$ SAMs, suggesting tighter packing of CPTPP on oxide surfaces.[2a,8e] Because the effective surface area of core ZnOr is varying slightly from sample to sample, there is difference in the absorbance between the same SAM formed on the modified ZnOr substrates. The absorption spectrum of P-Si$(OEt)_3$ SAM on ZnOr|ZnO (2 or 5 nm) was similar to that of ZnOr, and thus the spectrum is not shown.

The interactions at semiconductor-organic SAM interfaces were monitored by comparing fluorescence intensities and lifetimes of the SAMs. The fluorescence of the porphyrin SAM on the semiconductor surface can be quenched due to (1) the intermolecular interactions in the SAM and (2) the interaction with metal oxide surface.[16] In the case of Al_2O_3, the fluorescence is expected to be quenched only due to intermolecular interaction in the SAM, whereas on ZnO and TiO_2, the interaction with metal oxide is expected to contribute strongly to the fluorescence quenching. The emission spectra of the both SAMs on TiO_2, Al_2O_3, and ZnO surfaces are shown in Figure 8. Emission intensities are normalized with respect to

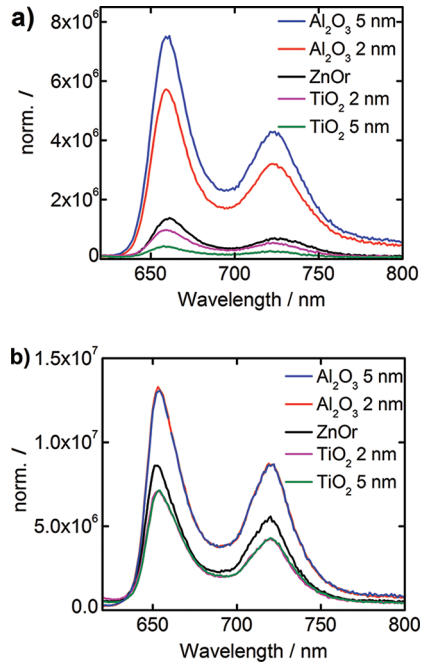

Figure 8. Normalized emission spectra with respect to the relative amount of the excitation light absorbed by the film of CPTPP (a) and P-Si$(OEt)_3$ (b) SAMs on ZnOr, ZnOr|Al_2O_3 (2 or 5 nm) and ZnOr|TiO_2 (2 or 5 nm).

the relative amount of the excitation light absorbed by the film. The shapes of the spectra are comparable, and there is practically no difference in emission intensities between the same SAMs on ZnOr|Al_2O_3 2 or 5 nm. Considering that Al_2O_3 is a dielectric medium and cannot contribute to the fluorescence quenching, one can conclude that a few nanometers separation between porphyrin SAM and semiconductor surface is sufficient for prohibiting electronic interactions between the SAM and semiconductor. The remaining fluorescence quenching for the SAMs on Al_2O_3 is due to porphyrin aggregation in the layer, which is in agreement with numerous previous studies.[2a,8b,e]

Even though both porphyrins form SAMs with compatible absorptions, the emission properties are quite different. P-Si$(OEt)_3$ SAM shows strong emission on all oxide substrates compared with that of CPTPP SAM. This can be explained by the two major differences in the structure of the porphyrins. First, the bulky *tert*-butyl groups in P-Si$(OEt)_3$ reduce aggregation and self-quenching due to intermolecular interactions in the SAM. The second reason for stronger emission of P-Si$(OEt)_3$ SAM is a longer linker, which increases the distance between the chromophore and the surface and reduces the

dx.doi.org/10.1021/jp2104769 | J. Phys. Chem. C 2012, 116, 2336−2343

Table 1. Fluorescence Lifetimes (τ_i) and Pre-Exponential Factors (a) Calculated from Bi-Exponential Fits Of TCSPC Decays of CPTPP and P-Si(OEt)$_3$ SAMs on Oxide Surfaces[a]

sample	τ1 [ns] a1 [%]	τ2 [ns] a2 [%]	τ_{avg} [ns]	χ^2	rel. emission (660 nm)	rel. τ_{avg}
ZnOr|Al_2O_3 (5 nm)|CPTPP	0.46 73.2	1.31 26.8	0.69	1.19	1.00	1.00
ZnOr|Al_2O_3 (2 nm)|CPTPP	0.41 78.6	1.26 21.4	0.59	1.29	0.77	0.86
ZnOr| CPTPP	0.17 90.4	0.49 9.6	0.20	1.88	0.18	0.29
ZnOr|TiO_2 (2 nm)|CPTPP	0.16 93.2	0.88 6.2	0.21	1.74	0.13	0.30
ZnOr|TiO_2 (5 nm)|CPTPP	0.062 93.2	0.39 6.8	0.08	1.40	0.06	0.12
ZnOr|Al_2O_3 (5 nm)|P-Si(OEt)$_3$	0.81 51.9	1.98 48.1	1.37	1.21	1.00	1.00
ZnOr|Al_2O_3 (2 nm)|P-Si(OEt)$_3$	0.94 47.4	2.23 52.6	1.62	1.16	1.01	1.18
ZnOr|P-Si(OEt)$_3$	0.70 78.3	2.28 21.7	1.04	1.65	0.61	0.76
ZnOr|TiO_2 (2 nm)|P-Si(OEt)$_3$	0.63 79.2	2.86 20.8	1.09	1.77	0.54	0.80
ZnOr|TiO_2 (5 nm)|P-Si(OEt)$_3$	0.61 75.6	2.65 24.4	1.11	1.72	0.55	0.81

[a] τ_{avg} is amplitude-weighted lifetime and χ^2 is weighted mean square deviation. Relative emission maximum and the fluorescence lifetime are presented in the last two columns.

interaction between the two.[8e] The latter can also explain the weak dependence of the emission intensity on the supporting semiconductor for P-Si(OEt)$_3$ SAM compared with that of CPTPP SAM. The emission intensity of CPTPP is the highest on the ZnOr|Al_2O_3 (5 nm) and lowest (17 times lower) on ZnOr|TiO_2 (5 nm). On the contrary, P-Si(OEt)$_3$ SAMs on ZnOr|Al_2O_3 (2 or 5 nm) have only approximately two times higher emission intensity than on ZnOr or ZnOr|TiO_2 (2 or 5 nm).

Emission decays of the porphyrin SAMs on ZnOr and ZnOr|TiO_2 or Al_2O_3 were measured by time-correlated single photon counting (TCSPC) method. The results of biexponential decay fits, comparison of emission intensities, and average fluorescence lifetimes are presented in Table 1. Some examples of the decay curves are presented in the Figure 9. A relatively thick

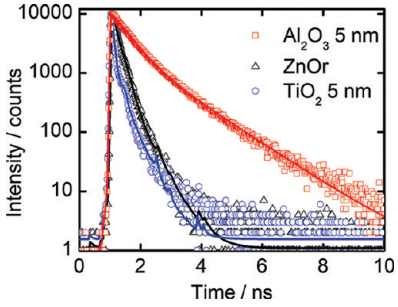

Figure 9. Fluorescence decay curves of CPTPP SAM on Al_2O_3 (red square), ZnO (black triangle), and TiO_2 (blue circle) surfaces.

layer of Al_2O_3 is expected to cancel all electronic interactions of the SAM with the oxide surface. The difference in the emission lifetimes of CPTPP SAM on the ZnOr|Al_2O_3 (2 and 5 nm) is rather small. Therefore, one may safely assume that 5 nm is a thick enough layer to prevent the interactions, and the fluorescence quenching is exclusively due to aggregation of the CPTPP molecules in SAM. For ZnOr|Al_2O_3 (2 nm), the lifetime is somewhat shorter, 0.59 vs 0.69 ns, and additional minor quenching of the fluorescence can be attributed to a weak interaction between ZnO and porphyrin SAM through 2 nm thick layer of Al_2O_3. Much stronger quenching is observed for CPTPP SAM on ZnOr, in which case the average emission lifetime is 0.2 ns. Comparing this lifetime to that of the same SAM on ZnOr|Al_2O_3 (5 nm), one can estimate the average rate constant of the quenching due to interaction between the SAM and the ZnO to be 3.6×10^9 s^{-1}. The strongest SAM-semiconductor quenching effect is observed for ZnOr|TiO_2 (5 nm) with the average rate constant of 1.1×10^{10} s^{-1}. On the basis of these experiments, a 2 nm layer of TiO_2 is not thick enough to switch surface properties completely from ZnO to TiO_2. The fluorescence lifetime is almost the same as that for ZnO sample, and the emission intensity is decreased only slightly.

The self-quenching in the P-Si(OEt)$_3$ SAM is weaker than in CPTPP SAM, and the average fluorescence lifetime on ZnOr|Al_2O_3 (5 nm) is 1.37 ns. Only minor decrease in the fluorescence lifetimes can be seen when the layers are deposited on ZnOr or ZnOr|TiO_2 (2 or 5 nm). The reasons for these observations are the structural differences between CPTPP and P-Si(OEt)$_3$, as previously discussed. Table 1 presents the relative emission intensities, and the average fluorescence lifetimes are normalized with respect to those on ZnOr|Al_2O_3 (5 nm), where only intramolecular interactions are expected to occur.

The relative fluorescence intensity and lifetime are in a reasonable agreement for P-Si(OEt)$_3$ SAM, but more than two time difference can be seen for CPTPP SAMs on ZnOr|TiO_2. This indicates that faster unresolved quenching processes may take place. Recent studies of dye-sensitized TiO_2 nanoparticles indicate that interfacial electron transfer takes place in picosecond and even subpicosecond time domains.[2] Preliminary studies of CPTPP SAMs on ZnOr and ZnOr|TiO_2 (5 nm) and ZnOr|Al_2O_3 (5 nm) were carried out using femtosecond pump–probe method (Supporting Information, Figure S9). The results revealed the presence of the ultrafast quenching processes and even indicated that the interfacial electron transfer can be the mechanism of enhanced fluorescence quenching in the case of ZnOr|TiO_2 and ZnOr|Al_2O_3 samples. However a more thorough investigation with wider range of SAM compounds is required to distinguish in-layer and interfacial interactions and also to establish the nature of interfacial interactions.

CONCLUSIONS

Dense arrays of ZnO nanorods can be grown in a controlled way by optimizing the ZnO seed layer, precursor concentration, and reaction temperature. The absorption of porphyrin SAM on the ZnOr surface gives valuable information about the sample morphology. The absorbance of SAM increased with the specific surface area of nanorods, and the effect of the length and density of ZnOr on the surface area was easily observed. For shorter nanorods (l < 500 nm) a simplified

dx.doi.org/10.1021/jp2104769 | J. Phys. Chem. C 2012, 116, 2336–2343

calculation model can be used to evaluate dependence of the increase in effective surface area on the ZnOr size and density.

Furthermore, the surface electronic properties of the nanorods can be modified by depositing a thin layer of Al_2O_3 or TiO_2 on ZnOr by the ALD method. At least two types of anchor groups, carboxylic acid or triethoxysilane, can be used to form SAMs with compatible density of molecules on all three types of nanorods. On the basis of the preliminary photophysical studies, the effect of the modification layer on interactions at the interface is the largest for the CPTPP SAMs, where the molecules are tightly packed closer to the surface. The fluorescence of CPTPP SAM is quenched efficiently when the layer is formed on the 5 nm thick TiO_2. On the contrary, a 5 nm thick layer of Al_2O_3 act as an insulating barrier, canceling the interfacial interactions and enabling studies of photophysical properties of the SAM itself.

On the basis of the presented results, the ZnO nanorod arrays are versatile model substrates to study electronic interactions between the organic SAM and supporting semiconductor surface. The hydrothermal growth method of ZnOr provides reasonable degree of morphology tuning to construct organic SAMs of interest, and electronic properties of ZnOr can be altered in a controlled way by ALD method. These kinds of model systems enable detailed interfacial studies by time-resolved spectroscopic methods.

■ ASSOCIATED CONTENT

Supporting Information

Additional SEM images of ZnO nanorods, absorption, and emission spectra of porphyrin SAMs on ZnO, TiO_2, and Al_2O_3 surfaces. This material is available free of charge via the Internet at http://pubs.acs.org.

■ AUTHOR INFORMATION

Corresponding Author

*E-mail: hanna.saarenpaa@tut.fi. Tel. +35840 198 1124. Fax +3583 3115 2108.

■ ACKNOWLEDGMENTS

H.S. and E.S.-L. are grateful to doctoral program of the President of the Tampere University of Technology for the financial support. H.I., N.T., H.L., and H.S. thank the Strategic Japanese-Finish Cooperative Program (JST, Tekes, and AF). H.H. is grateful for a JSPS Fellowship for Young Scientists.

■ REFERENCES

(1) (a) Hagfeldt, A.; Boschloo, G.; Sun, L.; Kloo, L.; Pettersson, H. *Chem. Rev.* **2010**, *110*, 6595. (b) Araki, N.; Amao, Y.; Funabiki, T.; Kamitakahara, M.; Ohtsuki, C.; Mitsuo, K.; Asai, K.; Obata, M.; Yano, S. *Photochem. Photobiol. Sci.* **2007**, *6*, 794.

(2) (a) Imahori, H.; Kang, S.; Hayashi, H.; Haruta, M.; Kurata, H.; Isoda, S.; Canton, S. E.; Infahsaeng, Y.; Kathiravan, A.; Pascher, T.; Chábera, P.; Yartsev, A. P.; Sundström, V. *J. Phys. Chem. A* **2011**, *115*, 3679. (b) Asbury, J. B.; Hao, E.; Wang, Y.; Ghosh, H. N.; Lian, T. *J. Phys. Chem. B* **2001**, *105*, 4545. (c) Varaganti, S.; Ramakrishna, G. *J. Phys. Chem. C* **2010**, *114*, 13917. (d) Szarko, J. M.; Neubauer, A.; Bartelt, A.; Socaciu-Siebert, L.; Birkner, F.; Schwarzburg, K.; Hannappel, T.; Eichberger, R. *J. Phys. Chem. C* **2008**, *112*, 10552.

(3) (a) Zhang, Q.; Dandeneau, C. S.; Zhou, X.; Cao, G. *Adv. Mater.* **2009**, *21*, 4087. (b) Yi, G.-C.; Wang, C.; Park, W. I. *Semicond. Sci. Technol.* **2005**, *20*, S22. (c) Weintraub, B.; Zhou, Z.; Li, Y.; Deng, Y. *Nanoscale* **2010**, *2*, 1573.

(4) (a) Ma, T.; Guo, M.; Zhang, M.; Zhang, Y.; Wang, X. *Nanotechnology* **2007**, *18*, 035605. (b) Guo, M.; Diao, P.; Cai, S. *J. Solid State Chem.* **2005**, *178*, 1864. (c) Kim, K. S.; Jeong, H.; Jeong, M. S.; Jung, G. Y. *Adv. Funct. Mat.* **2010**, *20*, 3055. (d) Gonzalez-Valls, I.; Yu, Y.; Ballesteros, B.; Oro, J.; Lira-Cantu, M. *J. Power Sources* **2011**, *196*, 6609. (e) Greene, L. E.; Law, M.; Tan, D. H.; Montano, M.; Goldberger, J.; Somorjai, G.; Yang, P. *Nano Lett.* **2005**, *5*, 1231. (f) Vayssieres, L. *Adv. Mater.* **2003**, *15*, 464. (g) Guo, M.; Diao, P.; Wang, X.; Cai, S. *J. Solid State Chem.* **2005**, *178*, 3210.

(5) (a) Yamada, H.; Imahori, H.; Nishimura, Y.; Yamazaki, I.; Ahn, T. K.; Kim, S. K.; Fukuzumi, S. *J. Am. Chem. Soc.* **2003**, *125*, 9129. (b) Imahori, H.; Kimura, M.; Hosomizu, K.; Sato, T.; Ahn, T. K.; Kim, S. K.; Kim, D.; Nishimura, Y.; Yamazaki, I.; Araki, Y.; Ito, O.; Fukuzumi, S. *Chem.—Eur. J.* **2004**, *10*, 5111. (c) Isosomppi, M.; Tkachenko, N. V.; Efimov, A.; Kaunisto, K.; Hosomizu, K.; Imahori, H.; Lemmetyinen, H. *J. Mater. Chem.* **2005**, *15*, 4546. (d) Thyagarajan, S.; Galoppini, E.; Persson, P.; Giaimuccio, J. M.; Meyer, G. J. *Langmuir* **2009**, *25*, 9219.

(6) (a) Ulman, A. *Chem. Rev.* **1996**, *96*, 1533. (b) Love, J. C.; Estroff, L. A.; Kriebel, J. K.; Nuzzo, R. G.; Whitesides, G. M. *Chem. Rev.* **2005**, *105*, 1103. (c) Yip, H.-L.; Hau, S. K.; Baek, N. S.; Ma, H.; Jen, A. K.-Y. *Adv. Mater.* **2008**, *20*, 2376.

(7) (a) Campbell, W. M.; Burrell, A. K.; Officer, D. L.; Jolley, K. W. *Coord. Chem. Rev.* **2004**, *248*, 1363. (b) Bessho, T.; Zakeeruddin, S. M.; Yeh, C.-Y.; Diau, E. W.-G.; Grätzel, M. *Angew. Chem., Int. Ed.* **2010**, *122*, 6796. (c) Martínez-Díaz, M. V.; de la Torre, G.; Torres, T. *Chem. Commun.* **2010**, *46*, 7090. (d) Imahori, H.; Umeyama, T.; Ito, S. *Acc. Chem. Res.* **2009**, *42*, 1809.

(8) (a) Rochford, J.; Chu, D.; Hagfeldt, A.; Galoppini, E. *J. Am. Chem. Soc.* **2007**, *129*, 4655. (b) Imahori, H.; Hayashi, S.; Hayashi, H.; Oguro, A.; Eu, S.; Umeyama, T.; Matano, Y. *J. Phys. Chem. C* **2009**, *113*, 18406. (c) Rochford, J.; Galoppini, E. *Langmuir* **2008**, *24*, 5366. (d) Imahori, H.; Matsubara, Y.; Iijima, H.; Umeyama, T.; Matano, Y.; Ito, S.; Niemi, M.; Tkachenko, N. V.; Lemmetyinen, H. *J. Phys. Chem. C* **2010**, *114*, 10656. (e) Imahori, H.; Hosomizu, K.; Mori, Y.; Sato, T.; Ahn, T. K.; Kim, S. K.; Kim, D.; Nishimura, Y.; Yamazaki, I.; Ishii, H.; Hotta, H.; Matano, Y. *J. Phys. Chem. B* **2004**, *108*, 5018.

(9) (a) Law, M.; Greene, L. M.; Radenovic, A.; Kuykendall, T.; Liphardt, J.; Yang, P. *J. Phys. Chem. B* **2006**, *110*, 22652. (b) Ganapathy, V.; Karunagaran, B.; Rhee, S.-W. *J. Power Sources* **2010**, *195*, 5138. (c) Park, K.; Zhang, Q.; Garcia, B. B.; Cao, G. *J. Phys. Chem. C* **2011**, *115*, 4927.

(10) (a) Baik, C.; Kim, D.; Kang, M.-S.; Kang, S. O.; Ko, J.; Nazeeruddin, M. K.; Grätzel, M. *J. Photochem. Photobiol. A* **2009**, *201*, 168. (b) Sariola-Leikas, E.; Hietala, M.; Veselov, A.; Okhotnikov, O.; Semjonov, S. L.; Tkachenko, N. V.; Lemmetyinen, H.; Efimov, A. *J. Colloid Interface Sci.* **2012**, DOI: 10.1016/j.jcis.2011.12.044. (c) Taratula, O.; Galoppini, E.; Wang, D.; Chu, D.; Zhang, Z.; Chen, H.; Saraf, G.; Lu, Y. *J. Phys. Chem B* **2006**, *110*, 6506. (d) Allen, C. G.; Baker, D. J.; Albin, J. M.; Oertli, H. E.; Gillaspie, D. T.; Olson, D. C.; Furtak, T. E.; Collins, R. T. *Langmuir* **2008**, *24*, 13393.

(11) Hayashi, H.; Kira, A.; Umeyama, T.; Matano, Y.; Charoensirithavorn, P.; Sagawa, T.; Yoshikawa, S.; Tkachenko, N. V.; Lemmetyinen, H.; Imahori, H. *J. Phys. Chem. C* **2009**, *113*, 10819.

(12) Saarenpää, H.; Niemi, T.; Tukiainen, A.; Lemmetyinen, H.; Tkachenko, N. V. *Sol. Energy Mater. Sol. Cells* **2010**, *94*, 1379.

(13) (a) Aarik, J.; Aidla, A.; Mändar, H.; Sammelselg, V. *J. Cryst. Growth* **2000**, *220*, 531. (b) Aarik, J.; Aidla, A.; Mändar, H.; Uustare, T.; Schuisky, M.; Hårsta, A. *J. Cryst. Growth* **2002**, *242*, 189.

(14) (a) Elam, J. W.; Sechrist, Z. A.; George, S. M. *Thin Solid Films* **2002**, *414*, 43. (b) Higashi, G. S.; Fleming, C. G. *Appl. Phys. Lett.* **1989**, *55*, 1963.

(15) Wang, M.; Wang, J.; Chen, W.; Cui, Y.; Wang, L. *Mater. Chem. Phys.* **2006**, *97*, 219.

(16) Lu, H.-P.; Tsai, C.-Y.; Yen, W.-N.; Hsieh, C.-P.; Lee, C.-W.; Yeh, C.-Y.; Diau, E. W.-G. *J. Phys. Chem C* **2009**, *113*, 20990.

Supporting information

Self-assembled porphyrins on modified zinc oxide nanorods: development of model systems for inorganic-organic semiconductor interface studies

Hanna Saarenpää*, Essi Sariola-Leikas, Alexander Pyymaki Perros, Juha M. Kontio, Alexander Efimov, Hironobu Hayashi, Harri Lipsanen, Hiroshi Imahori, Helge Lemmetyinen, and Nikolai V. Tkachenko

*Corresponding author:

E-mail:hanna.saarenpaa@tut.fi

tel. +35840 198 1124

fax +3583 3115

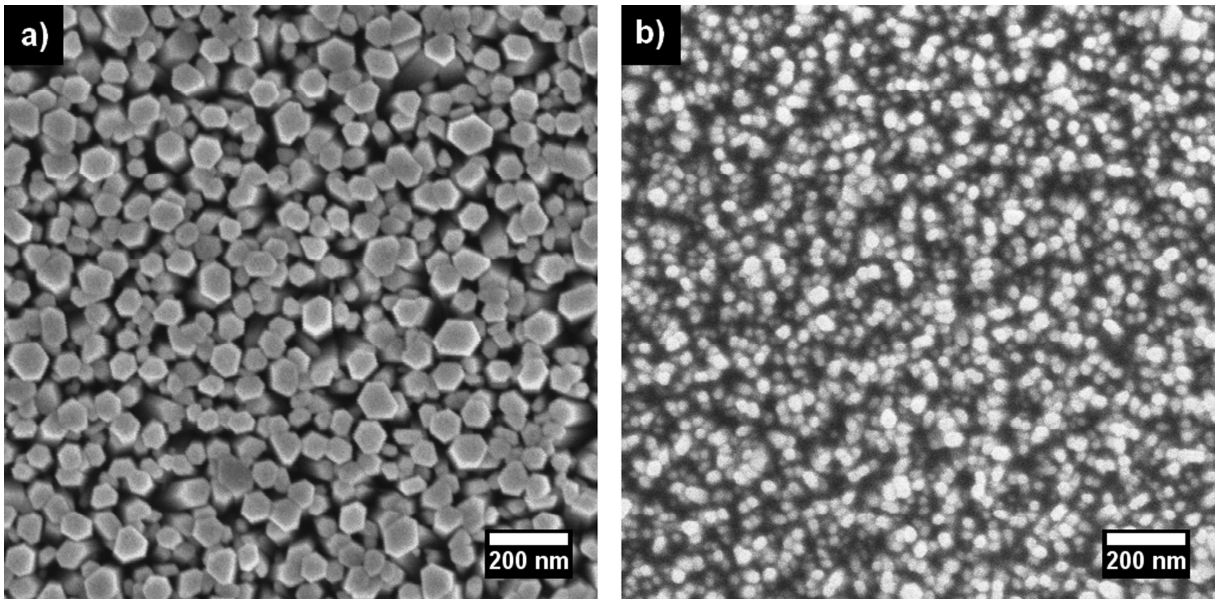

Figure S1. SEM images of ZnOr grown at 80^0C for 2.5 h on seed layer B using 0.05 M (a) and 0.02 M (b) precursors.

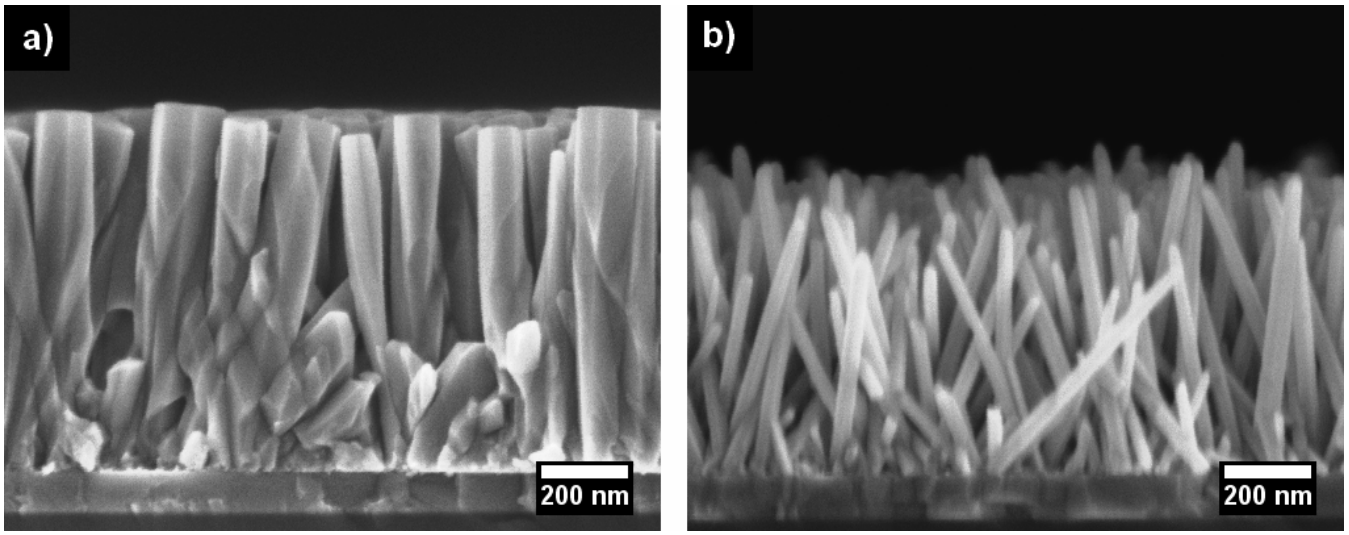

Figure S2. SEM images of ZnOr grown at 80^0C for 6 h on seed layer A using 0.05 M (a) and 0.02 M (b)

precursors.

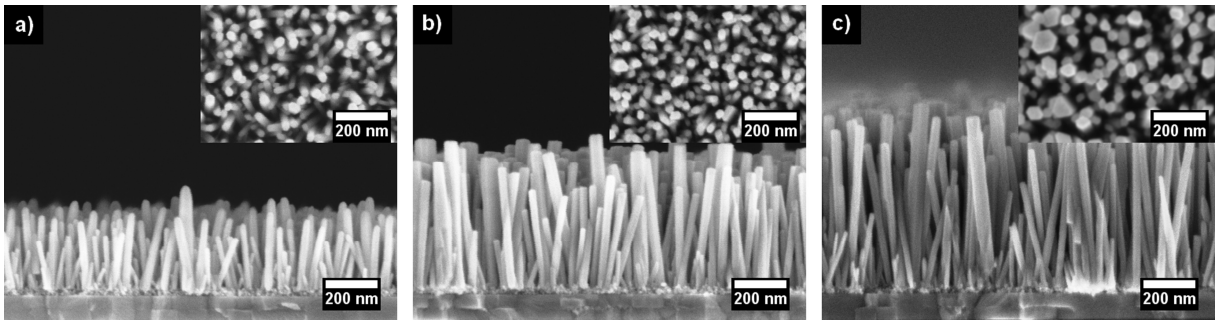

Figure S3. SEM images of ZnOr grown at 80^0C (a), 85^0C (b) and 90^0C (c) for 4 h on a seed layer B

using 0.02 Mprecursors.

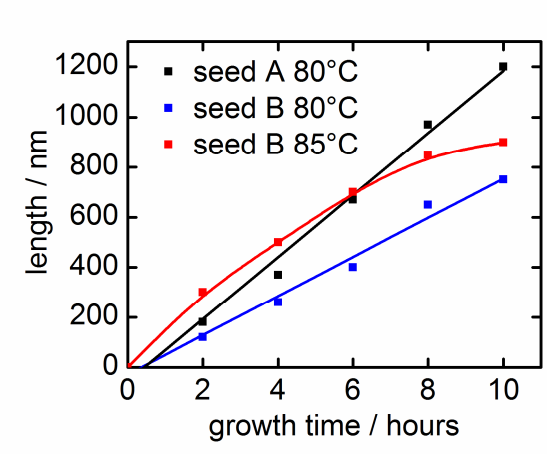

Figure S4. The length of ZnOr grown on seeds A at 80^{0}C (black) and on seed B at 80^{0}C (blue) and 85^{0}C (red) as a function of the reaction time. The precursor solution is not changed during the growth.

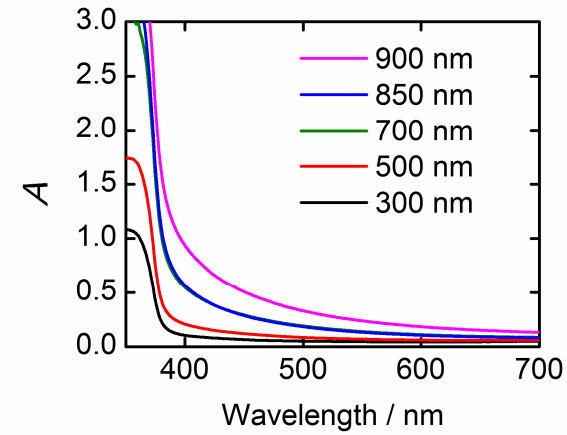

Figure S5. Absorption spectra of ZnOr substrates grown on seed B at 85^{0}C for 2-10 h.

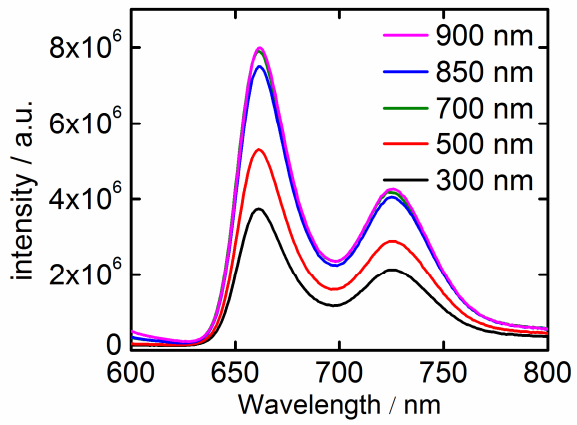

Figure S6. Emission spectra of CPTPP SAM on ZnOr. (Nanorods were grown on seed B at 85^0C for 2-10 h using 0.02 M precursors).

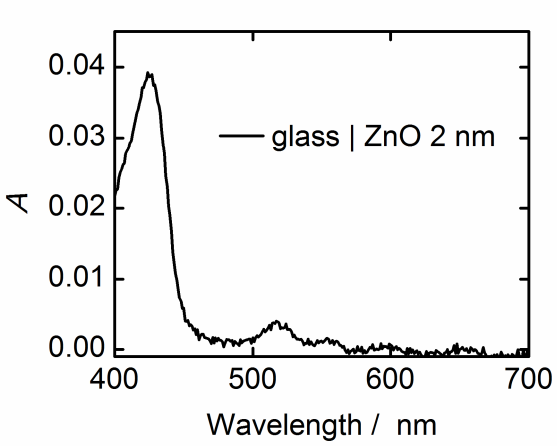

Figure S7. Absorption spectrum of CPTPP SAM on glass | ZnO (2 nm).

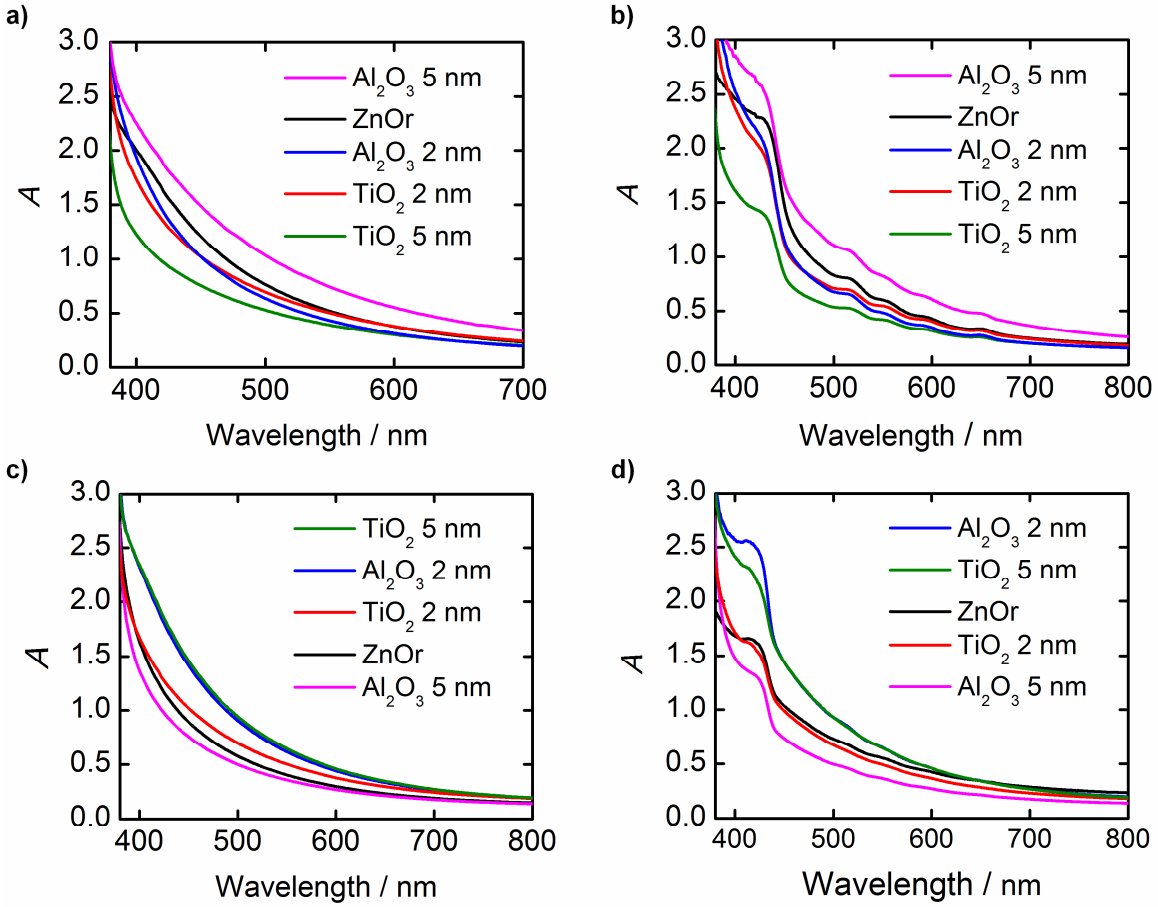

Figure S8. Absorption spectra of the a) oxide substrates of CPTPP SAMs and b) P-Si(OEt)$_3$ SAMs, c) absorption spectra of CPTPP SAMs and d) P-Si(OEt)$_3$ SAMs on oxide substrates without substrate subtraction.

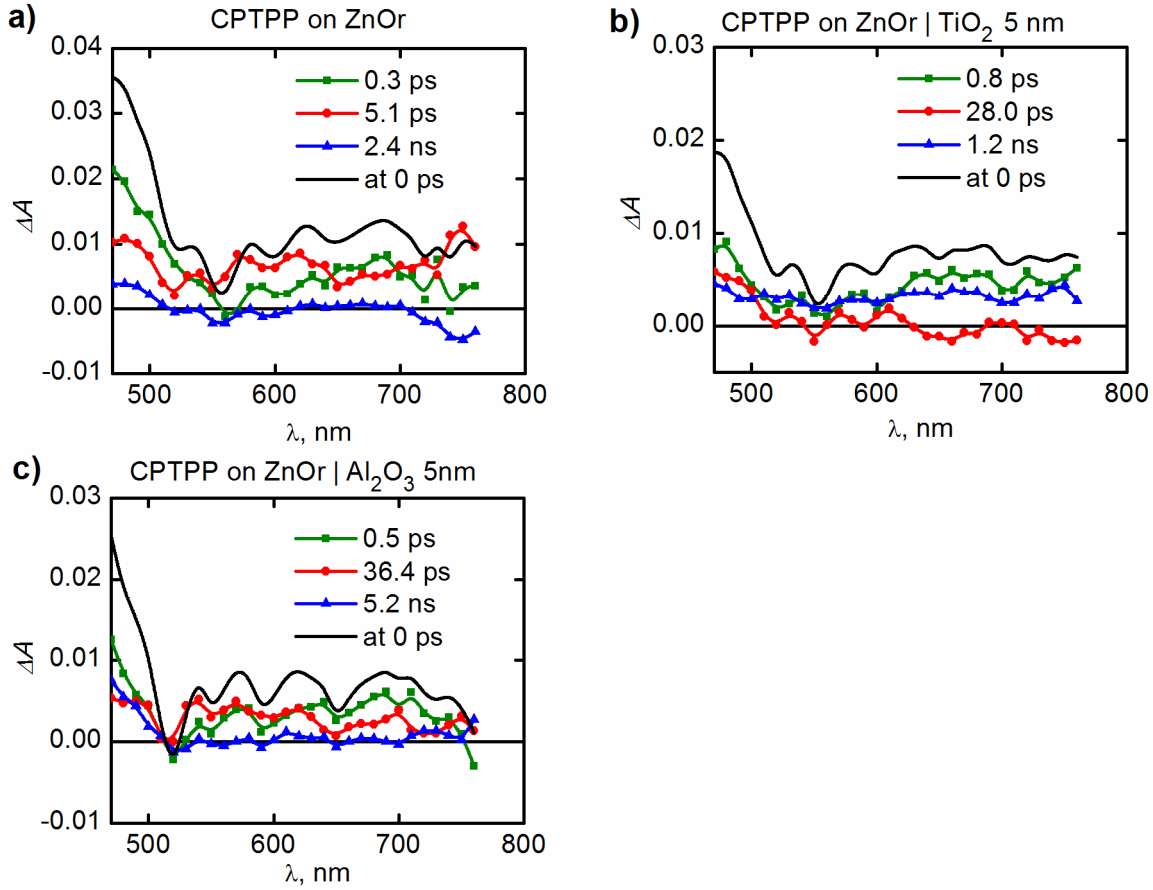

Figure S9. Decay component spectra (lines with symbols) of CPTPP SAM on ZnO (a), TiO_2 (b), and Al_2O_3 (c) surfaces. The component lifetimes are indicated in the plots. The black solid lines present the time resolved spectra right after the excitation (at 0 ps). The zero delay time spectrum of the Al_2O_3 sample agrees well with the transient spectrum of the singlet excited state of porphyrin (as expected). However in the case of ZnO and TiO_2 samples the increased absorption in the 600-700 nm range indicate presence of some amount of porphyrin cations, which are formed with time constant shorter than the time resolution of the instrument. In a qualitative level the porphyrin cations are longer-lived in TiO_2 than in ZnO sample (0.8 vs 0.3 ps). However more advanced studies are required for quantitative evaluation of the excitation relaxation processes in such samples.

III

PHOTOINDUCED ELECTRON TRANSFER AT NANOSTRUCTURED SEMICONDUCTOR-ZINC PORPHYRIN INTERFACE

by

Hanna Saarenpää, Alexander Pyymaki Perros, Pasi Myllyperkiö, Kei Kurotobi, Harri Lipsanen, Hiroshi Imahori, Helge Lemmetyinen and Nikolai V. Tkachenko, 2014

Chemical Physics Letters vol. 592, 47-51

Chemical Physics Letters 592 (2014) 47–51

Contents lists available at ScienceDirect

Chemical Physics Letters

journal homepage: www.elsevier.com/locate/cplett

Photo-induced electron transfer at nanostructured semiconductor–zinc porphyrin interface

Hanna Hakola [a,*], Alexander Pyymaki Perros [b], Pasi Myllyperkiö [c], Kei Kurotobi [d], Harri Lipsanen [b], Hiroshi Imahori [d,e], Helge Lemmetyinen [a], Nikolai V. Tkachenko [a]

[a] Department of Chemistry and Bioengineering, Tampere University of Technology, P.O. Box 541, FI-33101 Tampere, Finland
[b] Department of Micro- and Nanosciences, Aalto University, P.O. Box 13500, FI-00076 Aalto, Finland
[c] Department of Chemistry, University of Jyväskylä, P.O. Box 35, FI-40014 Jyväskylä, Finland
[d] Institute for Integrated Cell-Material Sciences (WPI-iCeMS), Kyoto University, Nishikyo-ku, Kyoto 615-8510, Japan
[e] Department of Molecular Engineering, Graduate School of Engineering, Kyoto University, Nishikyo-ku, Kyoto 615-8510, Japan

ARTICLE INFO

Article history:
Received 12 September 2013
In final form 4 November 2013
Available online 20 November 2013

ABSTRACT

Electron transfer at metal oxide–organic dye interface on ZnO nanorod (ZnOr) templates was studied by femtosecond absorption spectroscopy method. Further confirmation of the electron transfer was obtained from photoelectrical studies. The fastest electron transfer from zinc porphyrin (ZnP) to semiconductor was observed for ZnOr modified by a 5 nm layer of TiO_2 (<0.2 ps). The charge recombination processes were not affected by the TiO_2 being faster than at the interface of TiO_2 nanoparticle and ZnP. This indicates that the charge recombination depends mainly on semiconductor bulk properties whereas the charge separation is determined by the organic-semiconductor interface.

1. Introduction

Controlled surface functionalization and in-depth understanding of photoinduced processes at the organic dye–inorganic semiconductor interface are the key factors to improve the efficiency of photovoltaic devices [1–4]. Sensitizer–semiconductor interface in real devices is a complex object and the surface properties vary depending on multiple factors [4,5]. Therefore the use of simplified model samples is essential to gain fundamental knowledge on electron transfer (ET) processes. So far, the major part of those samples consists of new organic photoactive molecules assembled on the film of commercial TiO_2 nanoparticles [6–11]. These studies give valuable information for the design of the sensitizers. At the same time, the effect of semiconductors properties on the interfacial ET processes was widely discussed, though the key factors affecting the processes need better understanding [4,5].

ZnO has been considered as a good alternative to TiO_2 for photovoltaic applications [1,3,12–15]. Bulk band gaps of ZnO and TiO_2 are similar, whereas ZnO has higher electron mobility than TiO_2. There are some advantages to use ZnO nanostructures in fundamental ET studies. Firstly, several fabrication methods are available and various controllable morphologies are possible to prepare. Secondly, Atomic Layer Deposition (ALD) is an accurate method to deposit additional layers of metal oxides (MO) conformally on ZnO nanostructures [15]. The core–shell structures were the shell is prepared by ALD are promising materials for practical applications such as photoanodes in dye sensitized solar cells (DSSC) or photoelectrochemical water splitting systems [15–18].

The aim of this letter was to study fundamental ET processes at metal oxide (MO)–organic dye interface. The samples were prepared using ZnO nanorods (ZnOr) as templates, covering them with a 5 nm layer of Al_2O_3 or TiO_2 and depositing zinc porphyrin (ZnP) photosensitizer layer on top of the MO nanostructures. Femtosecond transient absorption (TA) measurements were performed to study in detail the electron transfer kinetics from ZnP to MO. To link primary reactions at the sensitizer–semiconductor interface with real applications, the DSSC experiments were carried out using the same structures as in the TA study.

2. Materials and methods

2.1. Sample preparation

The preparation of ZnOr substrates for spectroscopic measurements has been described in detail previously [19]. Briefly, ZnOr were grown by hydrothermal method and were modified by growing a 5 nm thick layer of Al_2O_3 or TiO_2 by ALD. A 2 μm thick layer of TiO_2 nanoparticles (Solaronix: Ti-Nanoxide-T, denoted later as TiO_2p) was formed on the glass substrates by a standard doctor blading technique [10]. 5-(4-Carboxyphenyl)-10,15,20-tris(2,4,6-trimethylphenyl)porphyrinatozinc(II) (ZnP) shown in Figure 1 was chosen as a sensitizer for this study [11]. The modified ZnO substrates and TiO_2p film were sensitized in a 0.2 mM ZnP in

* Corresponding author.
E-mail address: hanna.hakola@tut.fi (H. Hakola).

0009-2614/$ - see front matter © 2013 Elsevier B.V. All rights reserved.
http://dx.doi.org/10.1016/j.cplett.2013.11.028

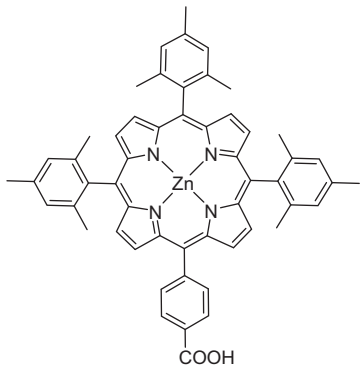

ZnP

Figure 1. Structure of studied zinc porphyrin, ZnP.

methanol at room temperature for 1 h [10]. Finally, the plates were rinsed thoroughly with methanol in order to remove all physisorbed ZnP molecules. The samples are denoted as ZnOr/ZnP, ZnOr/Al_2O_3/ZnP, ZnOr/TiO_2/ZnP and TiO_2p/ZnP later in the text.

The preparation of ZnOr on FTO substrates for the DSSC experiments was similar to that as described for ITO [19]. The only difference was the number of spin coated ZnO seed layers. Two layers were required to ensure conformal ZnO seed layer on a rough FTO substrate. In addition to Al_2O_3 or TiO_2 modification layers, one set of ZnOr on FTO was modified by a 5 nm layer of ZnO. The FTO/ZnOr based electrodes were immersed into 0.2 mM ZnP in methanol for 24 h and after the reaction rinsed carefully with pure solvent. Otherwise the DSSC samples were prepared as previously described [10].

2.2. Sample characterization

The morphology of ZnOr and TiO_2 nanoporous films were studied using a field emission scanning electron microscope (FE-SEM, Carl Zeiss Ultra 55). Absorption spectra were recorded by a Shimadzu UV-360 spectrophotometer. Steady state emission was measured by Fluorolog 3 fluorimeter using the correction function supplied by the manufacturer and all samples were excited at 430 nm. A time-correlated single-photon counting (TCSPC) system (PicoQuant GmbH) consisting of a PicoHarp controller and PDL-800-B driver was used for time-resolved fluorescence measurements. The samples were excited by a pulsed LED (LDH-P-C-405B) at 405 nm and fluorescence decays were monitored at 605 nm. Time resolution of the TCSPC measurements was approximately 60–70 ps (FWHM). The Fourier transform infrared attenuated total reflectance (FT-IR-ATR) spectra were measured using a Perkin Elmer Spectrum One FT-IR Spectrometer equipped with a diamond crystal. The contact force between the sample and the crystal was kept the same for all samples and 64 scans were recorded with a resolution of 2 cm^{-1}.

For the transient absorption measurements, an integrated one-box femtosecond laser system (Integra-C 3.5 mJ, Quantronix) was used to pump two home-built non-collinear parametric amplifiers (NOPAs) delivering pump (560 nm) and probe (660 nm) pulses for the experiment. The detection of transient absorption was done using traditional two beam arrangement (probe and reference beams) giving a detection limit well below 0.1 mOD over 1000 shots. The mutual polarization of the pump and probe pulses was set to magic angle (54.7°). The time-resolution in the experiment was determined to be ~80 fs by sum-frequency cross-correlation signal generated in 0.1 μm thick BBO-crystal at the sample position. A fast (~100 fs) response was observed for all ZnOr based samples regardless of TiO_2, Al_2O_3 or ZnP layers (Figure S1) and is tentatively attributed to two-photon absorption in ZnO [20]. This fast response was subtracted from the sample signals shown below but it reduces the accuracy of measurements in a short time scale, <200 fs.

The photocurrent–voltage performances were measured with a solar simulator (PEC-L10, Peccell Technologies) providing AM 1.5 excitation spectrum (100 mW/cm^2). The active area of the studied cell was 0.16 cm^2. Two cells of each sample type were measured and the average values are presented in the results.

3. Results and discussion

3.1. Sensitization of nanorods

Steady state absorption spectra of ZnP in methanol and ZnP SAMs on metal oxides are shown in Figure 2. The solution spectrum agrees well with the previous studies [10]. The absorbances of ZnP SAMs on ZnOr, ZnOr/Al_2O_3 and ZnOr/TiO_2 are 0.3–0.7 at maxima, the Soret bands, and 0.02–0.04 at the strongest Q bands observed at around 550 nm. These absorbance values are in agreement with those of recently published for free base porphyrin SAMs on similar ZnOr and suggest reasonably high coverage of the semiconductor surfaces by ZnP [19]. The variation in sample absorbances is mainly due to some differences in effective surface area of ZnOr templates (Figure S2). In addition, the light scattering by the nanorods disturbs the measured spectra of ZnP SAMs especially in the Soret band region. Despite the spectrum of each particular substrate has been subtracted from the spectrum of its corresponding ZnP SAM sample, the quantitative comparison of the sample absorbances is rather inaccurate. Nevertheless, it is evident that TiO_2p/ZnP has significantly higher (approximately ten times) absorbance than that of ZnP SAMs on ZnOr substrates. This is directly related to the higher effective surface area of the 2 μm thick mesoporous TiO_2p layer as compared to that of ZnOr (Figure S3).

The binding mode of ZnP layer on semiconductors was studied by FT-IT-ATR spectroscopy method [9,21,22]. The ATR spectra of a solid ZnP powder and ZnP bound to MO substrates are shown in Supporting information (Figure S4). The spectrum of solid ZnP has characteristic carboxylic acid stretching bands ν(C=O) and ν(C—O) at around 1700 and 1280 cm^{-1}, respectively. Upon binding these bands disappear and symmetric ($\nu(COO^-_{as})$) and asymmetric ($\nu(COO^-_{s})$) stretching bands of carboxylate groups appear at around 1400 and 1600 cm^{-1}. These characteristic features are observed

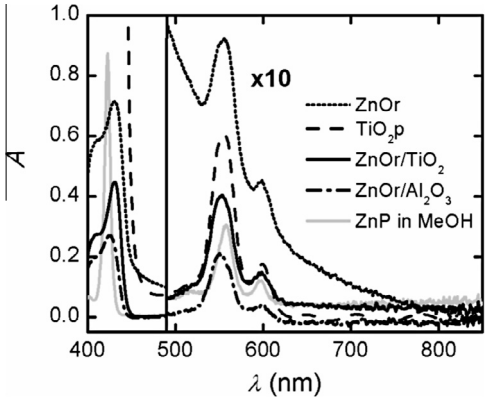

Figure 2. Absorption spectra of ZnP in methanol (solid gray) and in the ZnOr/ZnP (short dot), TiO_2p/ZnP (dash), ZnOr/TiO_2/ZnP (solid black), and ZnOr/Al_2O_3/ZnP (dash dot) samples. Except TiO_2p/ZnP, all the spectra are multiplied by a factor of ten in the range 490–850 nm.

when ZnP is bound to all studied substrates. The FT-IR-ATR signal intensity is not high in case of ZnOr based samples, but still a clear difference to the spectrum of solid unbound ZnP is found. The disappearance of strong ν(C=O) band in ZnP SAM spectra rules out the ester type binding mode and also indicates that no unbound ZnP is left on the metal oxide surfaces. The difference between the symmetric and asymmetric stretching bands of carboxylate group suggests bidentate binding mode of ZnP on all studied metal oxides.

3.2. Photoinduced electron transfer at the interface

After photoexcitation, at least two states can be formed in the ZnP layer, the singlet excited state, ZnP^S, and the ZnP radical cation, $ZnP^{\bullet+}$, which can be formed after the electron transfer from ZnP^S to the semiconductor [7]. However, there are other possible deactivation reactions for ZnP^S, such as intermolecular interactions and enhanced non-radiative relaxations in the ZnP layer itself. Fluorescence spectra of ZnOr/ZnP, ZnOr/Al_2O_3/ZnP, and ZnOr/TiO_2/ZnP shown in Figure 3 illustrates a strong dependence of the fluorescence intensity on the semiconductor substrate. The fluorescence intensity is strongest for ZnOr/Al_2O_3/ZnP and most quenched for ZnOr/TiO_2/ZnP. This supports our hypothesis that the 5 nm layer of Al_2O_3 blocks the interactions between ZnP and ZnOr, leaving the intermolecular interactions in the ZnP layer as the major pathway for ZnP^S quenching. For other samples, the formation of $ZnP^{\bullet+}$ is the major reason for reduced fluorescence intensity [15,19]. The measured average fluorescence lifetime for the ZnOr/Al_2O_3/ZnP is 0.34 ns, and in case of ZnOr/ZnP and ZnOr/TiO_2/ZnP the lifetime is close to the TCSPC instrument resolution, being approximately 0.1 ns (Figure S5). This also indicates that in the latter case the ZnP^S relaxation is strongly accelerated by interaction with the ZnO or TiO_2. The fluorescence of the TiO_2p/ZnP was quenched significantly stronger than that for ZnOr/TiO_2/ZnP and practically no signal was detected under otherwise identical measurement conditions. One reason for this can be increased intermolecular interactions. The probability of the dye–dye interactions in porous TiO_2p film can be high because the pore size is only few nanometers (Figure S3).

DSSC experiments provided another proof that Al_2O_3 layer suppress effectively the $ZnP^{\bullet+}$ formation. The photocurrent–voltage characteristics are shown in Figure 4 and the performance parameters are summarized in Table 1. The efficiency of the ZnOr/Al_2O_3/ZnP solar cell is almost zero (η = 0.001%). On the other hand, the ZnOr/ZnP, ZnOr/ZnO and ZnOr/TiO_2/ZnP cells have reasonable efficiencies compared to the low cell absorbances. Also for the same reason the photocurrent is roughly proportional to the cell

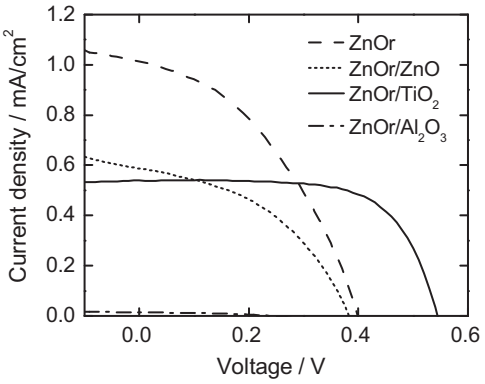

Figure 4. IV–characteristics of studied samples based on ZnOr photoanodes.

Table 1
Photovoltaic properties of the samples and the absorption at the strongest Q band at 550 nm.

Photoanode	J_{sc} (mA/cm^2)	U_{oc} (V)	*FF*	η (%)	$A_{550\ nm}$
ZnOr	1.0	0.40	0.42	0.17	0.060
ZnOr/ZnO	0.59	0.39	0.43	0.10	0.045
ZnOr/Al_2O_3	0.01	0.24	0.43	0.001	0.030
ZnOr/TiO_2	0.54	0.55	0.67	0.20	0.040

absorption for all cells except of ZnOr/Al_2O_3/ZnP. The most remarkable differences between the ZnOr/ZnP or ZnOr/ZnO/ZnP and ZnOr/TiO_2/ZnP cells are found in U_{oc} and *FF*. Adding the TiO_2 layer on ZnOr increases the U_{oc} by 38% (from 0.39 to 0.55 V) and *FF* by 60% (from 0.43 to 0.67).

The most detailed information on photoinduced processes at MO–ZnP SAM interface was obtained from TA measurements. The preliminary experiments were carried out by acquiring spectra in the range 460–760 nm (see SI, Figure S6) at varying the excitation densities. The aim was to find the excitation energy limit at which the signal decay profile does not depend on the excitation density. This study indicated that the sensitivity of the primary used system is not sufficient and another instrument optimized for detection of weak signals was used. However, this system is designed for TA decay measurements rather than for spectra studies. Therefore the most of the measurements were done with excitation at 560 nm and monitoring at 660 nm using 0.03 mJ/cm^3 excitation density.

Although 660 nm is optimum wavelength for monitoring, $ZnP^{\bullet+}$, ZnP^S state also has a contribution to the TA response at this

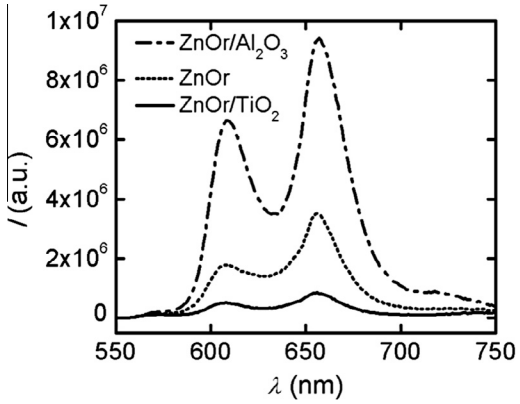

Figure 3. Emission spectra of the ZnOr/Al_2O_3/ZnP (dash dotted) ZnOr/ZnP (short dot), and ZnOr/TiO_2/ZnP (solid) samples.

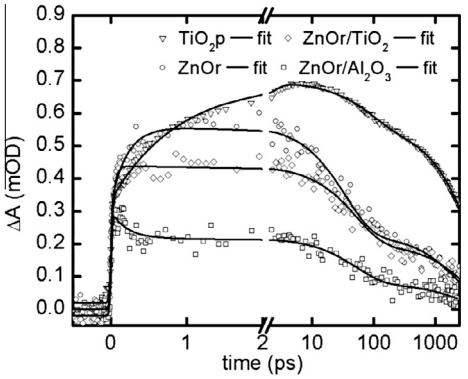

Figure 5. Transient absorption response of the ZnP SAMs on metal oxides. The signal intensity of TiO_2p/ZnP is divided by the factor of ten.

wavelength [6–8,23]. At first, with the excitation at 560 nm, the ZnP^S is populated and it gives an instant rise of the TA signal shown in Figure 5. The slower rise of the absorption at this wavelength can be attributed to the formation of $ZnP^{\cdot+}$ [6–8]. The slower part of the rise was not observed for ZnOr/Al_2O_3/ZnP sample, therefore there is no ET from ZnP to the semiconductor in this case. The analysis for the TA decays is not that straightforward, since the contributions of the ZnP^S and $ZnP^{\cdot+}$ cannot be separated. The decays of ZnOr/Al_2O_3/ZnP, ZnOr/TiO_2/ZnP and ZnOr/ZnP look roughly the same (Figure 5 and Table 2). The signal intensities in TA responses were rather weak thus the accuracy of the calculated lifetimes shown in Table 2 is approximately 30%. However, the TCSPC measurements show that at least at 100 ps delay time the population of ZnP^S of ZnOr/TiO_2/ZnP and ZnOr/ZnP samples is much lower than that of ZnOr/Al_2O_3/ZnP; therefore the TA response of ZnOr/TiO_2/ZnP and ZnOr/ZnP can be attributed to the decay of $ZnP^{\cdot+}$. In addition, the DSSC measurements (Figure 4) suggest that the ET is very inefficient process in the case of ZnOr/Al_2O_3/ZnP. These three observations, the rise of absorption in subpicosecond time for ZnOr/TiO_2/ZnP and ZnOr/ZnP only, much shorter fluorescence lifetime of the same samples and no photocurrent generation for ZnOr/Al_2O_3/ZnP, lead us to conclusion that origin of the transient absorption decays of these samples at 660 nm is different, although the lifetime is roughly the same. For ZnOr/TiO_2/ZnP and ZnOr/ZnP the signal decay is mainly due to $ZnP^{\cdot+}$, whereas in the case of ZnOr/Al_2O_3/ZnP it arises from ZnP^S.

Transient absorption kinetics of TiO_2p/ZnP is in agreement with previous studies carried out in presence of 1:1 tert-butanol:acetonitrile [7]. In our experiments carried out in air atmosphere, a clear rise of TA is seen for TiO_2p/ZnP with a time constant of 0.9 ps. At the ZnOr/ZnP interface, the ET is faster and takes place in a subpicosecond time domain (~0.3 ps). Even faster ET was observed for ZnOr/TiO_2/ZnP, but the time constant of the process interferes with the response of the ZnOr substrate and therefore can only be determined on a qualitative level to be <0.2 ps.

In part, these results are in contradiction with previous studies of ET dynamics on sensitized TiO_2 and ZnO nanoparticle thin films, which reported faster ET for TiO_2 than for ZnO [24–26]. Comparison however is not straightforward to make because the sensitizers and nanostructures are different. Compared to TiO_2p/ZnP, we observe faster ET not only for ZnOr/TiO_2/ZnP but also for ZnOr/ZnP. This is a clear indication that the semiconductor nanostructure has a strong influence on the ET rate. The TiO_2 nanoparticle film is randomly packed and has grain boundaries and therefore electronic states differ from the bulk at every nanoparticle interface. On the contrary, one-dimensional ZnOr are single crystals with wurtzite structure and can provide a direct pathway for electron transport along the nanorods unlike the film of nanoparticles. Looking at only samples based on nanorods (ZnOr/ZnP and ZnOr/TiO_2/ZnP), TiO_2 enhances the ET rate. A 5 nm layer of TiO_2 may be too thin to have well defined crystal structure but is thick enough to change the electronic structure of the ZnOr surface.

The faster ET for TiO_2 than for ZnO can be attributed to differences in conduction band electronic structures of TiO_2 and ZnO [24,25]. Although the band gaps of bulk ZnO and TiO_2 are very close to each other, TiO_2 has higher density of states than ZnO. This definitely is one reason for the faster ET rate, although in the case of sensitized ZnO nanorods and nanoparticle films the role of conduction band electronic structure in ET reaction rate has been under discussion [26,27]. It has been suggested that ET proceeds via intermediate state at ZnO–sensitizer interface and this state is a major factor determining the ET rate. The intermediate state is related to ZnO properties because no stepwise ET is observed for the reference TiO_2 samples but its origin is still under intense study [26,27]. Moreover, it is known that the ET at ZnP–semiconductor interface takes place through the space and is sensitive to the molecule arrangement on the surface and in particular to the tilt angle of ZnP [7,8,28]. The surfaces of the semiconductors are heterogeneous and despite similar sensitizing conditions, variation in tilt angles as well as different types of porphyrin aggregates are possible. So far, the effect of these factors on the ET remain unclear since experimental determination of exact molecular organization on semiconductor surface is extremely challenging task [8].

Although TiO_2 layer on ZnOr increases the ET rate, only a small difference in the charge recombination rate between the ZnOr/ZnP and ZnOr/TiO_2/ZnP is observed. Though the calculated longer lifetimes are somewhat different for these samples there is no visible difference in the decay profiles (Figure 5). The TiO_2 layer decreases slightly amplitude of ~50 ps decay component. One reason for this can be that the conductivity of the ZnOr core is higher than TiO_2 shell and the energy level of the conduction band of ZnO is slightly lower than that of TiO_2 [15]. Therefore photoinjected electrons in ZnOr/TiO_2/dye structures move across the TiO_2 layer into ZnOr and the recombination rate is mainly determined by ZnOr. Among all measured samples, the charge recombination is slowest in TiO_2p/ZnP. One possible explanation can be that the bulk carrier mobility of ZnO and TiO_2 contributes to the rate of charge recombination – the faster charge migration in ZnO makes charge recombination faster. The latter should not have a negative effect on the solar cell performance, since the higher carrier mobility is also beneficial for the efficient charge transport to the external circuit.

Table 2
Lifetimes and amplitudes of decay components obtained from transient absorption decays. τ_1, formation of porphyrin radical cation; τ_2 and τ_3, two decay time constants.

Substrate	τ_1 rise	τ_2 decay	τ_3 decay
ZnOr	0.3 ps	50 ps (60%)	2.3 ns (40%)
ZnOr/TiO_2	<0.2 ps, unresolved	50 ps (50%)	3.1 ns (50%)
ZnOr/Al_2O_3	Not formed	50 ps (60%)	2.5 ns (40%)
TiO_2p	0.9 ps	84 ps (20%)	>2 ns (80%)

4. Conclusions

For both ZnOr/ZnP and ZnOr/TiO_2/ZnP interfaces the ET is efficient and fast, being faster than that at the interface of TiO_2p/ZnP. A 5 nm thick TiO_2 shell on ZnOr modifies the surface electronic properties thus enabling sub-ps (<0.2 ps) ET reaction. The transient absorption measurements revealed only minor differences in the charge recombination rate between the ZnOr based samples but a clear difference is found in DSSC experiments. TiO_2 shell decreases the charge recombination as indicated by the increased open circuit voltage of the cell.

Acknowledgments

H.H. is grateful to doctoral program of the President of the Tampere University of Technology for the financial support. H.I., N.T., H.L., and H.H. thank Strategic Japanese-Finish Cooperative Program (JST, Tekes, and AF). The authors are grateful for Optoelectronics Research Centre (Tampere University of Technology) for SEM facilities. We also acknowledge the provision of ALD facilities by Aalto University at Micronova Nanofabrication Centre.

Appendix A. Supplementary data

Supplementary data associated with this article can be found, in the online version, at http://dx.doi.org/10.1016/j.cplett.2013.11.028.

References

[1] J.A. Anta, E. Guillén, R. Tena-Zaera, J. Phys. Chem. C 116 (2012) 11413.
[2] A. Hagfeldt, G. Boschloo, L. Sun, L. Kloo, H. Pettersson, Chem. Rev. 110 (2010) 6595.
[3] Q. Zhang, C.S. Dandeneau, X. Zhou, G. Cao, Adv. Mater. 21 (2009) 4087.
[4] A. Listorti, B. O'Regan, J.R. Durrant, Chem. Mater. 23 (2011) 3381.
[5] O.V. Prezhdo, W.R. Duncan, V.V. Prezhdo, Prog. Surf. Sci. 84 (2009) 30.
[6] A.S. Hart, C.B. KC, H.B. Gobeze, L.R. Sequeira, F. D'Souza, ACS Appl. Mater. Interfaces 5 (2013) 5314.
[7] H. Imahori et al., J. Phys. Chem. A 115 (2011) 3679.
[8] S. Ye et al., J. Phys. Chem. C 117 (2013) 6066.
[9] H. Imahori, S. Hayashi, H. Hayashi, A. Oguro, S. Eu, T. Umeyama, Y. Matano, J. Phys. Chem. C 113 (2009) 18406.
[10] H. Imahori et al., J. Phys. Chem. C 114 (2010) 10656.
[11] H. Imahori et al., Langmuir 22 (2006) 11405.
[12] T. Ling, J.-G. Song, X.-Y. Chen, J. Yang, S.-Z. Qiao, X.-W. Du, J. Alloys Compd. 546 (2013) 307.
[13] M. McCune, W. Zhang, Y. Deng, Nano Lett. 12 (2012) 3656.
[14] O. Lupan, V.M. Guérin, I.M. Tiginyanu, V.V. Ursaki, L. Chow, H. Heinrich, T. Pauporté, J. Photochem. Photobiol., A 211 (2010) 65.
[15] M. Law, L.M. Greene, A. Radenovic, T. Kuykendall, J. Liphardt, P.J. Yang, J. Phys. Chem. B 110 (2006) 22652.
[16] M. Liu, C.-Y. Nam, C.T. Black, J. Kamcev, L. Zhang, J. Phys. Chem. C 117 (2013) 13396.
[17] A.K. Chandiran, P. Comte, R. Humphry-Baker, F. Kessler, C. Yi, M.K. Nazeeruddin, M. Grätzel, Adv. Funct. Mater. 23 (2013) 2775.
[18] V.O. Williams, N.C. Jeong, C. Prasittichai, O.K. Farha, M.J. Pellin, J.T. Hupp, ACS Nano 6 (2012) 6185.
[19] H. Saarenpää et al., J. Phys. Chem. C 116 (2012) 2336.
[20] R.J. Ellingson, J.L. Blackburn, J. Nedeljkovic, G. Rumbles, M. Jones, H. Fu, A.J. Nozik, J. Phys. Rev. B 67 (2003) 075308.
[21] M.K. Nazeeruddin, R. Humphry-Baker, D.L. Officer, W.M. Campbell, A.K. Burrell, M. Grätzel, Langmuir 20 (2004) 6514.
[22] J. Rochford, E. Galoppini, Langmuir 24 (2008) 5366.
[23] Z. Gasyna, W.R. Browett, M.J. Stillman, Inorg. Chem. 24 (1985) 2440.
[24] J.B. Asbury, E. Hao, Y. Wang, H.N. Ghosh, T.J. Lian, J. Phys. Chem. B. 105 (2001) 4545.
[25] V. Thavasi, V. Renugopalakrishnan, R. Jose, S. Ramakrishna, Mater. Sci. Eng. R 63 (2009) 81.
[26] H. Němec et al., Phys. Rev. Lett. 104 (2010) 197401.
[27] C. Strothkämper, A.F. Bartelt, P. Sippel, T. Hannappel, R. Schuetz, R. Eichberger, J. Phys. Chem. C 117 (2013) 17901.
[28] M. Niskanen, M. Kuisma, O. Cramariuc, V. Golovanov, T.I. Hukka, N. Tkachenko, T.T. Rantala, Phys. Chem. Chem. Phys. 15 (2013) 17408.

SUPPORTING INFORMATION

Photo-induced electron transfer at nanostructured semiconductor-zinc porphyrin interface

*Hanna Saarenpää, Alexander Pyymaki Perros, Pasi Myllyperkiö, Kei Kurotobi, Harri Lipsanen, Hiroshi Imahori, Helge Lemmetyinen, and Nikolai V. Tkachenko**

*Corresponding author:

E-mail: hanna.hakola@tut.fi

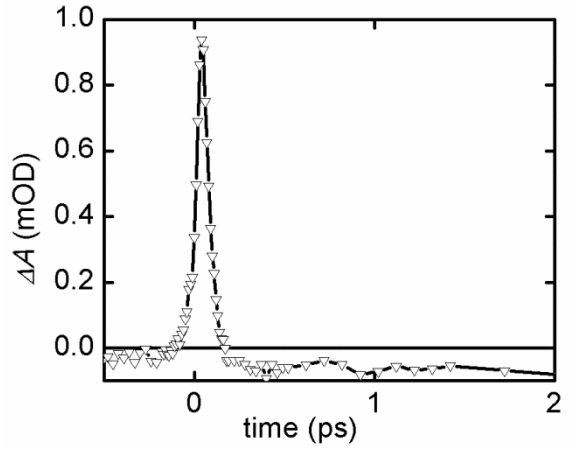

Figure S1. Transient absorption response of ZnOr substrate.

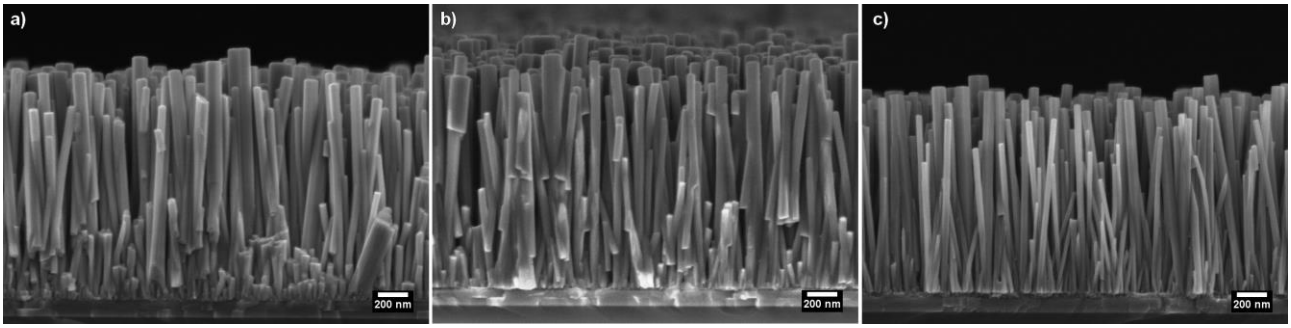

Figure S2. SEM images of ZnOr/Al_2O_3 5 nm (a), ZnOr/TiO_2 5 nm (b) and ZnOr (c) on ITO substrates. Considering the variation in diameters of ZnOr and the SEM resolution, the 5 nm thick layer of ZnO, Al_2O_3, or TiO_2 cannot be resolved from the ZnOr core.

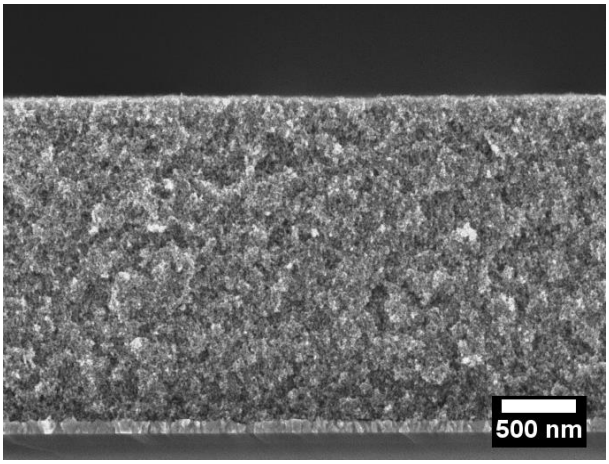

Figure S3. Cross-section SEM image of TiO_2 nanoparticle film.

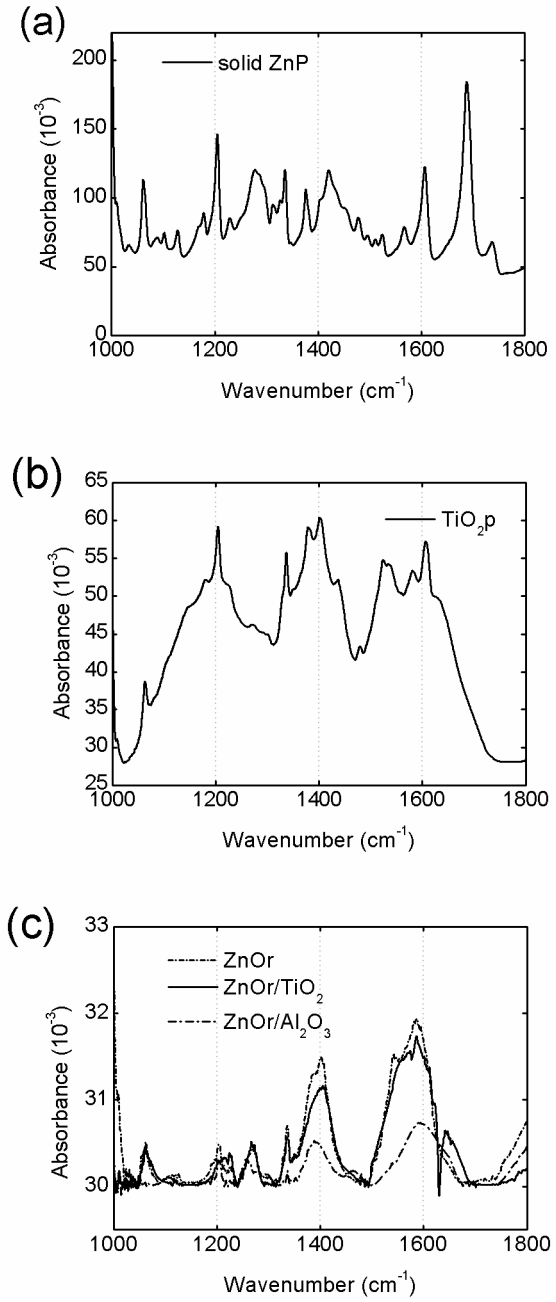

Figure S4. FT-IR-ATR spectra of (a) ZnP powder, (b) TiO_2p/ZnP and (c) ZnOr/Al_2O_3/ZnP (dash dot), ZnOr/ZnP (short dot), and ZnOr/TiO_2/ZnP (solid).

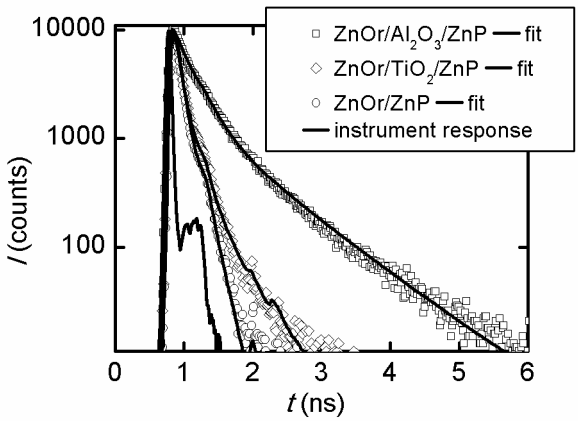

Figure S5. TCSPC decays of ZnOr/Al_2O_3/ZnP (square), ZnOr/ZnP (circle), and ZnOr/TiO_2/ZnP (diamond). Excitation and monitoring wavelengths were 405 nm and 605 nm, respectively.

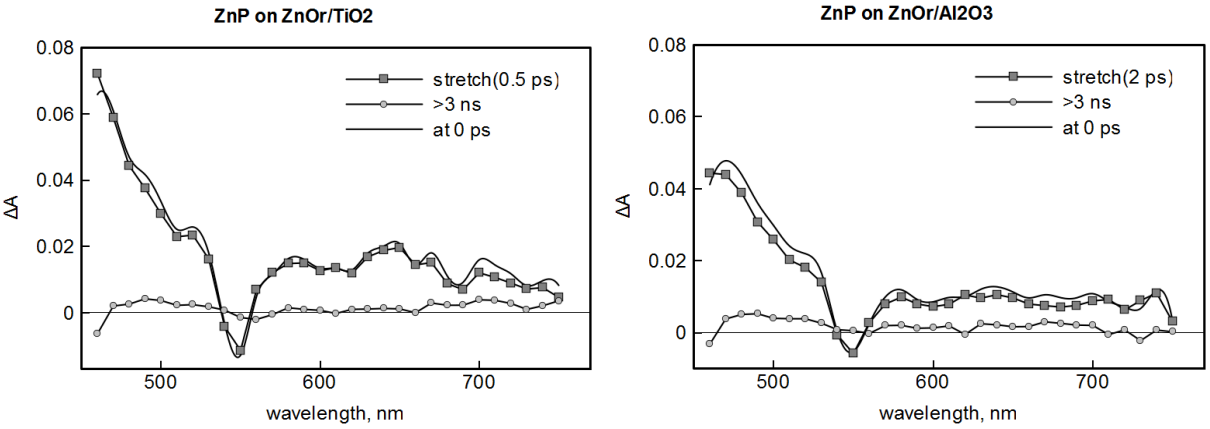

Figure S6. Decay component spectra of ZnP SAM on ZnOr/TiO_2 5 nm (left figure) and ZnOr/Al_2O_3 5 nm (right figure). The component lifetimes are indicated in the plots. The black solid lines present the time resolved spectra right after the excitation (at 0 ps). The details of the measurement system are found elsewhere*

*H. Lehtivuori, A. Efimov, H. Lemmetyinen, N.V. Tkachenko, Chem. Phys. Lett 437 (2007) 238-242.

IV

PHOTOINDUCED CHARGE TRANSFER THROUGH ZINC PHTALOCYANINE MONOLAYER ON ZINC OXIDE

by

Hanna Hakola, Essi Sariola-Leikas, Alexander Efimov and Nikolai V. Tkachenko, 2016

The Journal of Physical Chemistry C vol.120, 7044-7051

THE JOURNAL OF PHYSICAL CHEMISTRY C

Article

pubs.acs.org/JPCC

Effect of Hole Transporting Material on Charge Transfer Processes in Zinc Phthalocyanine Sensitized ZnO Nanorods

Hanna Hakola, Essi Sariola-Leikas, Alexander Efimov, and Nikolai V. Tkachenko*

Department of Chemistry and Bioengineering, Tampere University of Technology, P.O. Box 541, 33101 Tampere, Finland

Supporting Information

ABSTRACT: The photoinduced electron transfer processes were studied for hybrid systems consisting of self-assembled monolayer of zinc phthalocyanine (ZnPc) assembled on ZnO nanorods and a film of organic hole transporting material (HTM) atop. Polythiophene (P3HT) or Spiro-OMeTAD were used as HTM. The study was carried out by ultrafast transient absorption spectroscopy technique with selective excitation of ZnPc at 680 nm or P3HT at 500 nm. Data analysis revealed that photoexcitation of ZnPc in the structure ZnO|ZnPc|P3HT results in a fast (1.8 ps) electron transfer from ZnPc to ZnO, which is followed by a hole transfer from the ZnPc cation to P3HT roughly in 30 ps. However, in the case of ZnO|ZnPc|Spiro-OMeTAD structure, the primary reaction upon excitation of ZnPc is a fast (0.5 ps) hole transfer from ZnPc to Spiro-OMeTAD, and the second step is electron injection from the ZnPc anion to ZnO in roughly 120 ps. Thus, we demonstrate two structurally very similar hybrid architectures that implement two different mechanisms for photoinduced charge separation found in dye-sensitized or in organic solar cells.

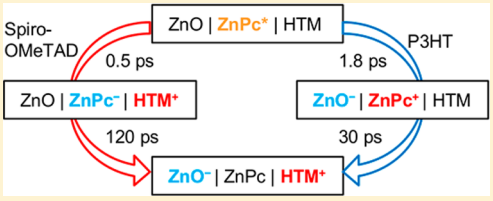

INTRODUCTION

Hybrid nanostructures consisting of inorganic and organic materials are under intense study due to their wide application range in photonics and molecular electronics.[1−3] To design new devices with specific photofunctions it is important to shed light on mechanism of light induced charge generation and transport in specifically designed organic and hybrid organic-semiconductor systems.[4] One example of such a device is dye-sensitized solar cell (DSSC). Typically photoinduced electron transfer (ET) reactions in these devices are controlled by the dye. More specifically, by selecting the chromophore with proper redox properties and suitable anchor group the desired photoresponse can be achieved. This type of the ET reactions at the inorganic−organic interface has been well-studied by advanced spectroscopy and $J-V$ characterization methods for a range of organic chromophores assembled on TiO_2 or ZnO nanostructures.[5−8] To get use of the charge separation (CS) at the organic-semiconductor interface, the charge has to be collected from the organic layer and delivered to an electrode. In a "classic" DSSC, this is a function of electrolyte filling, but new solid state devices utilize hole transporting materials (HTM) for this purpose. One of the most widely used HTM is Spiro-OMeTAD,[3] which was first described by Bach et al.[9] A hole transporting layer is deposited on top of an organic sensitizer, thus, adding an organic−organic interface to the system. Charge transfer processes in TiO_2-dye-Spiro-OMeTAD structures have been studied with ruthenium,[10,11] indolene,[12] and perylene[13−15] sensitizers, as well as in perovskite-based solar cells.[16] Another common HTM is P3HT. It was first used as hole conductor in bulk heterojunction solar cells,[17,18] but has also been studied in solid-state dye sensitized solar cells recently.[19] Photodynamics at dye−P3HT interface was studied using indolene[20] and phthalocyanine[21] derivatives as sensitizers for samples prepared on TiO_2 nanoparticle films. However, to the best of our knowledge, only a few studies were undertaken to compare these two HTM, and even these studies compare the final solar cell performance,[22] leaving mechanism of photoinduced charge separation unanswered.

Investigation of primary mechanisms of photoinduced charge transfer in three-component structures such as semiconductor-dye sensitizer-HTM is a challenging task, since a few reactions can compete with each other, and potentially, the reactions can be initiated by exciting both the dye sensitizer and the HTM, as is in the case of P3HT used as HTM. One of the aims of this study is to find such systems when the reaction can be initiated selectively at a particular component of the structure. Therefore, zinc phtalocyanine (ZnPc) derivative was selected as dye sensitizer as it has distinct band close to 700 nm and can be excited selectively. At the same time, ZnPc has almost no absorption around 500 nm, which makes possible selective photoexcitation of P3HT if required. Phthalocyanines were widely used as sensitizers in DSSC,[23] though their drawbacks are relatively high aggregation tendency, which reduces ET efficiency, and relatively narrow absorption band, which leads to a poor spectrum coverage.[24]

Another challenge of this study is to ensure compatible conditions for the formation of the HTM layer on top of semiconductor with dye monolayer for such different compounds as Spiro-OMeTAD and P3HT. Since the method to study the primary photoreactions is ultrafast transient absorption spectroscopy, we cannot use flat layered architec-

Received: February 16, 2016
Published: March 22, 2016

DOI: 10.1021/acs.jpcc.6b01583
J. Phys. Chem. C 2016, 120, 7044−7051

tures, as the dye monolayer has insufficient absorption to be studied by this technique. At the same time, typically used TiO_2 nanoparticle films have very small pore sizes; thus, it is difficult to ensure complete coverage of the dye monolayer by P3HT. Therefore, we have used ZnO nanorod films as model semiconductor surfaces. Similar to TiO_2, ZnO nanorods are employed in the design of DSSC, though they show lower overall conversion efficiency.[25−27] The specific surface area of ZnO nanorods is much smaller than that of TiO_2 nanoparticle films but sufficient to conduct the study. As semiconductor, ZnO has conduction/valence band energies very similar to TiO_2 and its activity as electron acceptor in DSSC is also compatible to that of TiO_2.[28,29]

EXPERIMENTAL SECTION

All commercially available reagents and solvents purchased from Sigma-Aldrich Co., TCI Europe, and VWR were used without further purifications unless otherwise mentioned. The chemical structure of zinc 4-(1,15,22-trimesitylphthalocyanine-8-yl)benzoic acid (ZnPc) is shown in Figure 1, and the synthetic route is described in Supporting Information (SI).

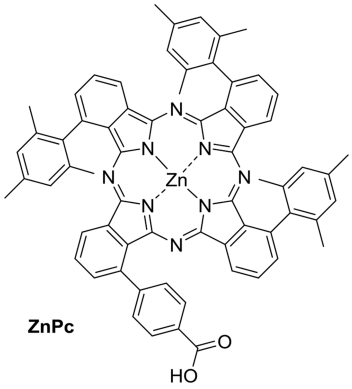

Figure 1. Chemical structure of ZnPc.

Solid Sample Preparation. ZnO nanorods were fabricated by a two-step hydrothermal method: formation of seed layers on flat substrates and the actual growth of the nanorods. ITO-coated glass substrates were cleaned by sonication in 2% Hellmanex, water, and 2-propanol, 15 min in each solvent, and dried in the oven at 150 °C for 30 min. Seed layer was formed by using zinc acetate dehydrate (0.23 mol/L) dissolved in a mixture of 2-methoxyethanol ($CH_3OCH_2CH_2OH$) and ethanolamine ($NH_2CH_2CH_2OH$) (96:4). Solution was stirred at 60 °C for 2 h and cooled down to room temperature. After overnight aging of the solution, it was spin-coated on UV ozone treated (15 min) ITO surface (1500 rpm, 60 s), followed by annealing in air at 350 °C for 20 min. The hydrothermal growth (85 °C) was carried out in a sealed beaker by immersing the ITO|ZnO substrates active surface down into 0.02 mol/L aqueous solution of zinc nitrate ($Zn(NO_3)_2$, ≥99%) and hexamethylenetetramine ($C_6H_{12}N$, 99%) for 6 h. After the reaction, the samples were removed from the solution, rinsed with Milli-Q water, and dried in air at room temperature and finally annealed in air (300 °C, 30 min).

Prior deposition of ZnPc SAM on ZnO nanorods, the substrates were heated (150 °C, 30 min). After cooling down to room temperature, the plates were immersed into a solution of ZnPc (0.05 mmol/L) in butanol. After a 16 h reaction, the samples were rinsed and immersed in butanol for 5 min in order to remove residual ZnPc molecules.

P3HT (regioregular poly(3-hexyl thiophene-2,5-diyl, 2 g/L, Rieke Metals) was spin-coated (2000 rpm, 60 s) from a chlorobenzene solution. Spiro-OMeTAD (2,2′,7,7′-tetrakis-(*N*,*N*-di-4-methoxyphenylamino)-9,9′-spirobifluorene, Shenzhen Feiming Science and Technology Co., Ltd.) in anhydrous chlorobenzene (70 mg/mL) was spin-coated in the same way as P3HT. Samples were stored in nitrogen-filled vials at room temperature. The samples are denoted as ZnO|ZnPc, ZnO|ZnPc|P3HT, and ZnO|ZnPc|Spiro later in the text.

Characterization. The morphology of the ZnO nanorods was studied using field emission scanning electron microscope (FE-SEM, Carl Zeiss Ultra 55). Absorption spectra of the samples were measured by Shimadzu UV-360 spectrophotometer. A pump−probe setup used for transient absorption measurements was described elsewhere.[30] In brief, the samples were excited at 500 and 680 nm (Combination of Libra-F, Coherent Inc., and Topas C, LightConversion). The time-resolved spectra were recorded in three wavelength ranges 480−770, 850−1060, and 1140−1350 nm (ExciPro spectrometer, CDP Inc.). Overall, time resolution of the system was 150−200 fs. All measurements were carried out under a nitrogen atmosphere. Excitation energy density was roughly 30 $\mu J \cdot cm^{-1}$, which resulted in excitation efficiency <6% (estimated from the ground absorption bleaching).

The data analysis was carried out using homemade software (decfit), which allowed a global fit of transient absorption data to various decay models, with data convolution with the instrument response function and group velocity compensation.[30−32]

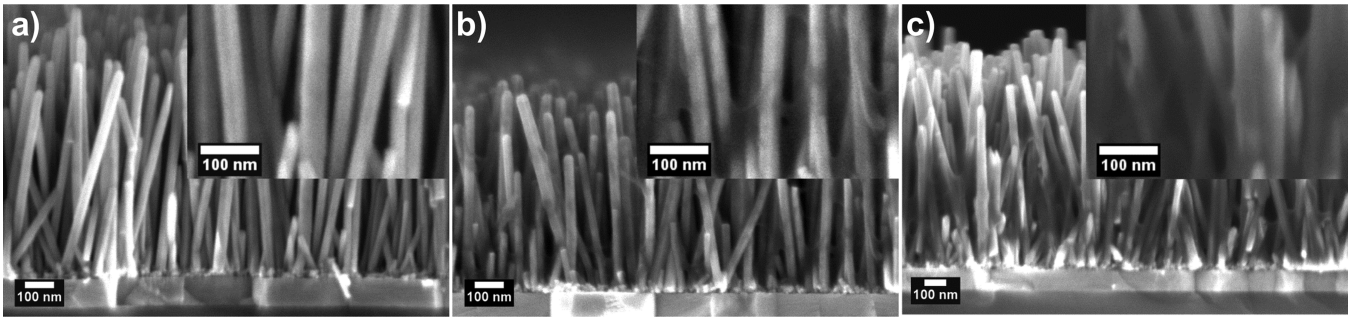

Figure 2. Cross section SEM images of (a) ZnO|ZnPc, (b) ZnO|ZnPc|P3HT, and (c) ZnO|ZnPcSpiro. Bigger magnifications of the same samples are shown in the figure insets.

DOI: 10.1021/acs.jpcc.6b01583
J. Phys. Chem. C 2016, 120, 7044−7051

RESULTS

Characterization of Hybrid Samples. SEM images of the ZnO|ZnPc, ZnO|ZnPc|P3HT, and ZnO|ZnPc|Spiro sample cross sections are shown in Figure 2. Hydrothermal growth of ZnO nanorods (ZnO) was used to prepare dense arrays of semiconductor nanorods aligned perpendicular to the supporting surface. After 6 h growth, the nanorods are approximately 700 nm long and have 30−40 nm diameter, which is in agreement with the previous studies.[33] The spatial resolution of the SEM used in this study is limited to 5−10 nm; thus, ZnPc SAM on ZnO cannot be distinguished. However, P3HT and Spiro-OMeTAD layers fill relatively large volumes and are seen in the images as gray areas around and between the ZnO. As a result, single nanorods are not seen in Figure 2b,c as clearly as in Figure 2a. SEM images illustrates that Spiro-OMeTAD infiltrates better to ZnO compared to P3HT. This is expected since it has lower molecular weight and spatial size than P3HT.[22] The corresponding images of the reference samples ZnO|P3HT and ZnO|Spiro can be found in SI (Figure S2). SEM images of the samples with and without ZnPc SAM look similar; thus, it was concluded that ZnPc SAM has no effect on the HTM infiltration. The same conclusion can be drawn from the absorption spectra shown later in the results.

The samples prepared for this study were optimized for the TA measurements, which require predominant coverage of ZnPc SAM by HTM, but complete filling of all the voids between the nanorods is not a prerequisite. In fact, one of the aims in preparing samples with P3HT was to minimize its amount so that it does not dominate those TA signals that are overlapping with ZnPc.

The absorption spectra of ZnPc butanol solution and the studied samples are shown in Figure 3. Absorption maximum of the ZnPc Q-band in butanol is at 679 nm. ZnPc SAM on ZnO has absorption maximum at 681 nm and spectrum is slightly broadened as compared to the solution spectrum. The bandwidths (fwhm) are 34 and 19 nm in SAM and in butanol, respectively. Such a small shift in absorption maximum position, and only a minor increase in the bandwidth indicate relatively low degree of aggregation of ZnPc in SAM.[7] The same conclusion can be drawn from other noticeable features of the absorption spectrum of ZnPc SAM. Minor Q-band at 610 nm is well preserved, and there is no typical aggregate shoulder at the red side of the main Q-band. These observations differ this ZnPc from other phthalocyanine derivatives used in dye sensitized solar cells, for example, from TT1, for which 3.52% power conversion efficiency was reported.[34]

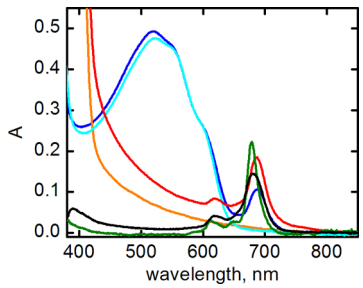

Figure 3. Absorption spectra of ZnPc in BuOH (green), ZnO|ZnPc (black), ZnO|P3HT (cyan), ZnO|ZnPc|P3HT (blue), ZnO|Spiro (orange), and ZnO|ZnPc|Spiro (red). Spectrum of ZnO has been subtracted from each film structure.

In general, absorbance of ZnPc SAM is at the expected level when compared to porphyrin SAMs on similar ZnO substrates.[33] Therefore, we expect reasonably complete coverage of ZnO surface by the SAM.

P3HT film has characteristic broad absorption in the range 400−620 nm, which is the dominating absorption of ZnO|P3HT and ZnO|ZnPc|P3HT samples (Figure 3). Shoulders at 550 and 600 nm can be attributed to vibrational transitions.[35] Spiro-OMeTAD film on ZnO is almost transparent, the main absorption band around 390 nm is seen as a sharp absorbance rise toward shorter wavelengths starting from 450 nm.[36] The spectra of ZnO|ZnPc|P3HT and ZnO|ZnPc|Spiro are almost sums of the spectra of its components, but ZnPc Q-band is red-shifted by 7 nm. The shift is an indication of the change in the environment of ZnPc SAM caused by the close contact to HTM. Despite of the red shift, the bandwidth of the ZnPc Q-band was not broadened but even a bit narrowed (30−32 nm) after deposition of HTM layers. This suggests relatively homogeneous coverage of ZnPc SAM by HTM, which does not leave detectable amount of ZnPc with the spectrum measured without HTM layer.

A small variation in the intensities of ZnPc absorption band can be attributed to a variation in length and density of nanorods, which have an effect on the effective surface area as was discussed in our previous study.[33]

Time-Resolved Absorption. TA measurements of ZnO|ZnPc were carried out with excitation at 680 nm. In principle, the ET from an excited ZnPc to ZnO is the first order reaction for each individual molecule and should follow exponential decay kinetics. The measured signal is cumulative response of large number ZnPc molecules in SAM on the ZnO surface and there is variation in local environment between ZnPcs. This converts exponential decay kinetics to a sum of exponents with time constants randomly distributed around some average value. A mathematical model to deal with the case was developed and successfully applied to analyze ET in molecular films,[31,32] and was used in this study as well. ZnO|ZnPc data was globally fitted with a model consisting of two distributed decays and the fit results are shown in Figure 4. A tentative interpretation is the electron injection from the photoexcited ZnPc to ZnO with 1.4 ps average time constant and the charge recombination with 850 ps average time constant. The average charge separation time constant agrees reasonably well with the ET time constant found for TT1 phthalocyanine on TiO_2 surface.[21] Within this interpretation, the spectrum of the singlet excited ZnPc is shown by the red dashed line and the spectrum of the ZnPc cation by the green line. The important spectral features to distinguish between the singlet excited state and

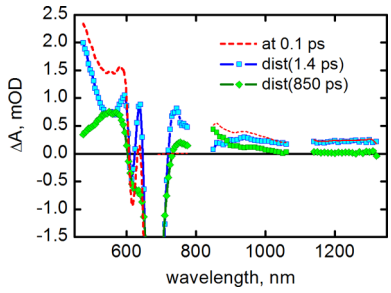

Figure 4. Decay component (line + symbol) and time-resolved (dashed line) spectra of ZnO|ZnPc. Excitation wavelength was 680 nm. See text for details.

DOI: 10.1021/acs.jpcc.6b01583
J. Phys. Chem. C 2016, 120, 7044−7051

ZnPc cation are the featureless excited state absorption in the ranges 470−600 and 900−1300 nm and the bands located at 550 nm and 850 corresponding to ZnPc cation.[37,38]

Time-resolved TA spectra of ZnO|P3HT were obtained with excitation at 500 nm and are shown in Figure 5. Except of very

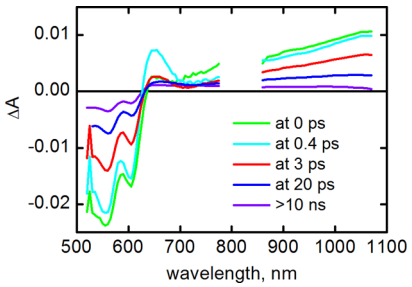

Figure 5. Calculated time-resolved spectra of ZnO|P3HT. Excitation wavelength was 500 nm.

fast subpicosecond spectral perturbations in the 600−650 nm range, the main features of the TA response is bleaching of the ground state absorption of P3HT at <630 nm and smoothly rising absorbance in the NIR region (850−1050 nm). To fit the data with reasonable accuracy (reasonably small sigma-value and noncorrelated residuals) a five exponential model had to be used, which gave time constants 0.2, 0.8, 7, 100, and 15000 ps with compatibly strong contribution to the decay and rather minor differences in corresponding decay component spectra. Considering a very wide divergence of the time constants, the results characterization by a single (average) lifetime is rather meaningless.

The TA response of ZnO|ZnPc|P3HT to excitation at 680 nm (selective excitation of ZnPc) is more complex, but can be understood at qualitative level by comparing responses at different wavelengths and time-resolved spectra at different delay times, as presented in Figure 6. Shortly after excitation the TA spectrum is dominated by the response of ZnPc, the singlet excited state or cation (Figure 4 and 2D map shown in SI, Figure S3). A distinct feature of the TA response at longer delay time is the recovery of the ZnPc ground state absorption (decay at 707 nm) that coincides with the bleaching development of P3HT ground state (decay at 551 nm and negative band at 500−600 nm at delays >10 ps).

Since P3HT is not excited directly, the only possibility how it gets involved is electronic interaction between the ZnPc layer and P3HT. The energy transfer can be excluded from the very beginning since excited state energy of P3HT is much higher than that of ZnPc (and that of the excitation light). The interaction cannot be just an electron transfer between the photoexcited ZnPc and P3HT since depletion of the P3HT ground state coincides with recovery of the ZnPc ground state. Thus, the most reasonable and simple explanation is two step electron transfer as denoted in eq 1.

$$\begin{aligned} \text{ZnO|ZnPc*|P3HT} &\rightarrow \text{ZnO}^{-}\text{|ZnPc}^{+}\text{|P3HT} \\ &\rightarrow \text{ZnO}^{-}\text{|ZnPc|P3HT}^{+} \end{aligned} \quad (1)$$

The second reaction step is hole transfer form ZnPc cation to P3HT. According to Figure 6b, this reaction takes place in the 2−2000 ps time domain.

Based on this reaction scheme the TA data were fitted globally using a model consisting of a picosecond exponent to account for the primary electron transfer from ZnPc singlet

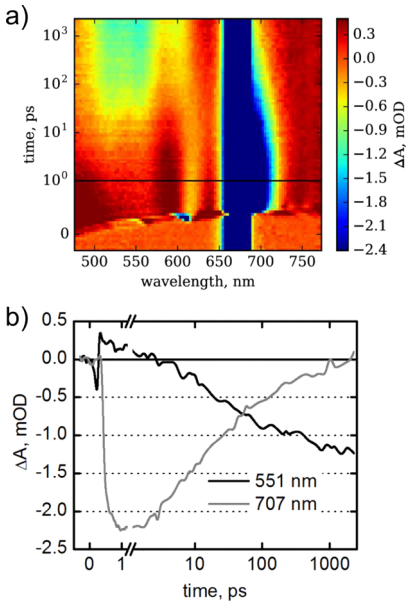

Figure 6. 2D map of ZnO|ZnPc|P3HT TA signals (a) and TA decay curves of the same sample monitored at 551 and 707 nm (b). The time scales are linear until 1 ps and logarithmic after 1 ps. Excitation wavelength was 680 nm (vertical blue line in plot (a) in the range 655−680 nm is the trace of scattered excitation beam).

excited state, a distributed decay to account for the hole transfer from $ZnPc^{+}$ to P3HT, and a long-lived exponent accounting for the long-lived holes in $P3HT^{+}$. Results of the fit are presented in Figure 7. The obtained exponential lifetime (1.8 ps) for the

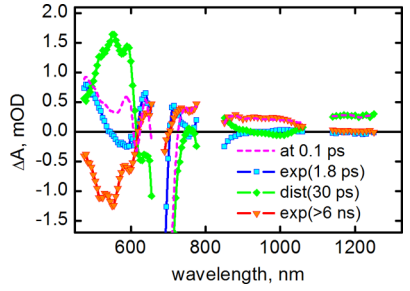

Figure 7. TA decay component spectra (lines with symbols) and time-resolved spectrum at 0.1 ps after excitation (dashed line) of ZnO|ZnPc|P3HT. Excitation wavelength was 680 nm.

$\text{ZnO|ZnPc*} \rightarrow \text{ZnO}^{-}\text{|ZnPc}^{+}$ reaction correlates well with that obtained for the sample without P3HT layer (1.4 ps). The corresponding component spectrum is also reasonably close to that obtained for the ET in ZnO|ZnPc sample. The hole transfer is much faster than the charge recombination at the ZnO|ZnPc interface (30 ps vs 850 ps), which means that an efficient hole transfer can be expected in this system.

Results of global fitting of the TA data of ZnO|ZnPc|Spiro are presented in Figure 8. The minimum number of exponential components to achieve a reasonable data approximation was five (four are shown in the figure and the fifth is associated with 50 fs time constant and was needed to correct the response function). Reference sample ZnO|Spiro was also measured but no signal was detected with 680 nm excitation.

The essential features of the ZnO|ZnPc|Spiro TA spectra are (1) bands at 575 and 960 nm, which are formed and decayed

DOI: 10.1021/acs.jpcc.6b01583
J. Phys. Chem. C 2016, 120, 7044−7051

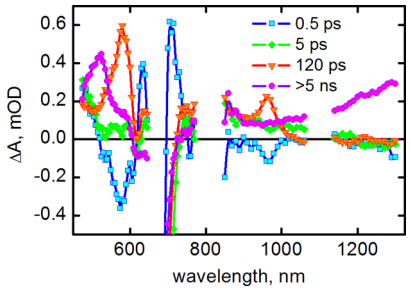

Figure 8. TA decay component spectra of ZnO|ZnPc|Spiro. Excitation wavelength was 680 nm.

with 0.5 and 120 ps time constants, respectively, (2) a component with time constant >5 ns, which has a band at 525 nm, and (3) a rising absorption at >1100 nm. The bands at 525, 575, and 960 nm are not seen right after excitation (at 0.1 ps, see time-resolved spectra in SI). The bands at 575 and 960 nm become clear at a few picosecond delay time. The band at 525 nm can be also observed already at 2 ps delay but it becomes much more pronounced after decay of the bands at 570 and 960 nm. The most reasonable assignment of the bands at 575 and 960 nm is to ZnPc anion[39] and of the bands at 525 nm and the broad band at 1150−1350 nm is to Spiro-OMeTAD cation.[9,13,16] Equation 2 describes the reaction steps.

$$\text{ZnO|ZnPc*|Spiro} \rightarrow \text{ZnO|ZnPc}^{-}\text{|Spiro}^{+} \rightarrow \text{ZnO}^{-}\text{|ZnPc|Spiro}^{+} \quad (2)$$

The primary CS takes place between the excited ZnPc* and Spiro-OMeTAD with roughly 0.5 ps time constant, and the following electron injection from ZnPc anion to ZnO takes place with 120 ps time constant. The decay profiles at the key wavelengths are shown in Figure 9.

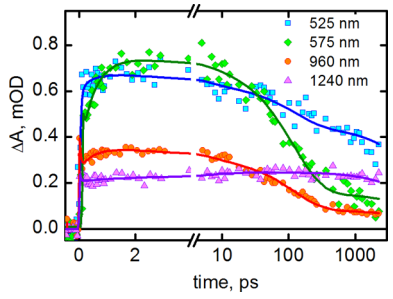

Figure 9. TA decay profiles of ZnO|ZnPc|Spiro at selected wavelengths.

The TA signals at 1240 and 525 nm originate mainly from Spiro-OMeTAD cation. At 525 nm the signal is not solely attributed to Spiro-OMeTAD cation, also ZnPc singlet excited state and ZnPc cation have contribution thus the faster decay at 525 nm than at 1240 nm is expected. ZnPc anion decay can be monitored at 575 and 960 nm which show similar relaxation rates. The difference in molar absorption coefficients between these two bands is mainly responsible for the smaller amplitude of the decay at 960 nm.[39]

According to the results obtained for ZnO|ZnPc, the electron transfer from the photoexcited ZnPc to ZnO takes place in the same time domain (1.4 ps, Figure 4). Therefore, one can expect a competing relaxation pathway to be

$$\text{ZnO|ZnPc*|Spiro} \rightarrow \text{ZnO}^{-}\text{|ZnPc}^{+}\text{|Spiro} \rightarrow \text{ZnO}^{-}\text{|ZnPc|Spiro}^{+} \quad (3)$$

In this case, the 5 ps time constant shown in Figure 8 (relatively minor component) can be attributed to the second reaction step ($\text{ZnPc}^{+}\text{|Spiro} \rightarrow \text{ZnPc|Spiro}^{+}$) and the time constant 0.5 ps is the total relaxation time of the singlet excited state (ZnPc*) via both channels, $\text{ZnPc*|Spiro} \rightarrow \text{ZnPc}^{-}\text{|Spiro}^{+}$ and $\text{ZnPc*|Spiro} \rightarrow \text{ZnO}^{-}\text{|ZnPc}^{+}$, respectively.

When the ZnO|ZnPc|P3HT sample is excited at 500 nm the P3HT is excited almost exclusively and TA response of this sample is almost identical to that of the sample without ZnPc SAM, as is illustrated in Figure 10. There is an exception in one particular spectrum range around 690 nm, which is absorption maximum of ZnPc. The decays monitored at 690 nm are shown in Figure 10c. It can be noticed that the negative absorption or bleaching of the ZnPc Q-band develops in a picoseconds delay time, but right after excitation, the transient absorption is positive confirming that excitation at 500 nm does not affect ZnPc chromophore.

Two possible explanations for the negative band around 690 nm are energy transfer,[21] $\text{ZnPc|P3HT*} \rightarrow \text{ZnPc*|P3HT}$, and electron transfer, $\text{ZnPc|P3HT*} \rightarrow \text{ZnPc}^{-}\text{|P3HT}^{+}$. In both cases a long distance CS state, $\text{ZnO}^{-}\text{|ZnPc|P3HT}^{+}$, is expected to be formed in few tens to a few hundred picoseconds time domain. Reaction scheme for the ZnPc excited state is shown by eq 1 and according to the measurements with direct excitation of ZnPc, this long distance CS state is formed with average time constant of 30 ps, which agrees well with the recovery of ZnPc bleaching (Figure 10c). If ZnPc anion is formed, the electron transfer from ZnPc^{-} to ZnO is expected to take place in 120 ps as was found in ZnO|ZnPc|Spiro sample. However, no sign of ZnPc^{-} (bands at 575 and 960 nm) was found in TA data obtained for ZnO|ZnPc|P3HT with excitation at 500 nm

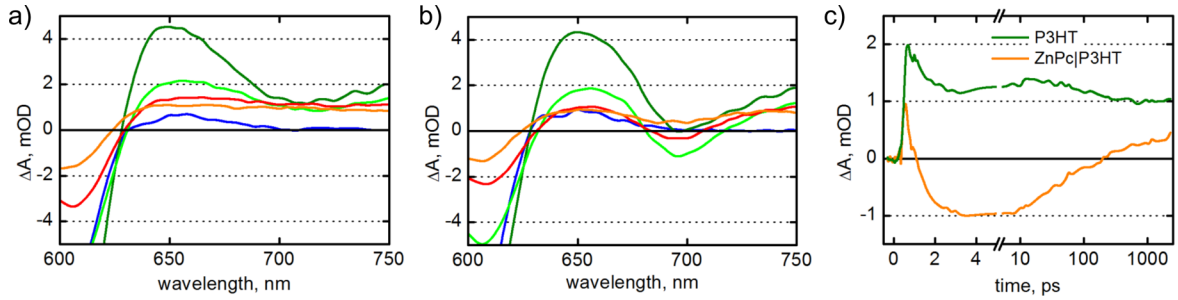

Figure 10. Time-resolved spectra of ZnO|P3HT (a) and ZnO|ZnPc|P3HT (b) at 0.2 ps (blue), at 1 ps (green), at 5 ps (light green), at 50 ps (red), and at 2 ns (orange) and TA decays monitored at 690 nm (c). The decay of ZnO|P3HT is indicated by the green line and ZnO|ZnPc|P3HT by orange line. Excitation wavelength was 500 nm.

DOI: 10.1021/acs.jpcc.6b01583
J. Phys. Chem. C 2016, 120, 7044−7051

(Figures 10 and S5). Therefore, the energy transfer and charge transfer following eq 1 is proposed as the main reaction pathway for the CS in this case, though not all excited P3HT are relaxing by the energy transfer to ZnPc, as will be discussed later.

DISCUSSION

In recent studies of semiconductor-dye-HTM systems, two types of the charge generation have been observed as schematically illustrated in Figure 11.[15] In the first type of reactions (type 1), excitation of the dye leads to an ET to semiconductor from the dye layer, which is followed by the hole transfer to the HTM. In the second case (type 2), the first charge transfer step is ET from HTM to the dye followed by ET from the dye (anion state) to the semiconductor.

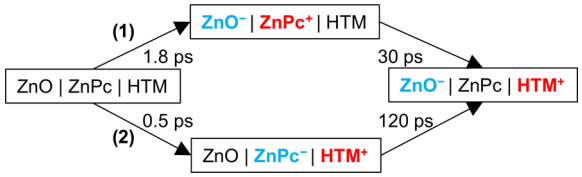

Figure 11. Schematic illustration of the main charge generation mechanism in the studied system. HTM corresponds to hole transporting material. The measured time constants for each reaction steps are shown for HTM = P3HT (top path, type 1) and HTM = Spiro-OMeTAD (bottom path, type 2).

In our ZnO|ZnPc|HTM system the type of charge generation is determined by the HTM. The time-resolved spectroscopy study shows that the pathway of charge transfer in ZnO|ZnPc|P3HT is type 1 independent of which chromophore is excited, ZnPc or P3HT. It needs to be noted that the samples were not optimized for efficient ET, when P3HT is excited. The exciton diffusion length in P3HT was estimated to be around 5 nm,[40−43] which means that in a thicker layer of P3HT the probability of exciton to reach ZnPc|P3HT interface is relatively small.

When P3HT layer is replaced by Spiro-OMeTAD, the ET reaction is converted to type 2. TA spectrum of ZnO|ZnPc|Spiro shows clear bands of the ZnPc anion and Spiro-OMeTAD cation shortly after the excitation. Previously studied TiO_2-dye-Spiro-OMeTAD systems have also demonstrated type 2 ET reaction.[12,15,16]

An interesting question to discuss is the reason for so different behavior of the two types of samples. If ZnPc is excited, for the hole transfer reaction to be thermodynamically possible, the HOMO energy of hole transporting material must be higher than that of ZnPc HOMO. The reported energies of P3HT HOMO are in the range −4.8 to −5.2 eV,[3,19,44] and for Spiro-OMeTAD are −4.9 to −5.1 eV.[2,3,45] Apparently both values are higher than HOMO level of ZnPc, but the values are very close to each other to explain the different reaction pathway. Though one needs to be cautious with this estimation since the conditions of measuring HOMO/LUMO energies of the compounds and molecular arrangements in studied samples are very different, and actual HOMO/LUMO levels in the samples may vary substantially form those measured in solution. However, the distance between ZnPc and HTM is another factor important for the efficient ET and it can be different in the case of P3HT and Spiro-OMeTAD. Spiro-OMeTAD is a relatively small molecule and it is likely to enter all possible voids in ZnO|ZnPc nanostructure. In the contrary, P3HT is a polymer with relatively long alkyl chains surrounding the hole conducting polythiophene core, and it is expected to form a layer on top of ZnPc SAM with alkyl chains separating ZnPc and polythiophene core. If this is correct, the short intermolecular distance in ZnPc|Spiro interface is the reason for primary ET at the organic−organic interface. The measured time constant for this ET is 0.5 ps. The ET reaction at ZnPc|P3HT interface is thermodynamically possible but due to longer distances it is much slower (30 ps) than the electron transfer from the excited ZnPc to ZnO (1.8 ps). In fact, the driving force for the hole transfer from P3HT is the electron vacancy at HOMO level of ZnPc, which still remains after ET from ZnPc to ZnO, and this reaction successfully proceeds with time constant 30 ps. Although the distance seems to be very reasonable explanation, there are no experimental evidence for the different distances between ZnPc and Spiro-OMeTAD or P3HT. Furthermore, addition of either Spiro-OMeTAD or P3HT results in almost the same shift of ZnPc Q-band position which was interpreted as penetration of HTM into ZnPc SAM, though in the case of P3HT the effect may be caused by alkyl chains penetration but not the polythiophene core.

The electron injection from ZnPc to ZnO is energetically favorable when an electron is promoted to LUMO of ZnPc. Formally speaking this can be the excited state, ZnPc*, or anion, $ZnPc^-$. Our study shows that the time constants for these two reactions, ZnO|ZnPc* → ZnO|$ZnPc^+$, and ZnO|$ZnPc^-$ → ZnO^-|ZnPc, are very different, 1.8 and 120 ps, respectively. Most probably Coulomb interaction with the cation in Spiro-OMeTAD side changes the energy balance and slows down the ET in the latter case.

Both studied structures, ZnO|ZnPc|P3HT and ZnO|ZnPc|Spiro, are promising architectures for real applications, for example, solid state solar cells. Having this application in mind, ZnO nanorods can be considered as an ideal template to build interpenetrating network of electron and hole conducting materials,[22−24] in which case, the array of ZnO nanorods is the required electron conducting material delivering the electrons to an electrode. Although in order to build a device with reasonable efficiency the surface area of ZnO nanorods should be optimized and the infiltration of the HTM material into ZnO nanostructure should be provided to the level when no ZnO nanorods are pointing toward the metal electrode.

CONCLUSIONS

The role of HTM in charge transfer reactions in three component systems consisting of ZnO, ZnPc SAM, and either P3HT or Spiro-OMeTAD was studied. For both sample architectures, the energy gradient is favorable for a fast photoinduced charge separation across the middle ZnPc layer. A cascade of reactions triggered by light absorbed in organic layers results in electron localized in ZnO and hole in the top HTM layer within few hundreds of picoseconds. However, sequence of the reactions is different and determined by the HTM.

For the structure with P3HT the sequence of reactions is typical for that in dye sensitized solar cells, when the primary charge separation takes place at semiconductor−organic interface, ZnO|ZnPc in our case. With Spiro-OMeTAD layer on top of the structure, the primary charge separation is at the organic−organic interface, which is ZnPc|Spiro in this case. This sequence of ET reactions is typically found in organic solar cells. Our study shows that a hybrid structure where the

DOI: 10.1021/acs.jpcc.6b01583
J. Phys. Chem. C 2016, 120, 7044−7051

operation can be switched from DSSC type to organic solar cell can be prepared by replacing a single component. This opens a possibility to design devices combining the best properties of both types of solar cell architectures.

■ ASSOCIATED CONTENT

Supporting Information

The Supporting Information is available free of charge on the ACS Publications website at DOI: 10.1021/acs.jpcc.6b01583.

Detailed description synthesis of ZnPc, additional SEM images, TA data and fits (PDF).

■ AUTHOR INFORMATION

Corresponding Author

*E-mail: nikolai.tkachenko@tut.fi.

Notes

The authors declare no competing financial interest.

■ ACKNOWLEDGMENTS

H.H. is grateful to the Academy of Finland (No. 263486, 270308) and to the doctoral programme in Engineering and Natural Sciences in Tampere University of Technology.

■ ABBREVIATIONS

DSSC, dye-sensitized solar cell; ET, electron transfer; fwhm, full width half-maximum; HTM, hole transporting material; ITO, indium tin oxide; *J*−*V*, current−voltage; P3HT, poly(3-hexyl thiophene-2,5-diyl); ZnPc, zinc phthalocyanine; ZnO, zinc oxide; SAM self-assembled monolayer; SEM, scanning electron microscope; Spiro-OMeTAD, 2,2′,7,7′-tetrakis(*N*,*N*-di-4-methoxyphenylamino)-9,9′-spirobifluorene; TA, transient absorption

■ REFERENCES

(1) Ragoussi, M.-E.; Torres, T. New Generation Solar Cells: Concepts, Trends and Perspectives. *Chem. Commun.* **2015**, *51*, 3957−3972.

(2) Game, O.; Singh, U.; Kumari, T.; Banpurkar, A.; Ogale, S. ZnO(N)-Spiro-MeOTAD Hybrid Photodiode: An Efficient Self-Powered Fast-Response UV (visible) Photosensor. *Nanoscale* **2014**, *6*, 503−513.

(3) Docampo, P.; Guldin, S.; Leijtens, T.; Noel, N. K.; Steiner, U.; Snaith, H. J. Lessons Learned: From Dye-Sensitized Solar Cells To All-Solid-State Hybrid Devices. *Adv. Mater.* **2014**, *26*, 4013−4030.

(4) Martín, C.; Ziółek, M.; Douhal, A. Ultrafast and Fast Charge Separation Processes in Real Dye-Sensitized Solar Cells. *J. Photochem. Photobiol., C* **2016**, *26*, 1−30.

(5) Ashokkumar, R.; Kathiravan, A.; Ramamurthy, P. Aggregation Behaviour and Electron Injection/Recombination Dynamics of Symmetrical and Unsymmetrical Zn-Phthalocyanines on TiO_2 Film. *Phys. Chem. Chem. Phys.* **2014**, *16*, 1015−1021.

(6) Sharma, D.; Steen, G.; Korterik, J. P.; García-Iglesias, M.; Vázquez, P.; Torres, T.; Herek, J. L.; Huijser, A. Impact of the Anchoring Ligand on Electron Injection and Recombination Dynamics at the Interface of Novel Asymmetric Push-Pull Zinc Phthalocyanines and TiO_2. *J. Phys. Chem. C* **2013**, *117*, 25397−25404.

(7) Matsuzaki, H.; Murakami, T. N.; Masaki, N.; Furube, A.; Kimura, M.; Mori, S. Dye Aggregation Effect on Interfacial Electron-Transfer Dynamics in Zinc Phthalocyanine-Sensitized Solar Cells. *J. Phys. Chem. C* **2014**, *118*, 17205−17212.

(8) Imahori, H.; Kang, S.; Hayashi, H.; Haruta, M.; Kurata, H.; Isoda, S.; Canton, S. E.; Infahsaeng, Y.; Kathiravan, A.; Pascher, T.; et al. Photoinduced charge carrier dynamics of Zn-porphyrin-TiO_2 electrodes: the key role of charge recombination for solar cell performance. *J. Phys. Chem. A* **2011**, *115*, 3679−3690.

(9) Bach, U.; Lupo, D.; Comte, P.; Moser, J. E.; Weissörtel, F.; Salbeck, J.; Spreitzer, H.; Grätzel, M. Solid-State Dye-Sensitized Mesoporous TiO_2 Solar Cells with High Photon-To-Electron Conversion Efficiencies. *Nature* **1998**, *395*, 583−585.

(10) Kroeze, J. E.; Hirata, N.; Schmidt-Mende, L.; Orizu, C.; Ogier, S. D.; Carr, K.; Grätzel, M.; Durrant, J. R. Parameters Influencing Charge Separation in Solid-State Dye-Sensitized Solar Cells Using Novel Hole Conductors. *Adv. Funct. Mater.* **2006**, *16*, 1832−1838.

(11) Weisspfenning, C. T.; Lee, M. M.; Teuscher, J.; Docampo, P.; Stranks, S. D.; Joyce, H. J.; Bergmann, H.; Bruder, I.; Kondratuk, D. V.; Johnston, M. B.; et al. Optimizing the energy Offset between Dye and Hole-Transporting Material in Solid-State Dye-Sensitized Solar Cells. *J. Phys. Chem. C* **2013**, *117*, 19850−19858.

(12) Snaith, H. J.; Petrozza, A.; Ito, S.; Miura, H.; Grätzel, M. Charge Generation and Photovoltaic Operation of Solid-State Dye-Sensitized Solar Cells Incorporating a High Extinction Coefficient Indolene-Based Sensitizer. *Adv. Funct. Mater.* **2009**, *19*, 1810−1818.

(13) Cappel, U. B.; Gibson, E. A.; Hagfeldt, A.; Boschloo, G. Dye Regeneration by Spiro-MeOTAD in Solid State Dye-Sensitized Solar Cells Studied by Photoinduced Absorption Spectroscopy and Spectroelectrochemistry. *J. Phys. Chem. C* **2009**, *113*, 6275−6281.

(14) Cappel, U. B.; Smeigh, A. L.; Plogmaker, S.; Johansson, E. M.; Rensmo, H.; Hammarström, L.; Hagfeldt, A.; Boschloo, G. Characterization of the Interface Properties and Processes in Solid State Dye-Sensitized Solar Cells Employing a Perylene Sensitizer. *J. Phys. Chem. C* **2011**, *115*, 4345−4358.

(15) Howard, I. A.; Meister, M.; Baumeier, B.; Wonneberger, H.; Pschirer, N.; Sens, R.; Bruder, I.; Li, C.; Müllen, K.; Andrienko, D.; Laquai, F. Two Channels of Charge Generation in Perylene Monoimide Solid-State Dye-Sensitized Solar Cells. *Adv. Energy Mater.* **2014**, *4*, 1300640.

(16) Kim, H.-S.; Lee, C.-R.; Im, J.-H.; Lee, K.-B.; Moehl, T.; Marchioro, A.; Moon, S.-J.; Humphry-Baker, R.; Yum, J.-H.; Moser, J. E.; Grätzel, M.; Park, N.-G. Lead Iodide Perovskite Sensitized All-Solid-State Submicron Thin Film Mesoscopic Solar Cell with Efficiency Exceeding 9%. *Sci. Rep.* **2012**, *2*, 591.

(17) Hoppe, H.; Sariciftci, N. S. Organic solar cells: An overview. *J. Mater. Res.* **2004**, *19*, 1924−1945.

(18) Lu, L.; Zheng, T.; Wu, Q.; Schneider, A. M.; Zhao, D.; Yu, L. Recent Advances in Bulk Heterojunction Polymer Solar Cells. *Chem. Rev.* **2015**, *115*, 12666−12731.

(19) Lee, H. J.; Leventis, H. C.; Haque, S. A.; Torres, T.; Grätzel, M.; Nazeeruddin, M. K. Panchromatic Response Composed of Hybrid Visible-Light Absorbing Polymers and Near-IR Absorbing Dyes for Nanocrystalline TiO_2-Based Solid-State Solar Cells. *J. Power Sources* **2011**, *196*, 596−599.

(20) Sai Santos Kumar, R.; Grancini, G.; Petrozza, A.; Abrusci, A.; Snaith, H. J.; Lanzani, G. Effect of Polymer Morphology on P3HT-Based Solid-State Dye Sensitized Solar Cells: an Ultrafast Spectroscopic Investigation. *Opt. Express* **2013**, *21*, A469−A474.

(21) Humphry-Baker, N.; Driscoll, K.; Rao, A.; Torres, T.; Snaith, H. J.; Friend, R. H. Time-Evolution of Poly(3-hexylthiophene) as an Energy Relay Dye in Dye-Sensitized Solar Cells. *Nano Lett.* **2012**, *12*, 634−639.

(22) Yang, L.; Cappel, U. B.; Unger, E. L.; Karlsson, M.; Karlsson, K. M.; Gabrielsson, E.; Sun, L.; Boschloo, G.; Hagfeldt, A.; Johansson, E. M. J. Comparing Spiro and P3HT Hole Conductors in Efficient Solid State Dye-Sensitized Solar Cells. *Phys. Chem. Chem. Phys.* **2012**, *14*, 779−789.

(23) Martín-Gomis, L.; Fernández-Lázaro, F.; Sastre-Santos, Á. Advances In Phthalocyanine-Sensitized Solar Cells (PcSSCs). *J. Mater. Chem. A* **2014**, *2*, 15672−15682.

(24) Ragoussi, M.-E; Cid, J.-J.; Yum, J.-H.; de la Torre, G.; Di Censo, D.; Grätzel, M.; Nazeeruddin, M. K.; Torres, T. Carboxyethynyl Anchoring Ligands: A means to Improving the Efficiency of Phthanolcyanine-Sensitized Solar Cells. *Angew. Chem., Int. Ed.* **2012**, *51*, 4375−4378.

DOI: 10.1021/acs.jpcc.6b01583
J. Phys. Chem. C 2016, 120, 7044−7051

(25) Schlur, L.; Carton, A.; Lévêque, P.; Guillon, D.; Pourroy, G. Optimization of a New ZnO Nanorods Hydrothermal Synthesis Method for Solid State Dye Sensitized Solar Cells Applications. *J. Phys. Chem. C* **2013**, *117*, 2993−3001.
(26) Son, D.-Y.; Im, J.-H.; Kim, H.-S.; Park, N.-G. 11% Efficient Perovskite Solar Cell Based on ZnO Nanorods: An Effective Charge Collection System. *J. Phys. Chem. C* **2014**, *118*, 16567−16573.
(27) Son, D.-Y.; Bae, K.-H.; Kim, H.-S.; Park, N.-G. Effects of Seed Layer on Growth of ZnO Nanorod and Performance of Perovskite Solar Cell. *J. Phys. Chem. C* **2015**, *119*, 10321−10328.
(28) Anta, J. A.; Guillen, E.; Tena-Zaera, R. ZnO-Based Dye Sensitized Solar Cells. *J. Phys. Chem. C* **2012**, *116*, 11413−11425.
(29) Asbury, J. B.; Hao, E.; Wang, Y.; Ghosh, H. N.; Lian, T. Ultrafast electron transfer dynamics from molecular adsorbates to semiconductor nanocrystalline thin films. *J. Phys. Chem. B* **2001**, *105*, 4545−4557.
(30) Stranius, K.; George, L.; Efimov, A.; Ruoko, T.-P.; Pohjola, J.; Tkachenko, N. V. Photophysical Study of a Self-Assembled Donor-Acceptor Two-Layer Film on TiO_2. *Langmuir* **2015**, *31*, 944−952.
(31) Lehtivuori, H.; Efimov, A.; Lemmetyinen, H.; Tkachenko, N. V. Distributed Decay Kinetics of Charge Separated State in Solid Film. *Chem. Phys. Lett.* **2007**, *437*, 238−242.
(32) Lehtivuori, H.; Kumpulainen, T.; Efimov, A.; Lemmetyinen, H.; Kira, A.; Imahori, H.; Tkachenko, N. V. Photoinduced Electron Transfer in Langmuir−Blodgett Monolayers of Double-Linked Phthalocyanine−Fullerene dyads. *J. Phys. Chem. C* **2008**, *112*, 9896−9902.
(33) Saarenpää, H.; Sariola-Leikas, E.; Pyymaki Perros, A.; Kontio, J. M.; Efimov, A.; Hayashi, H.; Lipsanen, H.; Imahori, H.; Lemmetyinen, H.; Tkachenko, N. V. Self-assembled Porphyrins on Modified Zinc Oxide Nanorods: Development of Model Systems for Inorganic-Organic Semiconductor Interface Studies. *J. Phys. Chem. C* **2012**, *116*, 2336−2343.
(34) Cid, J. J.; Yin, J.-H.; Jang, S.-R.; Nazeeruddin, M. K.; Martinez-Ferrero, E.; Palomares, E.; Ko, J.; Grätzel, M.; Torres, T. Molecular Cosensitization for Efficient Panchromatic Dye-Sensitized Solar Cells. *Angew. Chem., Int. Ed.* **2007**, *46*, 8358−8362.
(35) Olson, D. C.; Lee, Y.-J.; White, M. S.; Kopidakis, N.; Shaheen, S. E.; Ginley, D. S.; Voigt, J. A.; Hsu, J. W. P. Effect of Polymer Processing on the Performance of Poly(3-Hexylthiophene)/ ZnO Nanorod Photovoltaic Devices. *J. Phys. Chem. C* **2007**, *111*, 16640−16645.
(36) Burschka, J.; Dualeh, A.; Kessler, F.; Baranoff, E.; Cevey-Ha, N.-L.; Yi, C.; Nazeeruddin, M. K.; Grätzel, M. Tris(2-(1 H -pyrazol-1-yl)pyridine)cobalt(III) as p-Type Dopant for Organic Semiconductors and its Application in Highly Efficient Solid-State Dye-Sensitized Solar Cells. *J. Am. Chem. Soc.* **2011**, *133*, 18042−18045.
(37) Fukuzumi, S.; Ohkubo, K.; Ortiz, J.; Gutiérrez, A. M.; Fernandez-Lázaro, F.; Sastre-Santos, A. Formation of a Long-Lived Charge-Separated State of a Zinc Phthalocyanine-Perylenediimide Dyad by Complexation with Magnesium Ion. *Chem. Commun.* **2005**, *30*, 3814−3816.
(38) Guldi, D. M.; Zilbermann, I.; Gouloumis, A.; Vázquez, P.; Torres, T. Metallophthalocyanines: Versatile Electron-Donating Building Blocks for Fullerene Dyads. *J. Phys. Chem. B* **2004**, *108*, 18485−18494.
(39) Mack, J.; Stillman, M. J. Photochemical Formation of the Anion Radical of Zinc Phthalocyanine and Analysis of the Absorption and Magnetic Circular Dichroism Spectral Data. Assignment of the Optical Spectrum of [ZnPc(−3)]-. *J. Am. Chem. Soc.* **1994**, *116*, 1292−1304.
(40) Kroeze, J. E.; Savenije, T. J.; Vermeulen, M. J. W.; Warman, J. M. Contactless Determination of the Photoconductivity Action Spectrum, Exciton Diffusion Length, and Charge Separation Efficiency in Polythiophene-Sensitized TiO_2 Bilayers. *J. Phys. Chem. B* **2003**, *107*, 7696−7705.
(41) Peumans, P.; Yakimov, A.; Forrest, S. R. Small Molecular Weight Organic Thin-Film Photodetectors and Solar Cells. *J. Appl. Phys.* **2003**, *93*, 3693−3723.
(42) Heremans, P.; Cheyns, D.; Rand, B. P. Strategies for Increasing the Efficiency of Heterojunction Organic Solar Cells: Material Selection and Device Architecture. *Acc. Chem. Res.* **2009**, *42*, 1740−1747.
(43) Mawyin, J.; Shupyk, I.; Wang, M.; Poize, G.; Atienzar, P.; Ishwara, T.; Durrant, J. D.; Nelson, J.; Kanehira, D.; Yoshimoto, N.; et al. Hybrid Heterojunction Nanorods for Nanoscale Controlled Morphology in Bulk Heterojunction Solar Cells. *J. Phys. Chem. C* **2011**, *115*, 10881−10888.
(44) Xie, Y.; Li, Y.; Xiao, L.; Qiao, Q.; Dhakal, R.; Zhang, Z.; Gong, Q.; Galipeau, D.; Yan, X. Femtosecond Time-Resolved Fluorescence Study of P3HT/PCBM Blend Films. *J. Phys. Chem. C* **2010**, *114*, 14590−14600.
(45) Driscoll, K.; Fang, J.; Humphry-Baker, N.; Torres, T.; Huck, W. T. S.; Snaith, H. J.; Friend, R. H. Enhanced Photoresponse in Solid-State Excitonic Solar Cells via Resonant Energy Transfer and Cascaded Charge Transfer from A Secondary Absorber. *Nano Lett.* **2010**, *10*, 4981−4988.

DOI: 10.1021/acs.jpcc.6b01583
J. Phys. Chem. C 2016, 120, 7044−7051

Supporting information

Effect of Hole Transporting Material on Charge Transfer Processes in Zinc Phthalocyanine Sensitized ZnO Nanorods

Hanna Hakola, Essi Sariola-Leikas, Alexander Efimov and Nikolai V. Tkachenko

Department of Chemistry and Bioengineering, Tampere University of Technology, P.O. Box 541, 33101 Tampere, Finland

ZnPc synthesis

The idea behind the synthesis was to prepare an A_3B-substituted phthalocyanine with "cartwheel" symmetry, axially protected from excessive aggregation.[1] Statistical condensation of the two phthalonitriles 1 and 2 by "DBU method" followed by KOH hydrolysis provided the target substance 3 with 10% yield. The synthetic route is presented in SI Figure 1.The moderate efficiency of the reaction must be attributed to a sterical hindrance of mesityl groups, which restricts the formation of isomers other than with 1,8,15,22-substitution pattern. In the NMR spectra (Figure S1) one can see well-resolved multiplets of phthalo- and carboxyphenyl-protons (8.7-7.5 ppm), as well as the two signals from meta-aryl-protons of mesityl groups at 7.34 and 6.95 ppm with the relative intensity 2:1. Similarly, the signals of perypheral methyl groups are found at 2.75 and 2.08 ppm (6 and 12 protons), and 2.32 and 1.83 ppm (3 and 6 protons, respectively), which can be rationalized as the two mesityl fragments more shielded and one less shielded present in the molecule. It must be admitted that addition of 5% of deuteromethanol to chloroform is required to obtain a well-resolved picture, and the NMR spectrum changes slightly with concentration of the analyte. That is, we cannot claim the aggregation completely conquered, however good resolution and a moderate number of ^{13}C signals let us claim that the substance is chiefly is a monoisomeric phthalocyanine and at mg/ml concentrations is present in solution in a non-clasterized form.

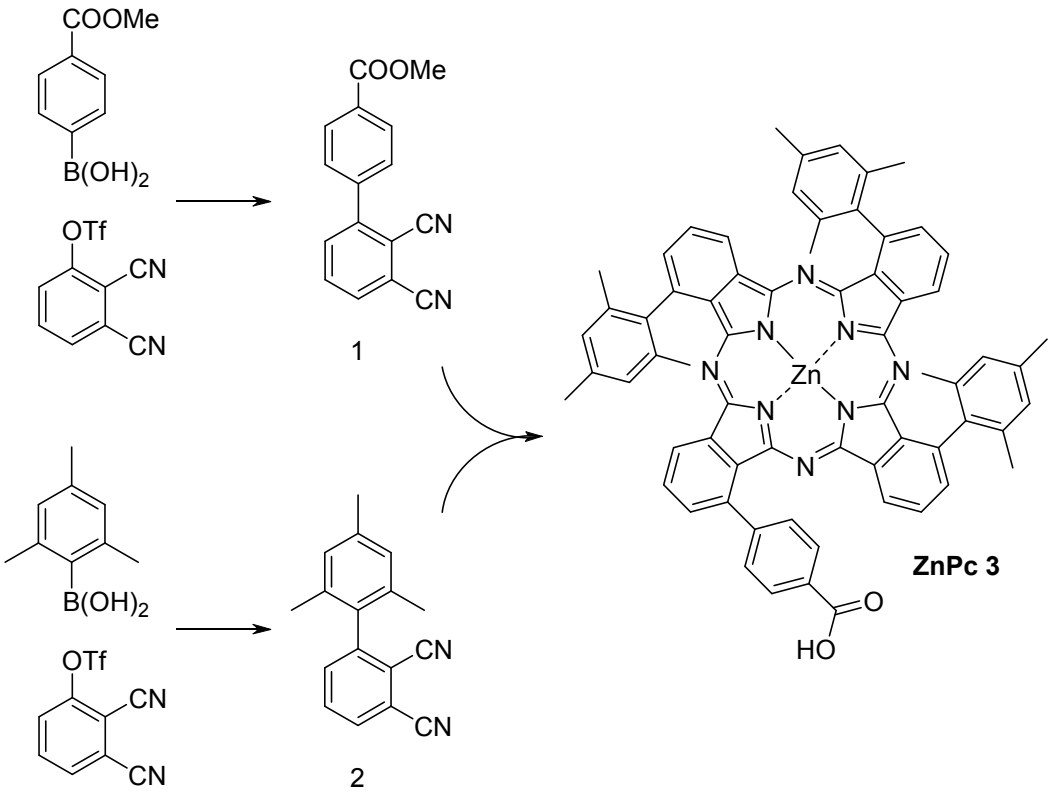

Figure S1 Syntetic route to ZnPc.

2,3-Dicyanophenyl trifluoromethylsulfonate was synthesized as described elsewhere.[1] Purification of the products was carried out either by column chromatography on Silica gel 60 (Merck) mesh size 40-63 μm or on preparative TLC plates (Merck) coated with neutral aluminum oxide 60 F254. NMR spectra were recorded using Varian Mercury 300 MHz spectrometer using TMS as internal standard. HRMS measurements were done with Waters LCT Premier XE ESI-TOF bench top mass spectrometer. Lock-mass correction (leucine enkephaline as reference compound), centering and calibration were applied to the raw data to obtain accurate mass. The synthetic route to ZnPc is shown in Figure 1.

Methyl 2',3'-dicyanobiphenyl-4-carboxylate (1). K_3PO_4 (0.46 g, 2.16 mmol) was dissolved in water (5 mL). Toluene (5 mL), 4-carboxymethyl phenylboronic acid (0.129 g, 0.72 mmol), and 2,3-dicyanophenyl trifluoromethylsulfonate (0.2 g, 0.72 mmol), and $Pd(dppf)Cl_2 \cdot CH_2Cl_2$ (29 mg, 0.036 mmol) were added to the vial. The r.m. was vigorously stirred under argon (90°C). After 16 h the r.m. was cooled down and diluted with brine (10 mL). Organic layer was collected, the water layer was extracted again with toluene (20 mL), and the combined organic extracts were washed with water (50 mL) and evaporated to dryness. Flash chromatography on Silica 60 (eluent $CHCl_3$) provided the target compound as a white solid (113 mg, 60%). Data for **2**: ^{1}H NMR (300 MHz, $CDCl_3$, TMS): δ = 8.22 – 8.17 (m, 2H), 7.88 – 7.75 (m, 3H), 7.66 – 7.60 (m, 3H), 3.96 (s, 3H) ppm. ^{13}C NMR (75 MHz, $CDCl_3$, TMS): δ = 166.49, 146.42, 140.77, 134.23, 133.36, 132.86, 131.51, 130.51, 129.05, 117.76, 115.70, 115.11, 114.81, 52.68 ppm. MS (ESI-TOF): [M+Na]+ calcd for $C_{16}H_{10}N_2O_2Na$+, 285.0640; found: 285.0614.

2',4',6'-Trimethylbiphenyl-2,3-dicarbonitrile (2). K_3PO_4 (3.1 g, 14.64 mmol) was dissolved in water (40 mL). Toluene (40 mL), mesitylboronic acid (0.8 g, 4.88 mmol), and 2,3-dicyanophenyl trifluoromethylsulfonate (1.35 g, 4.88 mmol), and $Pd(dppf)Cl_2 \cdot CH_2Cl_2$ were added to the vial. The r.m. was vigorously stirred under argon (90°C). After 16 h the r.m. was cooled down and diluted with brine (20 mL). Organic layer was collected, the water layer was extracted again with toluene (40 mL), and the combined organic extracts were washed with water (3×100 ml) and evaporated to dryness. Flash chromatography on Silica 60 (eluent CH_2Cl_2) provided the target compound as a white solid (670 mg, 56%). Data for **2**: ^{1}H NMR (300 MHz, $CDCl_3$, TMS): δ = 7.86 – 7.71 (m, 2H), 6.99 (s, 2H), 2.34 (s, 3H), 1.97 (s, 6H) ppm. ^{13}C NMR (75 MHz, $CDCl_3$, TMS): δ = 147.84, 139.26, 135.53, 135.13, 133.35, 133.19, 132.22, 129.02, 21.88, 20.48 ppm. MS (ESI-TOF): [M+H]+ calcd for $C_{17}H_{15}N_2$+, 247.1235; found: 247.1237.

Zinc 4-(1,15,22-trimesitylphthalocyanine-8-yl)benzoic acid (3). Phthalonitrile **1** (47 mg, 0.19 mmol), phthalonitrile **2** (150 mg, 0.57 mmol), and $Zn(OAc)_2 \cdot H_2O$ (87 mg, 0.475 mmol) were mixed in pentanol (100 mL) and heated at reflux under a drying tube (24 h). The solution was cooled down and evaporated to dryness at reduced pressure. The dark residue was dissolved in THF (15 ml), methanol (3.5 ml) and KOH/H_2O solution (1.55%, 1.55 mL) was added, and the r.m. was stirred at r.t. (48 h). The solution was neutralized by addition of HCl (2 mol l^{-1}, 2.1 mL), and solvents were removed under reduced pressure. Target substance was obtained by flash chromatography on Silica 100 (eluent $CHCl_3$, then $CHCl_3$/EtOH/AcOH 20/1/0.1) as a second green band with the yield 19 mg (9.5%). Data for **3**: ^{1}H NMR (300 MHz, $CDCl_3$, TMS): δ = 9.25 (br, 1H), 8.79 – 8.29 (m, 6H), 8.14-7.61 (m, 12H), 7.45-7.36 (m, 6H), 2.80 (br s, 6H), 2.21-2.07 (m, 18H) ppm. ^{13}C NMR (75 MHz, $CDCl_3$, TMS): δ = 147.84, 139.26, 135.53, 135.13, 133.35, 133.19, 132.22, 129.02, 21.88, 20.48 ppm. MS (ESI-TOF): [M+H]+ calcd for $C_{66}H_{51}N_8O_2Zn$+, 1051.3427; found: 1051.3401.

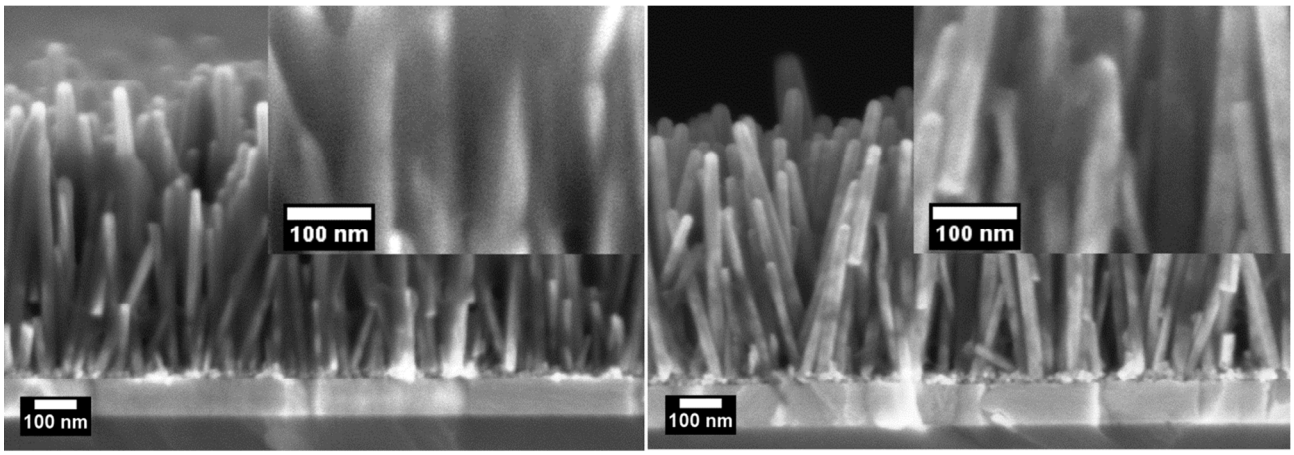

Figure S2 Cross section SEM images of ZnOr|ZnPc, ZnOr|ZnPc|P3HT and ZnOr|ZnPcSpiro-OMeTAD. A visual difference in filling voids in ZnOr|ZnPc|Spiro-OMeTAD and ZnOr|Spiro-OMeTAD structure is mainly due to the fact that in the former case ZnOr are 200 nm longer.

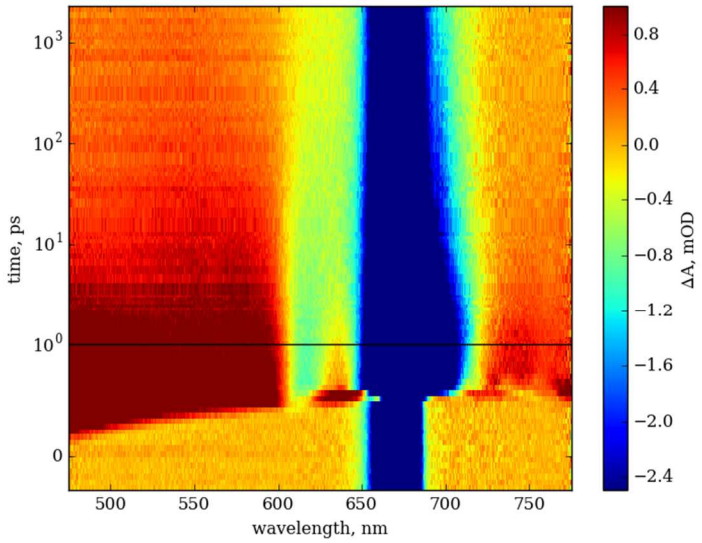

Figure S3 Transient absorption response map of ZnOr|ZnPc in the visible part of the spectrum (linear time scale till 1 ps and logarithmic after 1 ps). Excitation wavelength was 680 nm.

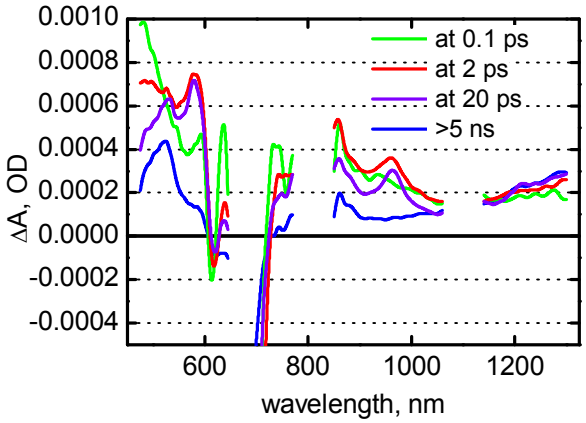

Figure S4. Time resolved spectra of ZnOr|ZnPc|Spiro-OMeTAD. Excitation wavelength was 680 nm.

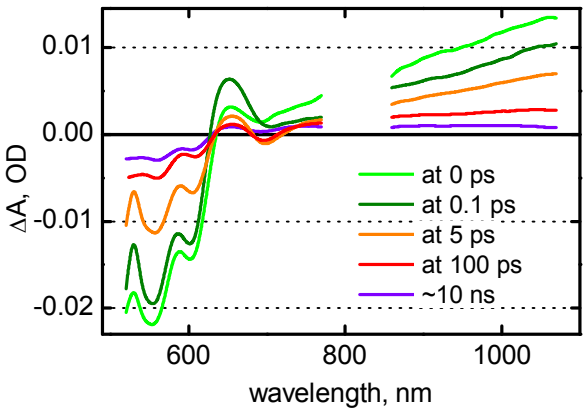

Figure S5. Time resolved spectra of ZnO|ZnPc|P3HT. Excitation wavelength was 500 nm

REFERENCES

1. Ranta, J.; Kumpulainen, T.; Lemmetyinen, H.; Efimov, A. Synthesis and Characterization of Monoisomeric 1,8,15,22-Substituted (A3B and A2B2) Phthalocyanines and Phthalocyanine−Fullerene Dyads *J. Org. Chem.* **2010**, *75*, 5178-5194.

Tampereen teknillinen yliopisto
PL 527
33101 Tampere

Tampere University of Technology
P.O.B. 527
FI-33101 Tampere, Finland

ISBN 978-952-15-3748-6
ISSN 1459-2045